MEMS-based Tunable Optical Filter Arrays for Nano-Spectrometer in the Visible Spectral Range

Dissertation

vorgelegt von
Onny Setyawati

eingereicht zur Erlangung des akademischen Grades eines
Doktors der Ingenieurwissenschaften (Dr.-Ing.)
im Fachbereich Elektrotechnik/Informatik
der Universität Kassel

Kassel, Dezember 2011

Erklärung

Hiermit versichere ich, dass ich die vorliegende Arbeit selbstständig und ohne unerlaubte Hilfe angefertigt und andere als die in der Dissertation angegebenen Hilfsmittel nicht benutzt habe. Alle Stellen, die wörtlich oder sinngemäß aus veröffentlichten oder unveröffentlichten Schriften entnommen sind, habe ich als solche kenntlich gemacht. Kein Teil dieser Arbeit ist in einem anderen Promotions- oder Habilitationsverfahren verwendet worden.

Kassel, Dezember 2011

Onny Setyawati

Diese Arbeit wurde zur Erlangung des akademischen Grades eines Doktors der Naturwissenschaften (Dr. rer. nat) im Fachbereich Elektrotechnik / Informatik der Universität Kassel vorgelegt und angenommen.

Eingereicht am	15. Dezember 2011
Tag der Disputation	27. Januar 2012
Gutachter:	Prof. Dr. Hartmut Hillmer Prof. Dr.-Ing. Josef Börcsök
Promotionskommission:	Prof. Dr. Hartmut Hillmer Prof. Dr.-Ing. Josef Börcsök Prof. Dr.-Ing. Axel Bangert Prof. Dr.-Ing. Peter Lehmann

Title:

MEMS-based Tunable Optical Filter Arrays for Nano-Spectrometer in the Visible Spectral Range

Author:

Onny Setyawati

Reviewer:

Prof. Dr. H. Hillmer/Prof. Dr.-Ing. J. Börcsök

Abstract

Tunable Fabry Pérot filter arrays in a visible spectral range for the implementation in a nano-spectrometer are investigated. The aim of this work is to fabricate tunable filter arrays using low cost technologies. Materials and technological processes which are adequate for the filter arrays fabrication are evaluated. In addition, a numerical model simulation to select the optimal design of filter structures is presented, wherein an investigation on the displacement of the filter membranes due to the stress in the materials is performed. Multilayers of dielectric DBRs and UV-NIL polymers as filters cavity material are introduced. Lateral structuring of the DBRs in RIE process, and underetching of the polymers in an oxidation plasma to obtain the filter's air gap cavity, are attained. The tunable Si_3N_4/SiO_2 DBRs-based filter arrays are succesfully fabricated. Optimization on structuring of high index contrast of TiO_2/SiO_2 DBRs-based filters are accomplished.

Keywords: *spectrometer, Fabry Pérot, tunable optical filter, MEMS, dry etching.*

Titel:

MEMS-basierende durchstimmbare optische Filter-Arrays für Nano-Spektrometer im sichtbaren Spektralbereich

Autor:

Onny Setyawati

Gutachter:

Prof. Dr. H. Hillmer/Prof. Dr.-Ing. J. Börcsök

Zusammenfassung

Im Rahmen dieser Arbeit, werden durchstimmbare Fabry Pérot Filter-Arrays im sichtbaren Spektralbereich für die Umsetzung als Nano-Spektrometer untersucht. Das Ziel dieser Arbeit ist, durchstimmbare Filter-Arrays mit kostengünstigen Technologien herzustellen. Materialien und technologische Prozesse, die für die Filter-Array-Herstellung benötigt werden, wurden untersucht. Darüber hinaus wurde ein Modell der numerischer Simulation vorgestellt, um das optimale geometrischen Design der Filterstrukturen zu erhalten, wobei sich das Hauptaugenmerk der Untersuchung auf die Durchbiegung der Filtermembranen aufgrund der mechanischen Dünnschicht-Spannungen richtet. Multischichten von den dielektrischen DBR-Spiegeln und UV-NIL-Polymere als Kavitätsmaterial wurden eingeführt. Lateralstrukturierung der DBR-Spiegel im RIE-Prozess, und der Unterätz-Prozesse der Polymere im Sauerstoffplasma um den Filter mit der Luftkavität zu erstellen, wurden durchgeführt. Die durchstimmbaren Si_3N_4/SiO_2 DBR-basierende Filter-Arrays wurden erfolgreich hergestellt. Optimierung bei der Strukturierung von hoher Brechungsindex-Kontrast der TiO_2/SiO_2 DBR-basierende Filter konnten erzielt werden. Die Ergebnisse dieser Arbeit ermöglichen die Realisierung eines breiten Spektralbereichs der Filter-Arrays im Nano-Spektrometer.

Stichwörter: *Spektrometer, Fabry Pérot, durchstimmbare optische Filter, MEMS, Ätz-Prozess.*

Nomenclature

Al	Aluminum
Ar	Argon
BK7	bor-crown glass, high quality glass
Cr	Chrome
CCD	Charge-Coupled Device
CCP	Capacitively Coupling Plasma
CHF_3	Trifluoromethane
CMOS	Complementary Metal Oxide Semiconductor
DBR	Distributed Bragg Reflector
FEM	Finite Element Method
FP	Fabry Pérot
FSR	Free Spectral Range
FT	Fourier Transform
FWHM	Full Width at Half Maximum
HfO_2	Hafnium Oxide
IBSD	Ion Beam Sputter Deposition
ICP	Inductively Coupling Plasma
IR	Infrared
ITO	Indium Tin Oxide
MEMS	Micro-Electro-Mechanical-System
MFC	Mass Flow Controller
NIR	Near-IR
NMP	N-Methyl-Pyrollidone
PECVD	Plasma Enhanced Chemical Vapor Deposition
PSG	Phosphosilicate glass
PZT	Piezoelectric Transducer
RF	Radio Frequency
RIBSD	Reactive IBSD
RIE	Reactive Ion Etching
RTA	Rapid Thermal Annealing
sccm	Standard Cubic Centimeters per Minute
SCIL	Substrate Conformal Imprint Lithography

SEM	Scanning Electron Microscope
SF_6	Sulfurhexafloride
Si	Silicon
Si_3N_4	Silicon Nitride
SiO_2	Silicon Oxide
TiO_2	Titanium Oxide
UV-NIL	Ultraviolet Nanoimprint Lithography
WLI	White Light Interferometer
$A(\varphi)$	Airy function
A	membrane area
α_m	slope angle of the mask
α	slope angle of the structure
c	speed of light in vacuum
d	cavity length, Δd the changes in the cavity (cavity range)
ϵ_0	permittivity of free space
$e^{'}$	energy from an energized particles
E_F	etch rate of thin film
E_{PR}	etch rate of the mask
E_t	amplitude of transmitted beam
f	frequency, Δf frequency bandwidth
F_{net}	total force
F_s	finesse
g_{PI}	cavity gap at pull-in condition
I_t	intensity of transmitted beam
I_T	energy transmission coefficient
k	spring constant
K	integer (plasma etch step)
λ	wavelength, $\Delta\lambda$ wavelength range
m	integer (mode)
n	effective refractive index
n_H	high refractive index
n_L	low refractive index
N	number of grating slits
r	reflection
R	reflection coefficient
R_s	resolution
S	etch selectivity
t	transmission
T	transmission coefficient
θ	angle of incident beam
φ	phase lag
ϵ	correction for phase change
V_{PI}	pull in voltage
η_t	tuning efficiency

List of Publications

1. C. Woidt, **O. Setyawati**, A. Albrecht, M. Engenhorst, V. Daneker, T. Woit, S. Wittzack, F. Köhler, H.H. Mai, M. Bartels, and H. Hillmer, "Micromachined Tunable Fabry-Pérot Filter Integrated into a Miniaturized Spectrometer for Low-Cost Applications", p. 537-541, *Inbook "Nanotechnological Basis for Advanced Sensors"*, Publisher: Springer-Dordrecht, Editor: J. P. Reithmaier, P. Paunovic, W. Kulisch, C. Popov and Plamen Petkov (Hrsg.), 2011.

2. **O. Setyawati**, M. Engenhorst, M. Bartels, V. Daneker, S. Wittzack, T. Woit, F. Köhler and Harmut Hillmer, "Characterization of Dry Etching of TiO_2/SiO_2 Distributed Bragg Reflectors for Tunable Optical Sensor Arrays", *SPIE Journal of Micro/Nanolithography, MEMS, and MOEMS*, Vol. 9, Issue 4, Article 041110, p. 041110 (1-6), Dec 28, 2010. doi: 10.1117/1.3524828.

3. **O. Setyawati**, M. Engenhorst, S. Wittzack, F. Köhler, C. Woidt, T. Woit, V. Daneker, M. Bartels and Hartmut Hillmer, "Dry Etching of TiO_2/SiO_2 DBR Mirrors for Tunable Optical Sensor Arrays", *SPIE Proceedings Photonic West MOEMS-MEMS 2010*, ISBN: 9780819479877, Vol. 7591 (Advanced Fabrication Technologies for Micro/Nano Optics and Photonics III) Nr. 7591-26, p. 75910R-(1 - 8), Publisher: SPIE (Society of Photo-Optical Instrumentation Engineers), February 2010. doi: 10.1117/12.841881.

4. **O. Setyawati**, H. H. Mai, C. Woidt, S. Schudy, M. Engenhorst, S. Wittzack, F. Köhler, M. Bartels and H. Hillmer, "Low-Cost Micromachined Tunable Fabry-Pérot Filters for Optical Nano Sensor Arrays", *Technical Digest MOC´10, 16th Microoptics Conference 2010*, p. TB4(64-65), Oct-Nov 2010, National Chiao Tung University and Microoptics Group, 2010.

5. H. H. Mai, **O. Setyawati**, V. Daneker, C. Woidt, T. Woit, K. Schultz, S. Schudy, M. Engenhorst, X. Wang, S. Wittzack, F. Köhler, A. Albrecht, M. Bartels and H. Hillmer, "Verification and Calibration of Spectral Properties of High-resolution Nano Sensor Arrays Using Microscope Spectrometers", *Technical Digest MOC´10, 16th Microoptics Conference 2010*, p. MC3(22-23), Oct-Nov 2010, National Chiao Tung University and Microoptics Group, 2010.

6. A. Albrecht, H. Mai, V. Daneker, X. Wang, S. Schudy, T. Woit, K. Schultz, C. Woidt, **O. Setyawati**, F. Köhler, S. Wittzack, M. Engenhorst, M. Bartels and H. Hillmer, "Optical Characterization of High-Resolution Optical Nanospectrometers for Networked Sensing Systems", *INSS Conference 2010, IEEE Technical Digest INSS*, ISBN 978-1-4244-7910-8, S.175-178, 2010.

7. M. Bartels, S. Wittzack, F. Köhler, X. Wang, A. Albrecht, S. Schudy, M. Engenhorst, H. H. Mai, **O. Setyawati**, T. Woit, C. Woidt and H. Hillmer, "High Vertical Resolution 3D

Nanoimprint Technology for Nanophotonic Applications", *IEEE/LEOS International Conference on Optical MEMS and Nanophotonics 2009*, p. 87-88, 2009.

8. S. Wittzack, F. Köhler, X. Wang, **O. Setyawati**, T. Woit, A. Albrecht, M. Engenhorst, S. Schudy, C. Woidt, M. Bartels and H. Hillmer, "Hochpräzise Nanoimprint-Templates für 3D-Strukturen", *Galvanotechnik* Vol. Band 100, Heft 10, p. 2376-2382, 2009.

Contents

Abstract **iii**

Nomenclature **v**

List of Publications **vii**

1 Introduction **1**

2 State of the Art **5**

3 Basics of the Optical Filter, Materials and Methods **13**
3.1 Fabry-Pérot Filter and its Optical Properties 13
3.1.1 Distributed Bragg Reflectors (DBRs) 16
3.1.2 Electrostatic Actuation 18
3.2 MEMS Surface Micromachining: the Promise 19
3.3 Deposition Methods 21
3.3.1 Plasma Enhanced Chemical Vapour Deposition (PECVD) 21
3.3.2 Ion Beam Sputtering Deposition (IBSD) 21
3.4 UV-NanoImprint Lithography (UV-NIL) polymer 22
3.5 Dry Etching Process: Tools Overview 22
3.5.1 Capacitively Coupling Plasma - Reactive Ion Etching 25
3.5.2 Inductively Coupling Plasma - Reactive Ion Etching 26
3.5.3 Barrel Plasma Etcher: Oxygen Plasma 26
3.6 Filters Characterization Methods 28
3.6.1 Microscope-Spectrometer's Set-up Measurement 28
3.6.2 White-Light Interferometer 28

4 Filter Structure Design **31**
4.1 Filters Technological Fabrication 31
4.2 Filter Arrays for the Sensor Application 34
4.3 Numerical Analysis on Filter Geometric Structures 36
4.3.1 Membrane Displacement due to the Stress 36
4.3.2 Simulation Results and Discussion 38

5 Tunable Si_3N_4/SiO_2 DBRs-based Filters **45**
5.1 Lateral Structuring of the DBRs 45
5.1.1 Etching Process in the Capacitively Coupling Plasma - RIE 45
5.1.2 Etching Process in the Inductively Coupling Plasma- RIE 47
5.1.3 *RIE-mode* in the Inductively Coupling Plasma - RIE 49
5.2 UV-NIL Polymers as the Cavity Layers 52
5.2.1 mr-UVCur06 and mr-UVCur21 Polymers 52
5.2.2 PAK-01 Polymer 53
5.2.3 Underetching Process in the Oxygen Plasma 55
5.3 Contact Electrodes 56
5.3.1 Indium-Tin-Oxide as the Bottom and Top Electrodes 56
5.3.2 Aluminum as the Top Electrode 58
5.4 Results and Discussion 59

6 TiO_2/SiO_2 DBRs-based Filters **67**
6.1 Lateral Structuring of the DBRs 67
6.1.1 Etch process in the ICP-RIE: using hard etch masks 67
6.1.2 Etch process in the CCP- and the ICP-RIE: using photoresist etch masks 74
6.2 UV-NIL Polymers as the Cavity Layer 79
6.2.1 PAK-01 Polymer 79
6.2.2 mr-UVCur21 and mr-UVCur06 Polymers 81
6.3 The Contact Electrodes: ITO and Al Layers 82
6.4 Results and Discussion 83

7 Summary and Outlook **89**

Bibliography **91**

List of Figures **102**

List of Tables **110**

Acknowledgements **113**

A Plate theory, elastic energy and virtual work principle **115**

B Technological processes regarding the fabrication **119**
B.1 Lithography of the photoresists 119
B.2 Film deposition 120
B.3 Photomasks for the fabrication 120
B.4 Material and coating process concerning the UV-NIL polymers 121
B.4.1 The coating process of the polymers 122
B.4.2 PAK-01 polymer 122
B.5 Etch conditions for lateral structuring of the DBRs 123

Chapter 1

Introduction

DETECTING and analysing spectra by means of an optical spectrometer, have nowadays attained significant attention, for instance, in the study of the composition of a sample liquid by measuring the fluorescence and bioluminescence spectrum [1, 2], and for determination of the chemical bonds [3]. It is also ulitized for examining of chlorophyll fluorescence at tree canopy levels for water stress monitoring [4].
The spectrometers become well-known instruments for several applications in life sciences, manufacturing, engineering, and health care due to their high selectivity and high sensitivity along with their contactless-type measurement. However, they are generally cumbersome and sometimes more costly in maintenance and installation than the instrument itself [5]. In addition, they are normally designed only for specific tasks.

Micro-Electro-Mechanical-System (MEMS) technology appears over the last decade to fullfil the needs of having compact, light-weight, reliable, and high precision portable devices. MEMS-based minispectrometers are the instruments which are considered as disruptive technology [6]. The compact, less power-consumed, and portable devices will raise the productivity of some traditional applications, where the miniaturized spectrometers now can be taken to the sample, in contrast to bring the sample to the devices. Their small sizes occasionally evince lower cost products compared to the conventional spectrometers, hence, they can lead to new applications those beyond the laboratories.

Miniaturized Fabry-Pérot (FP) filters are very attractive devices for optical communication and "smart personal environments", including health-care applications. They bring out a potential solution to reduce the entire production cost of component manufacture. Using low-cost technologies in the fabrication of the filters should be considered, to influence significantly the economical aspect of the devices [7]. An array of several static (non-tunable) FP filters have been developed at the institute, with the nanoimprint technology to fabricate the different filter cavities in one step process by means of a stamp or template nanostructure [8, 9]. Nanoimprint is well known as a low cost technology for batch production [10, 11]. This technology will benefit the nano-spectrometer production in creating different cavity thicknesses of the filter arrays. The filter arrays will be integrated into the detector array to create a compact device which can lead to a handheld and

portable spectrometer.
The tunable filters for spectroscopic applications need a large tuning range, and since they operate in a low-order mode, multiple filters are required to obtain a broad wavelength range. The reasons, why the tunable optical filters in visible range are required for different applications, will be reviewed here. Visible range-spectrometers derive a benefit from the CCD-detector, wherein its low cost-product and technical progress have been supported by consumer needs [6]. And compared to the visible one, the cost of detectors for the infrared (IR) spectrometers are relatively higher. The aforementioned static FP filter arrays-based spectrometer ensures the parallelism of the mirrors that formed the filters. However, many detectors will contribute for analysing the signal, hence, under the ideal condition only a fraction of the light intensity is available for each filter and the optical power dissipation occurs. Despite the complexity in fabrication of an air gap cavity for a tunable filter, it gives benefit, i.e. the air gap cavity is a way to avoid the rising absorption of the materials for the Distributed Bragg Reflectors (DBRs).

The **objective** of this work is to fabricate tunable FP filter arrays for the visible spectral range applications using low cost technologies. The filter arrays are designed accordingly to the detectors (courtesy of MAZeT GmbH) for the implementation of a high-precision colour sensor. In order to fabricate the tunable filter arrays, several experiments have been performed to obtain the optimal and compatible fabrication process concerning the utilized material and the design. The experiments focus on structuring and characterizing the filters. The preliminary results gained from this work are necessary for the fabrication of the FP filter arrays in the visible spectral range, and afterward for the ones which will be operated in the IR/NIR (near-IR) range.
Dielectric-based filters are very attractive due to the trade-off between the transmission peak and mirror reflectivity inherited by metal-based filters [12]. In this work, two DBR material systems, Si_3N_4/SiO_2 and TiO_2/SiO_2, are investigated. The etching processes for patterning the DBRs are introduced and evaluated under different etch masks.
The application of UV-NIL (Ultra Violet NanoImprint Lithography) polymers as post structures and sacrificial layers are described. In this work, spin coating process was used for applying the polymer as filter's cavity layer. Underetching of the UV-NIL polymers, characterization of the filters and some optimization processes regarding the filter fabrication are also presented. Since the photomask that is used for the fabrication contains different filter geometric structures, a simplified model simulation has been made to investigate the displacement (or deflection) of the filter membrane, regarding different filter geometries, i.e. the membrane diameter and the suspensions.

Chapter outline of this thesis is given in the following.

- Chapter 1 introduces the motivation and research objective of this work.
- Chapter 2 presents the state of the art, including Micro/ Nano-spectrometer bases upon the grating- and interference-type, and addresses the filter arrays-based spectrometer as the focus of this work.
- Chapter 3 contains basics of Fabry-Pérot filter, starts with theory of Fabry-Pérot

etalon, followed by the DBRs as main component of the filter and electrostatic tuning mechanism. Overview on MEMS-based filters, technological processes, i.e. the deposition and dry etching tools, the materials utilized in the fabrication, and the characterization methods are also described.

- Design of the filter arrays for the sensor applications will be introduced along with their technological fabrication in Chapter 4. In addition, the simplified model simulation using FEMLAB software for investigating membrane displacements due to the stress in the materials is described. The simulation is performed concerning the type of DBRs and different filter geometries. Significant simulation results are presented.

- Experiments and results regarding the tunable Si_3N_4/SiO_2-air gap filters are described in Chapter 5. Dry etching of the DBRs, underetching process of the polymers, and the contact electrodes are explained. The characterization on the mechanical and optical properties of the filters are documented and discussed.

- Chapter 6 explains the experimental fabrication of TiO_2/SiO_2- based filters, and focuses on the optimization of lateral structuring of the DBRs using reactive ion etching (RIE) process. Investigation on the adhesion between the polymers and the TiO_2/SiO_2 dielectric materials is also described. Results of the fabricated filters are presented.

Chapter 2

State of the Art

In this chapter a review of microspectrometers that have been fabricated by silicon micromachining process, and by other methods such as surface micromachining and LIGA[1] technique wherein metal, plastic or glass are used, will be presented. The milestones are focused on the grating- and filter-type spectrometers and the comparison of their spectral resolution. Review on filter arrays-based micro/nano-spectrometers will close this chapter. The review gives the relevance of this research work.

Miniature Spectrometer: Cost and benefit

Minispectrometers have been developed since the past two decades. MEMS technology emerges to create compact, light-weight and portable devices, and it allows the portable spectrometer to be taken to the sample being measured, instead of taking the sample to the device. It grows potential productivity of some conventional applications, hence, the bulky spectrometers has been replaced now with the miniature ones [13–16]. MEMS-based spectrometers are considered as the instruments with a disruptive technology [6]. Featuring miniaturization, multiplicity and microelectronics within this technology, batch and low-cost productions can also be attained, hence, device applications can be extended to those beyond the laboratory [17].
Important things that are needed to be considered when miniaturizing the spectrometers, that is it leads to the decreasing of system throughput and signal-to-noise ratio, and in turn, it will reduce also the device resolution [18]. To recompense these shortcomings, many results have been published with different kind of solutions, for instance in producing the wavelength dispersive elements and the integrated or tunable detectors as part of the research interest [19–22].
Microspectrometers that are fabricated compatible with the silicon process, that is, they can be integrated toward silicon devices are reported by Wolffenbuttel [12]. Other spectrometers that are fabricated by the surface micromachining and LIGA technology also reviewed in [23]. These technologies are not directly compatible to the silicon process, meanwhile the bulk silicon micromachining process can be categorized as the compati-

[1]LIGA is a German acronym for Lithograpie (lithography), Galvanoformung (electroplating), Abformung (molding), the technology for production of high aspect ratio structures

ble one. Microspectrometers based upon grating and interference (filter) principles are recently widely used in many applications, and since the prism based spectrometer is improper for the miniaturization, only these two types of the dispersion elements will be presented in the following.

Grating-based Microspectrometers

A grating-based spectrometer fabricated in silicon using bulk-micromachining techniques was reported by Kwa *et al*. The microspectrometer was integrated with the photodiode array [24, 25], it is shown in Fig. 2.1. The spectrometer was designed for 380 - 720 nm spectral range. It composed of two silicon p-type wafers which were bonded, and an optical path of about 4mm was created with an n-type epilayer, on which electrochemically controlled etching was applied. The dispersive element was made of 32-slits diffraction grating.

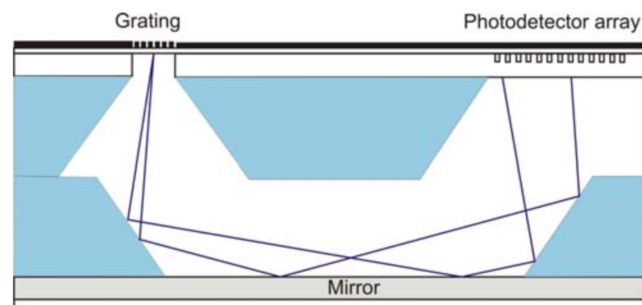

Figure 2.1: *A grating-based integrated spectrometer with photodiode array fabricated in silicon [24] .*

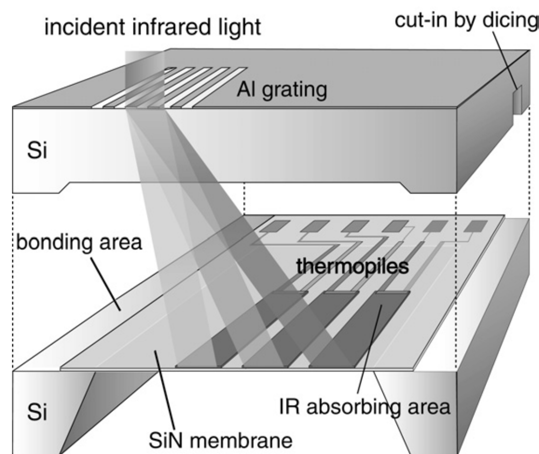

Figure 2.2: *The scheme of an IR grating-based microspectrometer with two wafer approach [26].*

Another spectrometer based on planar waveguide grating coupler in combination with a plano convex lens has been demonstrated by Chaganti *et al*. Within wavelength range of 480 - 640 nm, the spectral linewidth (Full-Width of Half Maximum/FWHM) varies from 0.3 to 4.6 nm. The uniform grating was made of HfO_2 on BK7 glass substrate with SiO_2 as the cladding layer. Two beam interference lithography was used for patterning the waveguide gratings with 401.5 nm in periods and 70 nm in depth [27].
IR grating-based microspectrometer fabricated using two wafers approach by bulk silicon micromachining was also presented by Kong *et al.* [26]. The optical path and slit gratings were made of bulk silicon and aluminium, respectively. Figure 2.2 shows the schematic view of the IR microspectrometer. The grating is formed by 30 or 60 slits with a range of grating constant from 4 to 20 μm. The measured spectral of the spectrometer at 6 μm grating constant revealed FWHM of 0.5 μm at λ of 5 μm.
The microspectrometer manufactured by microParts using LIGA technology is shown in Fig. 2.3 [18]. This technology generally involves polymeric and metal molding process. The devices designed for the UV and NIR range are based upon a monolithic spectrometer chip, comprised of all components i.e. an entrance slit, self-focusing diffraction grating, and deflection mirror, on a single injection-molded part. The near-IR spectrometer has a size of 61x42x16 mm^3, equipped with InGaAs array detector and it covers a range of 1000 - 1700 nm with resolution of less than 16 nm.

Filter-based Microspectrometers

Interference-based spectrometers can be distinguished into three groups, i.e. *Michelson-*, *Mach-Zender-*, and Fabry Pérot filter-based interferometer. Filter-based interferometers are more favorable, since it is not easy to situate the beam-splitter in the other type of interferometers. Moreover, the filter-based spectrometer has relatively higher resolution, and can be tailored for many different wavelength specifications. The Fourier Transform (FT)-based type is actually a variation of the filter type, where the movable detector works to scan the wavelengths [23]. FT-based spectrometers for widely applications in mid- and near-IR range are described in detail in the articles written by Crocombe [6, 15].

A microspectrometer for IR and visible range based on tunable filter fabricated using a new porous silicon batch was reported in [28]. Porous silicon[2] was formed by electrochemical etch process, using silicon nitride mask in hydrofluoric acid. The filters were actuated by a thermal bimorph up to 2 V, and the wavelengths in the visible range were selected with a resolution of approximately 25 nm.
Tunable FP filter fabricated using bulk silicon micromachining was reported by Correia *et al.* in [29] designed for the visible range application. This tunable filter-based microspectrometer consisted of two parallel silver mirrors, with silicon nitride as a supporting post structure, forming a cavity of 1.2 μm. By applying electrostatic actuation only one mirror was tuned on a movable silicon frame. The filter revealed a *finesse* of >30 and a FWHM of <3 nm with silver thickness of 50 nm, and at a voltage of 21 V the displacement of

[2]Electrochemically etched silicon, with pore size in order of nm to μm. Discovered in 1956 by Arthur Uhlir at Bell Labs

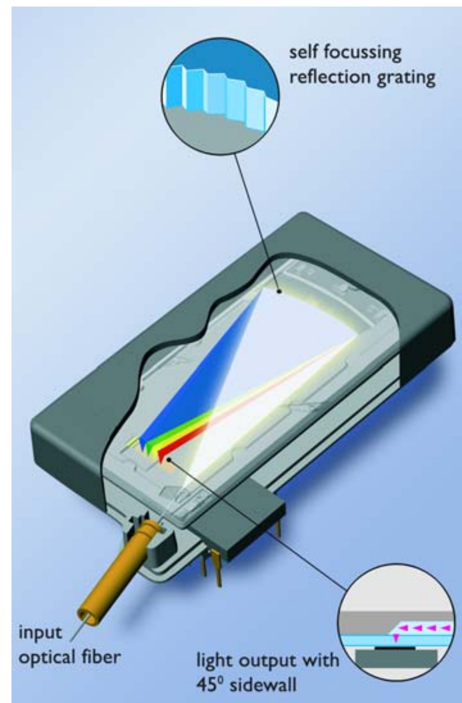

Figure 2.3: *A monolithic 'slab-waveguide' spectrometer manufactured by LIGA process, courtesy of* Boehringer Ingelheim microParts [18] *(later* INSION*).*

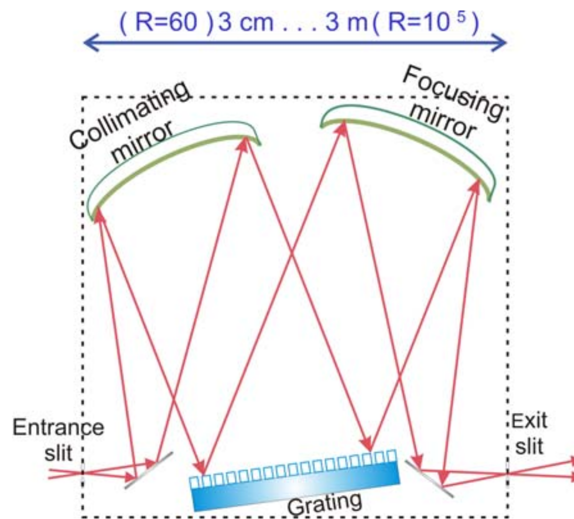

Figure 2.4: *Illustration of the grating-based spectrometer produced by* Carl-Zeiss*. The increase in the number of grating slits influences the resolution.*

450 nm was obtained.

Two wafers approach to build a tunable FP filter-based spectrometer fabricated by bulk

micromachining, was reported by Raley in [30]. The dielectric mirrors formed the tunable filter. Membrane displacement of 250 nm was measured under 100 V of actuation voltage.

Spectral Resolution of the Grating- and Filter-based Spectrometer

The following Fig. 2.4 shows the typical grating-type spectrometer manufactured by *Carl-Zeiss*. The illustration shows that the spectral resolution is getting increased as the number of grating slits N increases, hence, the size of the spectrometer increased as well. If the first mode is applied then resolution R_s of the grating-type can be defined as R_s = N , where N is the number of the grating slits. This condition applied by assuming Fraunhofer diffraction is existing [32]. Larger N leads to higher resolution, which can be accomplished by increasing the optical path length between detector and grating element [23]. In FP filter-based microspectrometers, the spectral resolution can be defined as $R_s = m.F_s$, where F_s is the *finesse* of the filter. If the spectrometer works in the first order mode, that is $m = 1$, then the *finesse*, which is described as $\pi\sqrt{R}/(1-R)$, will determine the resolution. R is the reflectivity of the mirrors that formed the FP filter. Therefore, the high reflectance of the mirrors leads to the high resolution.

Selected materials for the filter is an important key in the fabrication since they can influence the effective *finesse* of the filter, e.g. roughness of the mirror and the reflectivity. Tradeoff between peak transmission and reflectivity is needed to be considered when metal-based filter is used. The stack layers of dielectric mirrors can provide high reflectance, low absorption, and its fabrication can be performed generally with surface micromachining.

Filter Arrays-based Microspectrometer

In the following, the static filter arrays-based spectrometers with relatively high optical transmission are presented. In these kind of filter arrays, no moving part components are included, hence, the imperfect parallelism mirrors can be avoided.

The microspectrometer with an array of 4x4 FP-etalon integrated into a single-chip CMOS had been fabricated by Correia *et al.*; the chip is shown in Fig. 2.5. The wavelength is tuned by having different resonance cavities. To obtain 2^K different thicknesses of SiO_2 layer, K plasma etch steps are required [33]. However, to accomplish a mass production of such spectrometers is infeasible with a customary lithography process.

A high spectral resolution ($R_s = \lambda/\Delta\lambda$) of 210 up to 470 of the filter array-based spectrometer, whose size smaller than 1 cm^3 was reported by Wang *et al.* This spectrometer has 8x16-channel integrated filter array without any moving parts, and a CCD that selects a spectrum in a range of 722 - 880 nm. The different filter cavity thicknesses (SiO_2) were fabricated by 9 deposition steps [34, 35], as shown in Fig. 2.6.

Applying Nanoimprint for the Fabrication of the Arrays of Filter Cavities

The aforementioned previous works generally used silicon substrates and the technologies which were considered to be expensive, for instance the bulk micromachining using

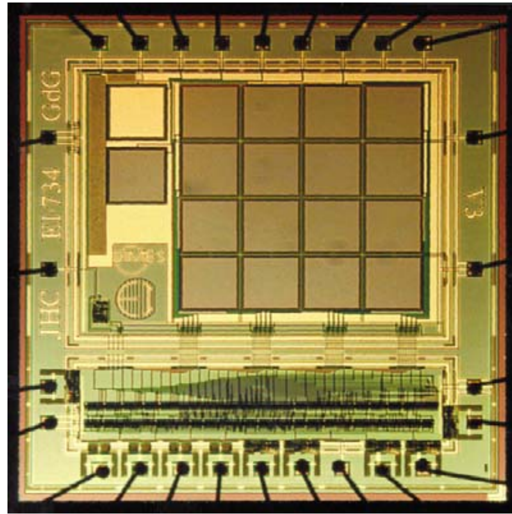

Figure 2.5: *The filter array-type spectrometer where 4x4 FP-etalon were integrated into a single-chip CMOS. Different thicknesses of SiO_2 layer (as the filter cavities) tune the passed wavelengths [33].*

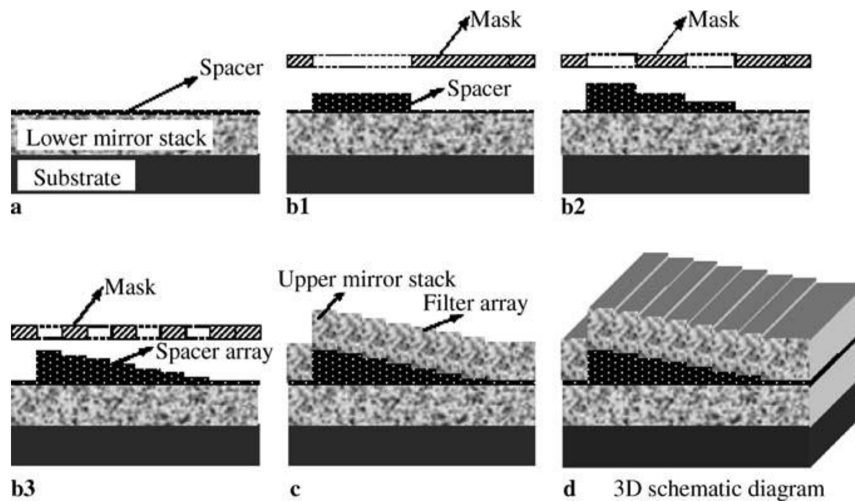

Figure 2.6: *The deposition process to fabricate the filter arrays with different cavities. SiO_2 film was used as cavity material and deposited by 9 steps [34].*

two wafer approach, the electron beam lithography, and the LIGA method.
This work focuses on using low cost technologies for the filter arrays production. Arrays of several static (non-tunable) FP filters have been developed at the institute, with the nanoimprint technology [8]. Nanoimprint technique emerges to provide low cost, uncomplicated and relatively fast process fabrication for the static FP filter arrays. Compared to the utilized fabrication process for the arrays of the aforementioned filters, this imprint

technology enables to attain batch production of the spectrometers. Creating of the different filter cavities in one step process can be obtained by means of a stamp/template nanostructure. Mechanism and fabrication of the stamps required for the imprint process has been patented in [36].
Implementation of the nanoimprint for the tunable filters is a potential low cost technology for mass production of spectrometers. Hence, in this work the compatibility of the UV-NIL polymers to the whole fabrication steps, and the process to remove the cross-linked polymers to obtain the air gap cavity are investigated. Moreover, other low cost technologies, e.g. PECVD and optical lithography, and utilizing of low cost glass substrates are considered for the filter's production.

Chapter 3

Basics of the Optical Filter, Materials and Methods

THE first interferometer developed by Charles Fabry and Alfred Pérot in 1897 consisted of two flat glass plates coated with silver films on their parallel facing surfaces [37]. The incoming light hit on the outer surface of the first plate, and going through the silver coating, the beam was reflected back and forth between the silvered layers for a large number of times. A fraction of the incident light passed through the surface of the second plate for each reflection. At the end, a bundle of parallel light beams emerged at the same angle, as the incident angle of the beams which hit the first plate, and could be converged by a lens.

The principle of a Fabry-Pérot filter will be reviewed in this chapter, and the important parameters such as filter linewidth, free-spectral-range (FSR), and *finesse* will be described. MEMS-based filters fabricated by surface micromachining are reviewed in the second section, followed by the technological processes and materials which were involved in the filter's fabrication described in this work. The characterization methods are presented in the last section.

3.1 Fabry-Pérot Filter and its Optical Properties

A Fabry-Pérot filter comprises of two mirrors parallel to each other and separated by a distance d, forming an optical resonance cavity. Basically there are two types; it is called an interferometer if d is variable, and an etalon if d is fixed. The filter is characterized by constructive and destructive interference of waves in the resonance cavity.
The constructive interference happens when there is a standing wave between the two mirrors, wherein the optical distance between them must equal to an integral number of half wavelengths of the incoming beam. When the cavity is on resonance, this condition allows basically 100% of the beam passes through the filter, and when it is off resonance, almost all the incoming beams will be reflected [38].

Considering that the plane waves reflected between two parallel surfaces P1 and P2 in Fig.

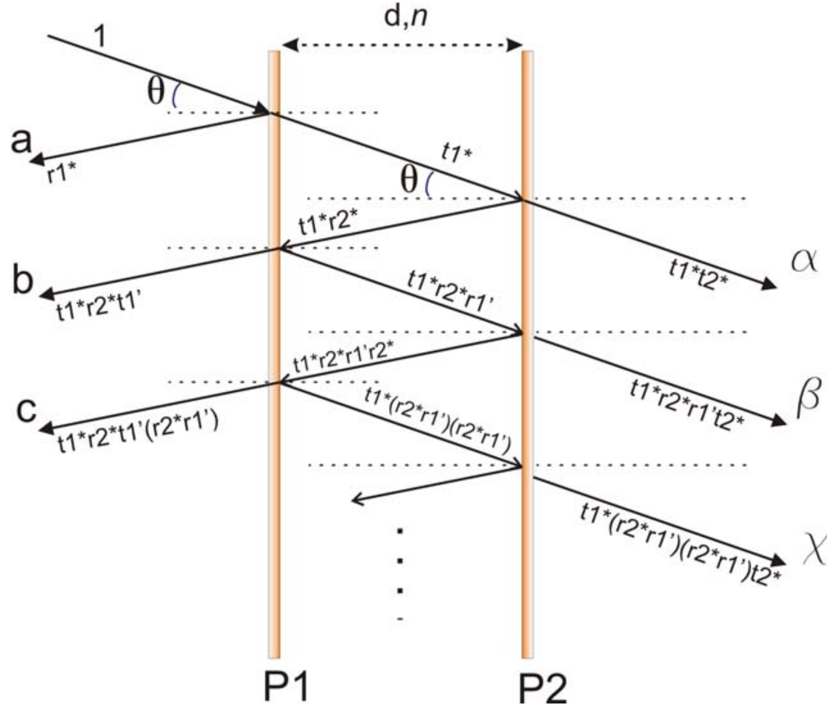

Figure 3.1: *Multiple reflection of plane waves between two plane P1 and P2 parallel surfaces. The amplitude coefficients of the reflected set of beams denote as a, b, c and the transmitted beams as α, β, γ [39].*

3.1 with the distance *d*, and *n* is the effective refractive index of the interspace. Angle θ denotes the angle of incident beam on the surface. Label * is used for the complex reflection and transmission amplitude coefficients from the incident beam that travels from left to right, and label ' for those from the beam which comes right to left.
The output light beams have a phase difference due to distinct path lengths for each beam. This phase lag φ is defined as [39]:

$$\varphi = \frac{4\pi nd\cos\theta}{\lambda} \tag{3.1}$$

The amplitude $E_t(m)$ of the transmitted lights is given by these relations:

$$\begin{aligned} E_t(m) &= t_1^* t_2^* [1 + r_1^{'} r_2^* e^{i\varphi} + ... + (r_1^{'} r_2^*)^{m-1} e^{i(m-1)\varphi}] \\ &= t_1^* t_2^* [1 - (r_1^{'} r_2^*)^m e^{im\varphi} / (1 - r_1^{'} r_2^* e^{i\varphi})] \end{aligned} \tag{3.2a}$$

And for infinite number of beams where $m \to \infty$ the equation becomes

$$E_t \to E_t(\infty) = t_1^* t_2^* / (1 - r_1^{'} r_2^* e^{i\varphi}) \tag{3.3}$$

I_t as the corresponding transmitted intensity can be described as:

$$I_t = |t_1^* t_2^*|^2 / (1 + \left|r_1^{'} r_2^*\right|^2 - 2\left|r_1^{'} r_2^*\right| cos\psi) \tag{3.4}$$

where

$$\psi = \varphi + \epsilon \tag{3.5}$$

ϵ is the correction for phase change. For a single surface, we have *R* and *T* as the surface intensity reflection and transmission coefficients, respectively, where:

$$t^* t' = T; \quad r^* = -r'; \quad r^{*2} = r'^2 = R; \quad R + T = 1 \tag{3.6}$$

For the ideal dielectrics $\epsilon = 0$, and $t^*_2 = t'_1$ and $r^*_2 = r'_1$, hence, for the pair of plane surfaces the energy transmission coefficient can be defined as:

$$I_T = T^2/(1 + R^2 - 2Rcos\varphi) \tag{3.7a}$$
$$= T^2/[(1 - R^2) + 4Rsin^2(\varphi/2)] \tag{3.7b}$$
$$= \frac{T^2}{(1-R)^2}\left(\frac{1}{1 + [4R/(1-R)^2]sin^2(\varphi/2)}\right) \tag{3.7c}$$
$$= [T/(1-R)]^2[1 + G\sin^2(\varphi/2)]^{-1} \tag{3.7d}$$
$$= [T/(1-R)]^2 A(\varphi) \tag{3.7e}$$

where *G* is equal to $4R/(1-R)^2$. Equation $3.7e$ is known as basic Airy formulas for transmission, and $A(\varphi)$ is the Airy shape function [39]. The energy reflection coefficient is given by:

$$I_R = G\sin^2(\varphi/2)[1 + G\sin^2(\varphi/2)]^{-1} \tag{3.8}$$

For the case *R+T = 1* with no surface absorption, the energy transmission and reflection coefficients are complementary and equal to one:

$$I_T + I_R = [T^2/(1-R)^2 + G\sin^2(\varphi/2)]/[1 + G\sin^2(\varphi/2)]^{-1} \tag{3.9}$$

The maxima in transmission will emerge when φ is equal to $2m\pi$

$$\varphi = \frac{4\pi ndcos\theta}{\lambda} = 2m\pi \tag{3.10}$$

This maxima or transmission peak can be expressed in frequency domain as:

$$f_m = m(\frac{c}{2ndcos\theta}) \tag{3.11a}$$
$$= m\,(FSR) \tag{3.11b}$$

where *FSR* is the free spectral range, that is the distance between two adjacent transmission peaks. If the light incidents normal to the etalon, the *FSR* depends only on the optical path length *nd*.

For the normal incidence light and an air gap cavity (*n=1*), the *FSR* in the frequency domain is defined as:

$$FSR = c/2d \tag{3.12}$$

where *d* is the distance between two mirrors, *m* is an integer, λ represents the resonant wavelength in the interferometer, and *c* is the speed of light in a vacuum. Important to

notice that the *FSR* is constant in the frequency domain [38].

If the cavity length *d* is increased, the *FSR* is reduced and ideally the FWHM becomes narrower, as illustrated in Fig. 3.2. The cavity materials used in the simulation by OpenFilter[1] [40], are the mr-UVCur06 polymer and air. The choice of cavity material and length determines the peak transmission and the FSR. The maximum transmission is occured if the optical path length *nd* is equal to $m\lambda/2$.

By increasing the reflectivity, the transmission linewidth or fringe will become sharper, and this can be expressed as the ratio of the separation of successive linewidths, which is known as *FSR*, to the width of the fringe, known as full-width at half-maximum (FHWM). This ratio is called as *finesse*, and it is given by:

$$F_s = FSR/FWHM \tag{3.13a}$$

$$= \pi/\varphi_{1/2} = (\pi/2)\sqrt{G} = \pi\sqrt{R}/(1-R) \tag{3.13b}$$

where the FWHM in frequency domain can be obtained by dividing the *FSR* by the *finesse* [41]:

$$FWHM = f_1 - f_2 = \frac{c(1-R)}{2\pi nd\sqrt{R}} \tag{3.14a}$$

$$= (1/F_s)(c/2nd) \tag{3.14b}$$

hence, *finesse* F_s represents a figure of merit of the filter. It gives information about the filter's ability in transmitting several channels without crosstalk or interferences between them. As shown by the equation $3.14b$, higher reflectivity leads to higher quality of the filter or narrower transmission peak.
High-reflective mirrors that are used to implement the FP filter based on the thin film multilayer structures. In the following the mirrors viz. DBRs will be reviewed.

3.1.1 Distributed Bragg Reflectors (DBRs)

Basically, the DBRs consist of stacked mirrors, which is known as a quarter wave stack mirror. It is composed of layers of dielectric materials with different refractive indices i.e high and low, wherein each layer has a quarter wavelength optical thickness. The beam reflected within the low-refractive-index layer has a phase shift of 180°, while the one reflected within high-refractive-index layer experiences no phase shift. Therefore, all the incident beams which are reflected at successive boundary layers, reappear all in phase at the front surface and they contribute constructively [42].

High refractive index contrast leads to a broad bandwidth of DBRs, it is stated by the equation in the following.

$$\Delta f = \frac{4\lambda}{\pi} arcsin(\frac{n_H - n_L}{n_H + n_L}) \tag{3.15}$$

[1] an open source software. With this software, the optical properties of a filter can be simulated based on data of the thin films or other material measured by an ellipsometer.

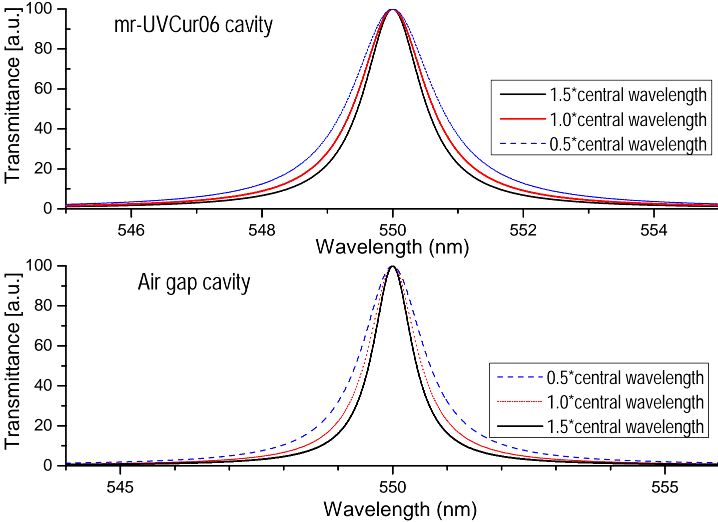

Figure 3.2: *Open-Filter's simulation results of the transmission linewidths. By increasing the length of cavity, the FSR will decrease.*

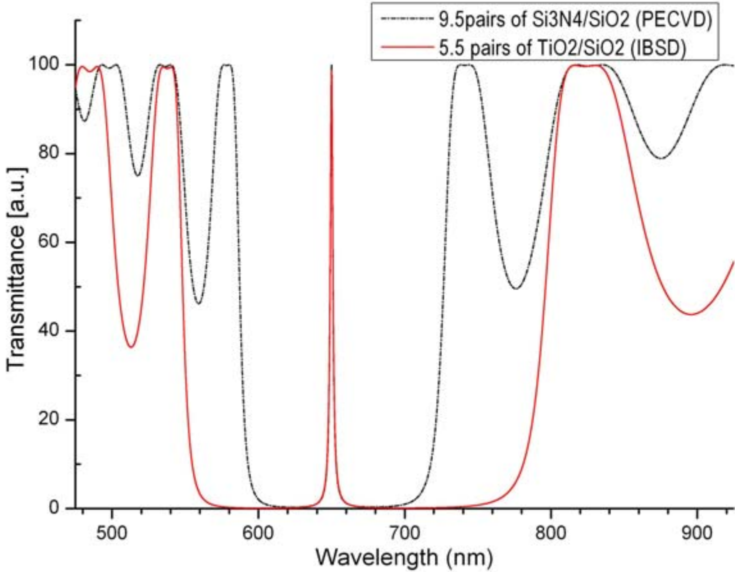

Figure 3.3: *Transmission of two type DBRs-based filters, simulated by OpenFilter, with the central wavelengths at 650 nm. TiO_2/SiO_2 DBRs-based filter exhibits broader bandwidth with fewer pairs of DBRs, due to the higher index contrast compared to Si_3N_4/SiO_2 DBRs-based filter.*

where Δf is frequency bandwidth, λ is the central wavelength, n_H and n_L represents the layer with high and low refractive index, respectively. Due to its higher refractive index contrast, the TiO_2/SiO_2 DBRs-based filter displayed a broader bandwidth with only fewer pairs of DBRs, compared to the one resulted from Si_3N_4/SiO_2 DBRs-based filter.
Figure 3.3 shows the transmission of the two types of DBRs-based filters, one consists of 9.5 pairs of Si_3N_4/SiO_2 and the other has 5.5 pairs of TiO_2/SiO_2 DBRs, whose refractive index contrast is approximately 0.4 and 0.9, respectively.

3.1.2 Electrostatic Actuation

In this work, electrostatic actuation will be applied for tuning the filter transmission peak. Contact electrodes are deposited underneath the bottom DBRs and on the top DBRs. In a Fabry-Pérot interferometer with an air gap cavity (*n = 1*), for the normal incidence light beam, the following relationship can be stated

$$d = m\lambda/2 \tag{3.16}$$

Therefore, changes in the cavity length *d*, will tune the transmitted wavelength λ of the interferometer.
The illustration in Fig. 3.5-top shows the change of air-gap cavity layer due to the actuation. A voltage *V* is applied in the two membranes, induces an electric field *E = V/L* in the gap, and an electrostatic force emerges between the mirrors. Due to this, the filter membranes are displaced or deflected. Another force, that is the mechanical (spring) force, will counteract the displacement caused by the electrostatic force. Hence, the total force at the voltage *V* and the gap *g* is given as [43]

$$F_{net} = \frac{-\epsilon_0 A V^2}{2d^2} + k(d-g) \tag{3.17}$$

where ϵ_0 is permittivity of free space, *A* is the membrane area, *k*is the spring constant, *d* is the gap, or cavity length, at zero spring extension and no applied voltage.
With small pertubation the total force will vary, and can be defined as

$$\delta F_{net} = (\frac{\epsilon_0 A V^2}{g^3} - k)\delta g \tag{3.18}$$

To obtain *g* as a stable equilibrium point, hence, *k* should be defined as

$$k > \frac{\epsilon_0 A V^2}{g^3} \tag{3.19}$$

By increasing the voltage, the equilibrium gap is decreased, and at a certain voltage, called pull-in voltage V_{PI}, the equilibrium will suffer. At pull-in, we have these two conditions [43]:

$$F_{net} = 0 \ and \ k = \frac{\epsilon_0 A {V_{PI}}^2}{{g_{PI}}^3} \tag{3.20}$$

and pull-in occurs at:

$$g_{PI} = \frac{2}{3}d \tag{3.21}$$

Hence, the pull-in voltage V_{PI} is given as:

$$V_{PI} = \sqrt{\frac{8kd^3}{27\epsilon_0 A}} \tag{3.22}$$

How to visualize pull-in phenomenon by plotting the normalized gap as a function of normalized voltage (*V/*V_{PI}) is presented also by Senturia [43]. The graph in Fig. 3.4 shows that stable displacement of the membrane happens for normalized gaps (*g/d*) greater than 2/3.
Another parameter that we review here is the tuning efficiency, which is defined by a ratio of wavelength tuning range to the changes in the cavity length [44]. The illustration for expressing a tuning efficiency η_t of 0.6, simulated with OpenFilter, is shown in Fig. 3.5. η_t can be defined as

$$\eta_t = \frac{\Delta\lambda}{\Delta d} \tag{3.23}$$

The cavity of a half-wavelength is selected for the mr-UVCur06, between the 9.5 pairs of DBRs, corresponded to 212 nm in thickness. The changes in cavity of ±50 nm, leads to the change in wavelength to 620 nm and 680 nm.

3.2 MEMS Surface Micromachining: the Promise

MEMS surface micromachining gives more promising technology to obtain low cost devices. With this technology, automated, reproducible, and batch production, can be accomplished. Bulk micromachining for filters fabrication emerged as well, however, concerning the materials and the technology, it leads to relatively expensive processes [24, 29, 46].
Tunable filter fabricated by surface micromachining technology in silicon, which was designed for 780 nm centre wavelength, was reported by Aratani *et al*, wherein the filter with thinned suspensions resulted in less voltages required for the tuning mechanism. The mirror consisted of polysilicon, silicon oxide and silicon nitride layers, deposited on top of a Si (silicon) substrate. Oxidized polysilicon and PSG (phosphosilicate glass) as sacrificial layers were investigated [47]. Another surface micromachined tunable filter fabricated on Si substrate was reported by Tran [48], it reveals 5 nm transmission linewidth within tuning range of 60 nm. The mirrors were composed of Si-SiO_2 layers and polyimide as sacrificial layer, designed for 1.517 μm centre wavelength.
A torsional tunable filter with continuous tuning range from 1500 to 1600 nm, had been developed by Mateus [49]. DBR pairs made of $Al_{0.1}Ga_{0.9}As/Al_{0.85}Ga_{0.15}As$, and GaAs as the sacrificial layer were used in the fabrication. With this torsional MEMS structure, the discharge problem can be avoided which may happened when the structures collapse onto the substrate. Fabrication of Si_3N_4/SiO_2 DBRs using low cost PECVD process, for

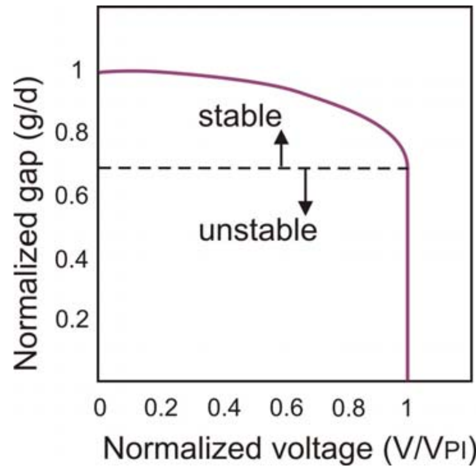

Figure 3.4: *Graph of the normalized gap as a function of normalized voltage to show the stable and unstable displacements for the electrostatic actuator [43].*

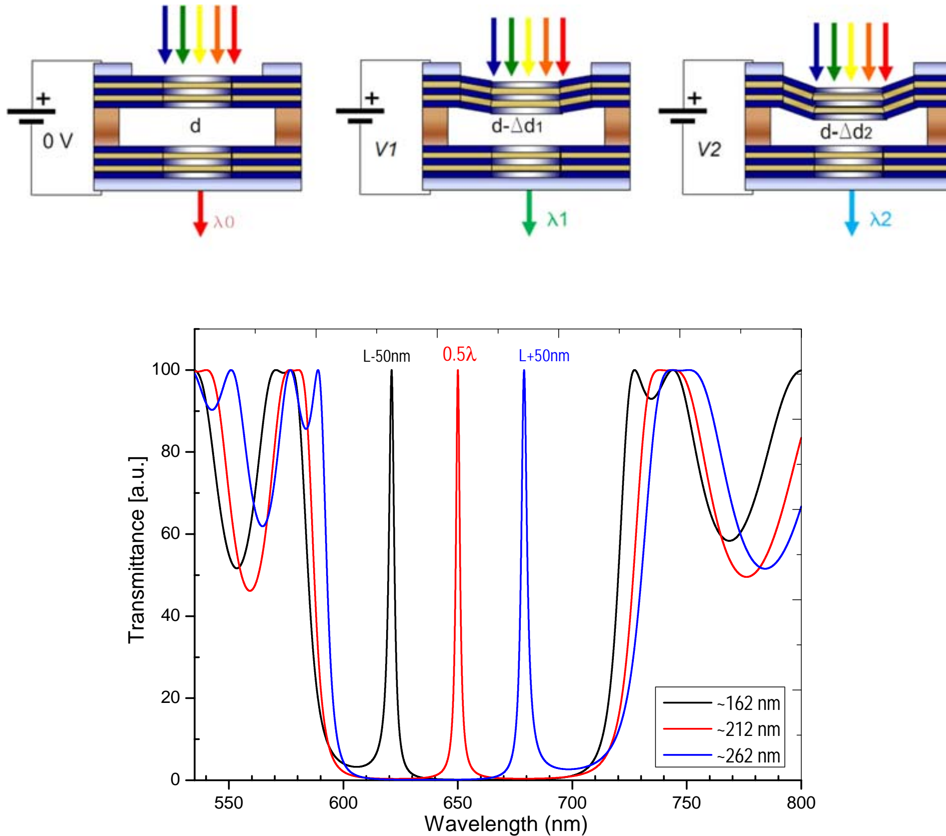

Figure 3.5: *Schematic sideview of the filter during electrostatic actuation, the top DBRs are moved towards the bottom ones. The actuation changes the cavity layer of the filter by applying bias voltage, and a different wavelength passes through (top). Illustration for expressing a tuning efficiency η_t of 0.6, simulated by OpenFilter (bottom).*

a micromachined tunable filter with a photoresist sacrificial layer and silicon as the substrate was reported by Tarraf *et al*. The filter demonstrated a tuning ability of 15 nm/mA at a micro-heater resistance of 2 kΩ under thermal actuation [50].

For the implementation of the filter in this work, the UV-NIL polymers sacrificial layer and glass substrates were used. Materials and methods used in the fabrication of the filters are presented in the following.

3.3 Deposition Methods

The two deposition methods implemented for the dieletric DBRs are briefly described in the following subsections.

3.3.1 Plasma Enhanced Chemical Vapour Deposition (PECVD)

In the presence of the plasma, thin films deposition by means of PECVD can be obtained at low temperatures. Typically the substrate's temperature varies from 100°C up to 400°C. Meanwhile the temperatures required for thin film deposition by means of CVD (Chemical Vapour Deposition) and LPCVD (Low Pressure CVD) are relatively high, 500 up to 850°C [43]. The plasma is ignited by a strong electric field between the two electrodes, the lower electrode on ground potential (where the substrate is located) and top electrode that is driven by a radio-frequency (RF).
Amorphous layers of silicon, as well as silicon oxide can be fabricated by reaction of silane/SiH_4 with N_2O.
Silicon nitride can be produced by reaction of SiH_4 with ammonia (NH_3). In this work, PECVD plant from Oxford was used for fabrication of the Si_3N_4/SiO_2 -DBRs. Deposition rate and thickness of the DBRs were evaluated according to the central wavelength designed for the filters. Stress properties on the layers can be controlled by adjusting process parameters i.e. the silane proportion, process temperature and excitation frequency of the plasma [65].

3.3.2 Ion Beam Sputtering Deposition (IBSD)

Sputter deposition is a physical vapor method of depositing thin films on the substrate (sample) by sputtering material from the target (source). This sputtering is conducted due to the bombardment of the target by energetic particles (ions). Very smooth films with high packing density and good adhesion can be obtained due to high kinetic energy and mobility of sputtered particle (particle energies of 5-50 eV). The separation of the plasma generation and deposition area leads to low damage density and reduction in contamination on the thin films. The most important component of the Ion Beam Sputtering Deposition (IBSD) arrangement is the ion beam sources. The first source is an argon- or xenon-ion beam, and the second one is oxygen- or nitrogen-plasma. A reactive IBSD (RIBSD) plant, IonSys 1000 from company Roth and Rau was used for fabricating of the dielectric TiO_2/SiO_2 DBRs and ITO films. The absorption coefficient and refractive

index can be tuned by varying the oxygen flow. This RISBD use metallic target for the deposition of oxides and nitrides, by using molecular reactive gas or assisted by ion beam.

3.4 UV-NanoImprint Lithography (UV-NIL) polymer

UV-NIL (ultraviolet-Nanoimprint lithography) polymer used as filter cavity layer works as post-structures and also as sacrificial layers, which means it will be removed to obtain an air gap cavity between the DBRs. The determination of the polymer thickness had been performed by test coating on Si-substrate and measured by means of ellipsometry. To fabricate the air gap cavity, adequate materials must fulfill requirements, that is, withstanding the structuring process steps and acting as a sacrificial layer among others. Different types of acrylates-based polymer, i.e. mr-UVCur06, mr-UVCur21 and PAK-01, which are UV-curable polymers were investigated in this work. UV nanoimprint technique has significant benefit over the thermal imprint due to its ability to be processed at room temperature, low pressure, and no thermal-cycle is required during the imprinting process. The crosslinking of these polymers can be performed under UV light exposure in nitrogen ambient.
PAK-01 polymer developed by Toyo-Gosei Co., Ltd, Japan [66], has relatively higher viscosity compared to other polymers. This resin was developed for wide application area. Its mechanical and thermal properties has been analyzed by Hirasawa *et al.* [68], and investigation on the polymer pattern in etching and electroplating environment has been reported by Fukuhara *et al.* [69]. Technical data of the three polymers are shown in Table 3.1. The processes regarding spin-coating of these polymers are given in the appendix (B.4).

3.5 Dry Etching Process: Tools Overview

Structuring of the dielectric mirrors requires an anisotropic etch process which is most effectively performed by plasma etching. Deep plasma etching for MEMS applications using RIE process is widely used nowadays [70–73].
This type of dry etching process, and the two reactive ion etching (RIE) machines used for lateral structuring of the DBRs, are described in the following. The barrel plasma etcher used for etching of the polymer will also be briefly reviewed.

Processes involved in the dry etching consist of generation of gas particles, transporting these particles to the target substrate, etching and removal of etch byproducts [75]. Two components, i.e. chemical and physical bombardment, can be performed in RIE, to obtain anisotropic plasma etching process. Chemical etching is held by these fluorine radicals and neutrals of the plasma. Physical etching is performed by ion bombardment. The illustration in Fig. 3.6 shows isotropic and anistropic profiles yielded by dry etching process, with this process we can tune the profile. The isotropic profile is where etch rate is independent of the direction; it is found generally in wet etching process.
Inert gas Ar (Argon) is used in the process representing the physical etching or ion assisted

Table 3.1: Technical data of mr-UVCur06 and mr-UVCur21 [courtesy of *micro-resist-technology GmbH*], and PAK-01 [courtesy of *Toyo-Gosei Co.,Ltd*]

UV-Curable Polymer	mr-UVCur06	mr-UVCur21	PAK-01
Refractive index	1.54@500 nm	1.494@500 nm	1.518@589 nm
Coating method	spin coating	spin coating	spin coating
Curing process	320-420 nm in vacuum	320-420 nm in vacuum	300-370 nm in vacuum
Smaller feature size (resolution)	sub-50 nm($\leq$30 nm)	$<$ 30 nm	20 nm
Viscosity	14 mPas	2.2 mPas	60 mPas (54.30 cSt)
Ready-to-use solutions for various film thicknesses (3000 rpm)	240 nm	300 nm	3690 nm
Adhesion promoter	mr-APS1	mr-APS1	TI-Prime*
Diluter	mr-T 1070	mr-T 1070	Ether*
* investigated in this work			

etching reaction [76]. Sulfur hexafluoride SF_6 as a gas source of *F* (fluorine) atoms is used for etching oxide films. The gas can be utilized for dry etching of silicon nitride. Another source of *F* atoms is provided by a fluorocarbon gas CHF_3, hence, the CHF_3 is also involved in the structuring of the DBRs. Some reactions in the following may happened in plasma etching of the DBRs [77, 78]:

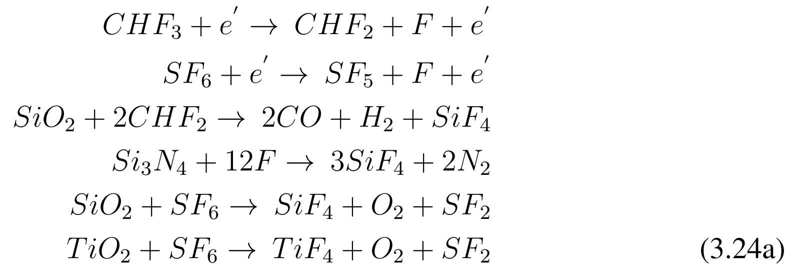

$$
\begin{aligned}
CHF_3 + e' &\rightarrow\ CHF_2 + F + e' \\
SF_6 + e' &\rightarrow\ SF_5 + F + e' \\
SiO_2 + 2CHF_2 &\rightarrow\ 2CO + H_2 + SiF_4 \\
Si_3N_4 + 12F &\rightarrow\ 3SiF_4 + 2N_2 \\
SiO_2 + SF_6 &\rightarrow\ SiF_4 + O_2 + SF_2 \\
TiO_2 + SF_6 &\rightarrow\ TiF_4 + O_2 + SF_2
\end{aligned}
\tag{3.24a}
$$

CO_2, COF_2, SO_x, SO_xF_x or TO_xF_x are etch byproducts that can be produced by the process. They are volatile, and some of them can also induce polymerization on the wafer surface or on the chamber wall. However, they can be removed easily by pumping or by means of ion bombardments. The readers who are interested in the reactions of dissosia-

tion and excitation for SF_6 and Ar gas flow rates can refer to [79].

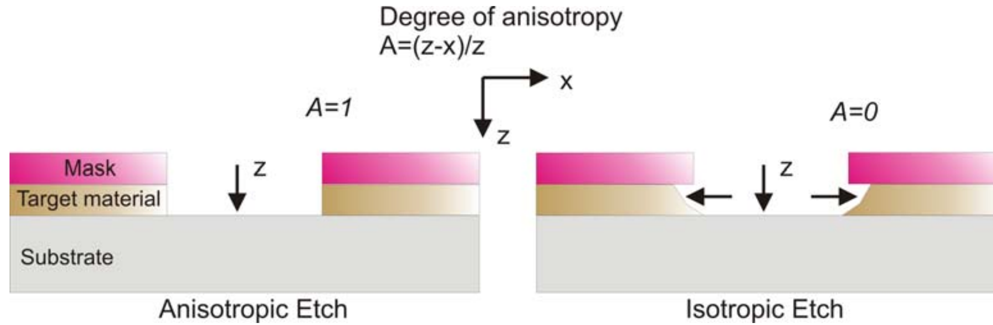

Figure 3.6: *Scheme of typical anisotropic and isotropic etch.*

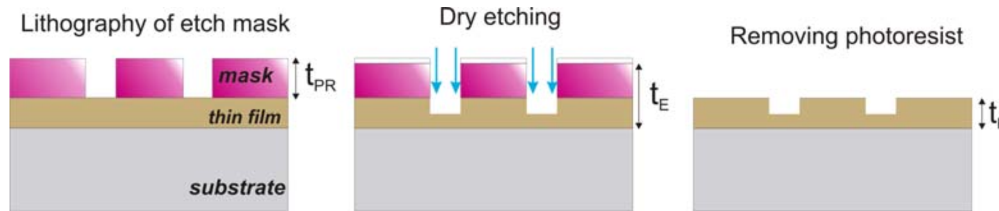

Figure 3.7: *Scheme for determination of the material thicknesses to calculate the etch rate and etch selectivity.*

Determination of the etch rate and etch selectivity

The determination of the etch rate and etch selectivity is accomplished by measuring the thickness of the structure after etching process, with and without the etch masks on it. The mechanical profilemeters, DEKTAK IIA and Ambios, are used for this task. Etch profiles are observed under a scanning electron microscope (SEM) and an optical microscope. Surface roughness can also be measured using a white light interferometer (WLI). The equations below show the calculation for the etch rate and etch selectivity, and the image in Fig. 3.7 illustrates the scheme. The thickness of the etch mask is noted as t_{PR}, and thickness of the sample after etching process as t_E. Thin film material's thickness after removing the etch mask is t_F. Hence, E_F represents etch rate of the thin film and etch selectivity *S* is defined as E_F over the E_{PR} i.e. etch rate of the mask.

$$E_F = t_F/etch\,time \tag{3.25a}$$

$$E_{PR} = (t_{PR} - (t_E - t_F))/etch\,time \tag{3.25b}$$

$$S = E_F/E_{PR} \tag{3.25c}$$

Several etch phenomena that can be detected in the etching process are illustrated in Fig. 3.8. Purely chemical etching is isotropic and very selective, it is caused by neutrals or

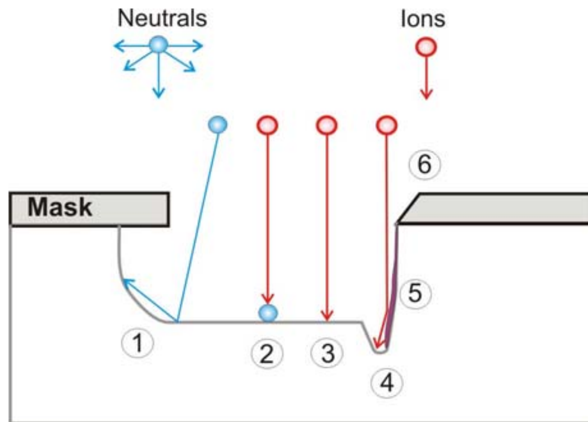

Figure 3.8: *Several processes in plasma etch (redraw after [80]). (1) Chemical etch; (2) Ion enhanced etch; (3) Physical etch; (4) Trenching; (5) Sidewall pasivation; (6) Mask erosion.*

radicals only. Ion enhanced etching involves neutrals and ions. The ion energy stimulates the chemical reaction, or it can remove the polymer (polymerization) caused by etch byproduct. This process is anisotropic and selective. Physical etching is performed by ions, hence, it is anisotropic and non-selective. Trenching effect can probably happen due to ion deflection from the sidewalls, or affected by electric field of charged mask. Sidewall passivation can be caused by deposition of non-volatile materials, e.g. etch mask and etch byproduct. The passivation is enhanced by ion bombardment. Moreover, ion bombardment can also effect erosion of the etch mask, and induces surface roughness [80].
Sidewall geometries in anisotropic etching process can be defined as given in the following. The slope angle α of the etch film which is directly proportional to the etch rate ratio (E_F/E_{PR}), which is known also as the selectivity of etching process, is given as [78]:

$$\tan\alpha = (E_F/E_{PR}).\tan\alpha_m \tag{3.26}$$

The equation shows that slope angle of the etch mask α_m influence the slope angle of the etched structure profile (the film material), however, if etch selectivity in the etching process is high, it can help to increase the slope angle of the etched profile.
To achieve sufficient etch depths and smooth surface profiles of the mirror structures, the etching process can be controlled by evaluating the etch rate and etch selectivity. Therefore, in this work these two parameters are investigated.

3.5.1 Capacitively Coupling Plasma - Reactive Ion Etching

Some of the etching processes were performed in the Capacitively Coupling Plasma (CCP) - RIE provided by Castor-Pollux. This parallel-plate etcher has medium plasma density (ion 10^9 and 10^{10} cm^{-3}), with pressure of 10^{-3} until 10^{-1} Torr.
The gases are fed into the chamber through mass-flow-controllers (MFCs). Plasma chamber wall is grounded, while the radio frequency (RF) generator (with frequency of 13.56 MHz) via a blocking capacitor is connected to the substrate table's electrode. The target sample is placed on the RF driven electrode. Electrons are accumulated at the chamber wall, hence, the wall charges up negatively with respect to the plasma potential. Since the area of the substrate table is much smaller compared to the chamber wall, it charges

up more negatively, therefore, it refers as cathode. The potential at the cathode and the chamber wall (anode) follows this equation:

$$\frac{V_a}{V_c} = (\frac{A_c}{A_a})^y \tag{3.27}$$

where *a* and *c* represent anode and cathode, respectively, with their voltage *V* and area *A*. The exponent *y* is between 1 and 4, that depends on the applied theory and condition of plasma [78]. The difference V_c - V_a is called dc bias voltage, which is always negative, hence, the negative sign is sometimes omitted when declaring the values. This voltage can estimate the difference potential between the plasma and the cathode (since the chamber wall's potential is close to the plasma potential), that is the accelerating voltage for the ions impinging onto the cathode [81]. Scheme of a typical parallel plate RIE reactor is illustrated in Fig. 3.9.

3.5.2 Inductively Coupling Plasma - Reactive Ion Etching

Low and medium plasma densities can be created by a capacitive coupling, meanwhile an inductively coupling plasma (ICP) type provides high plasma densities. Compared to the CCP type wherein high energy ion bombardment is generated, lower ion bombardment energy can be produced in the ICP. In the CCP reactor the ion energy and ion density cannot be controlled separately.

The etching experiments in an inductively coupled plasma-reactive ion etcher (ICP-RIE) are performed in the Oxford Plasmalab 100 equipped with an ICP 180 system. The plant has separate RF generators for the ICP and electrode/cathode, therefore, enables an independent control of ion density and ion energy. Maximum coil power (ICP) of 3000 W and maximum RF power of 300 W are available for the process. High density plasma of 10^{11} up to 10^{12} cm^{-3} can be generated in this plant. Scheme of an ICP-RIE plant is shown in Fig. 3.10, with a frequency of 13.56 MHz drives the parallel plate reactors on cathode where the sample is located, and another one for the inductive coupler (coil or ICP power). The lower electrode bias adjusts the ion bombardment, while the ICP power generates and excites the plasma, hence, it adjusts the plasma density. The load-lock wafer entry for loading of the sample is provided, allowing permanent vacuum in the chamber [81].
For a certain purpose, an etching process can also be run in the so called *RIE-mode*, that is an etch condition without using the ICP power. Some experimental results regarding this etch condition will also be presented, that is for structuring of Si_3N_4/SiO_2 DBRs in the ICP plant.

3.5.3 Barrel Plasma Etcher: Oxygen Plasma

The process in a barrel plasma reactor is mostly pure chemical and isotropic, and generally required for removing remnants of photoresist and polymer. This reactor type is categorized as a low density plasma reactor, with pressure around 10^{-1} to 1 Torr, and no

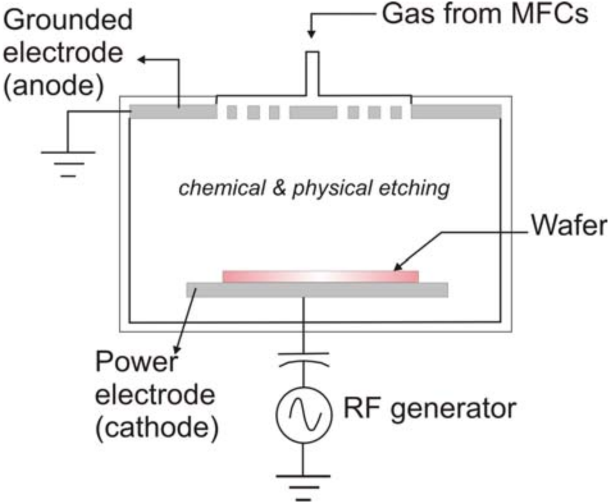

Figure 3.9: *Scheme of a typical paralel-plate CCP-RIE reactor (redraw after [78, 82]).*

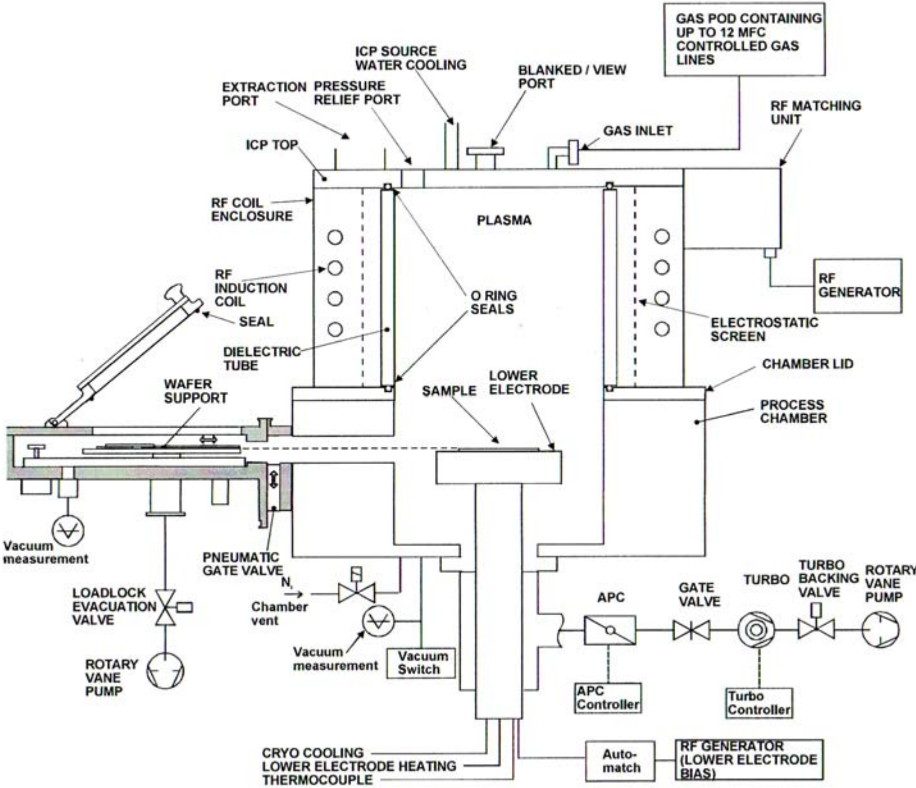

Figure 3.10: *Scheme of an ICP-RIE plant [81].*

temperature control. RF bias source is used and coil or electrodes are arranged outside the vessel. In these experiments, the oxygen plasma process in this reactor is used for underetching of the polymer sacrificial layer, de-scum or stripping of photoresist, and for cleaning of the substrate.

3.6 Filters Characterization Methods

The two instruments which were used for characterizing of filter's optical and mechanical properties are briefly presented in this section.

3.6.1 Microscope-Spectrometer's Set-up Measurement

A microscope-based spectrometer is used for measuring the optical properties of the filters. The system has a short inspection time, the capability to measure an area of several μm, and is able to show a real image of the observed structure. The measurement set-up is depicted in Fig. 3.11.
Two halogen lamps serve as the white light sources, covering spectral range from 400 up to 900 nm. The microscope objective lens with three different magnifications are used to focus the incident light onto the sample surface, and to observe the filter structure. A translation stage where the sample is placed, can be moved to x, y and z direction for scanning of the sample. A transmitted light is selected, and coupled to the fiber connected to the spectrometer by a decoupling device that is equipped with an adjustable diaphragm. A recorded light is evaluated by HR2000 spectrometer (from Ocean Optics), subsequently the transmission and/or reflection spectra are plotted on the monitor by means of its software OOIBase32. An image of the sample or the observed structure is captured by a CCD camera and displayed as well [89]. Calibration of the set up is performed by measuring the reflection beam before the measurement of the filter properties. Aluminum of 100 nm in thickness deposited on a gass substrate is used as the reference. With this reference signal, the transmission and reflection spectra can be calculated automatically by the OOIBase32 software. For the tuning purpose, two needle probe kits are provided, to connect the top electrodes on the top mirrors, and the bottom electrodes located on the glass substrate. The needles are connected to the voltage supply, where the voltage bias can be adjusted manually.

3.6.2 White-Light Interferometer

The mechanical properties of the filter are measured under a white light interferometer (WLI) using Zygo NewView 5000 equipped with an analyzing software MetroPro. WLI is a well-known reliable profiling method for analyzing three dimensional structures, e.g. step heights and surface roughness, in engineering or MEMS applications [91, 92]. The work principle of the scanning WLI is illustrated in Fig. 3.12 and described as the following. The incident light from microscope is split into two beams, one goes to a reference surface and the other beam hits the target sample. Both of light beams are then reflected and directed onto the camera. Interferences between the two lights basically perform an

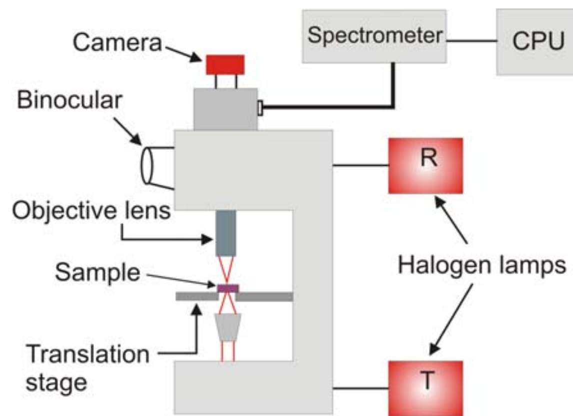

Figure 3.11: *Microscope-spectrometer: system set-up for optical properties measurement (re-draw after [89]).*

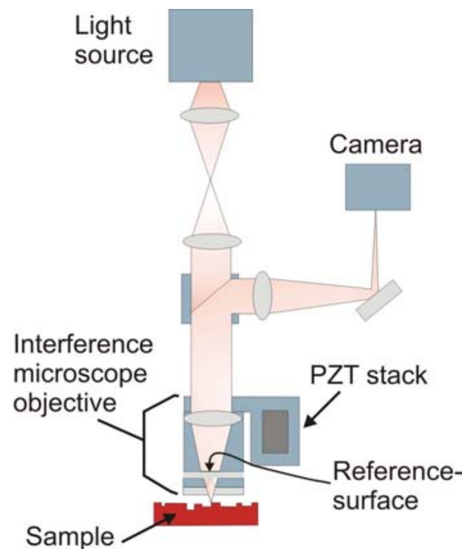

Figure 3.12: *A scheme of the WLI Zygo NewView 5000 [90].*

image of dark and light lines, named fringes, that represent structure of the sample surface being measured. Scanning of the sample is done by vertically moving the interferometric objective with a piezoelectric transducer (PZT), while a video system catches the intensities at each camera pixel. MetroPro software modifies the intensities into images. Lateral detections (in plane of the structure surface) are performed by defining the pixel size from the objective's field of view, and vertical detections (perpendicular to the structure surface) are performed interferometrically [90].

Using an application provided by MetroPro, an automatic analysis of the obtained data is enable, that is by comparing two surfaces, the ´mask´ (or mesa structure) and the reference surface which is unchanged with the applied voltages. The values represent the height difference between these surfaces are sequentially stored, and they can be evaluated. The concept and the program which was made for this automatic measurement was reported

detail in [93].

Chapter 4

Filter Structure Design

DESIGN and the fabrication process of MEMS-based Fabry-Pérot filters will be presented in this chapter. The fabrication depends on some fundamental processes, e.g. film deposition, lithography, and structuring of the Distributed Bragg Reflectors (DBRs). The design of the filter arrays for the color sensor or spectrometer applications are described in the second section. Numerical analysis on the filter membrane displacements in order to find the optimal filter geometric structures, together with the results are presented in the last section.

4.1 Filters Technological Fabrication

Surface micromachined Fabry-Pérot filters in this work utilize low-cost materials and technology processes. The illustration in Fig. 4.1 shows the filter's fabrication process.

(a) A glass substrate, with thickness of 0.7mm, is prepared with the bottom electrode, and subsequently the bottom DBRs are deposited on top of it. Afterwards, UV-NIL polymer as the cavity layer is coated over the bottom DBRs, and then the top DBRs is deposited on the polymer (Fig. 4.1-a).

(b) The patterning of the etch mask is brought by an optical lithography, if a photoresist etch mask is used, as shown in Fig. 4.1-b. This lithography step is followed by a lift-off or wet etching process if a hard etch mask is used in the dry etching process of the DBRs.

(c) Anisotropic lateral structuring of the top DBRs is performed using RIE process (Fig. 4.1-c) in the CCP- or ICP-RIE.

(d) Removing of the etch mask, it can be performed completely in a solvent, in an oxygen plasma, or in an etchant solution (Fig. 4.1-d).

(e) Oxygen plasma is used to remove the polymer sacrificial layer, to perform an air-gap cavity and release the filter membrane (Fig. 4.1-e). The membrane displacement can be estimated with a model simulation.

(f) The top electrodes are deposited on the top of the DBRs (Fig. 4.1-f). The filter is actuated electrostatically by applying bias voltages.

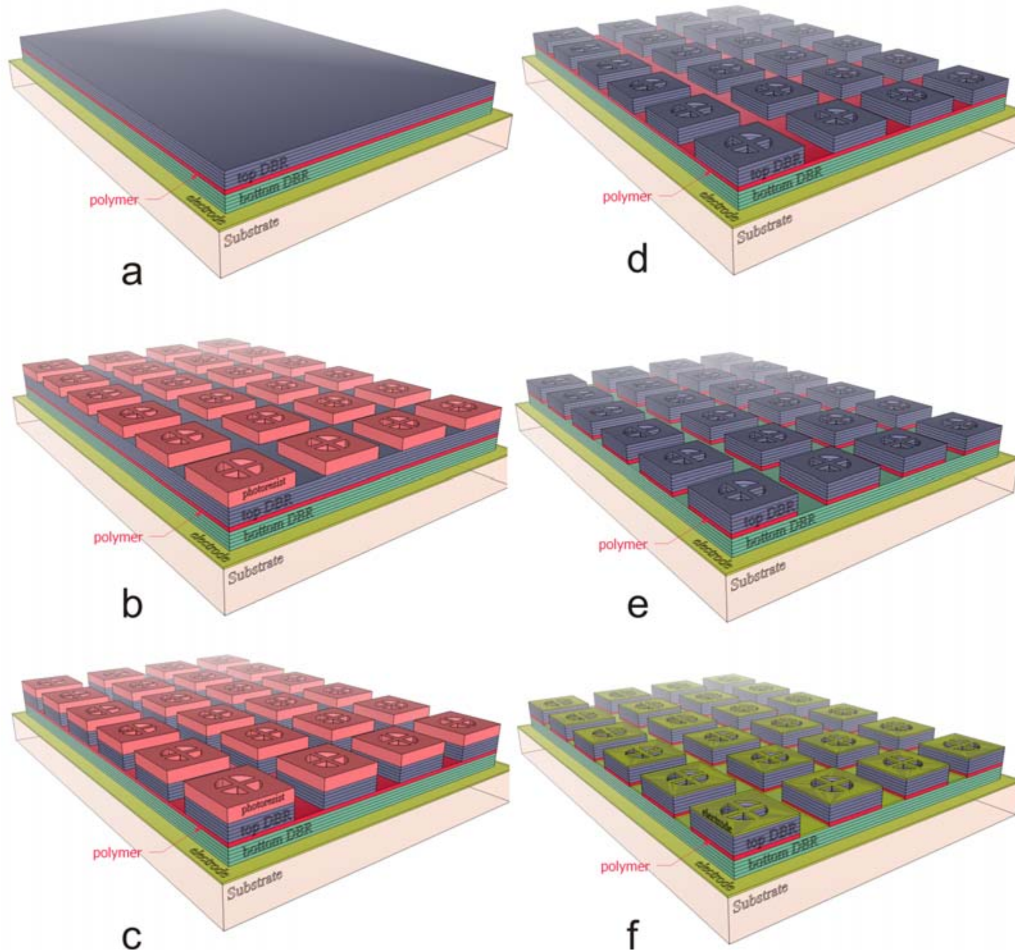

Figure 4.1: *Overview of the filter fabrication process.*

The filters consisted of the top and bottom mirrors made of dieletric materials, and a cavity layer. The center wavelength for the transmission linewidth was chosen between 550 to 650 nm. The optical thickness of each DBRs-pair is a half-wavelength, and a quarter-wavelength for each dielectric layer. One pair, or one period of DBRs consisted of the alternated Si_3N_4/SiO_2 or TiO_2/SiO_2 layers, that were deposited by Plasma Enhanced Chemical Vapour Deposition (PECVD) or by Ion Beam Sputtering Deposition (IBSD), respectively. Designing 9.5 pairs of Si_3N_4/SiO_2 was the optimal choice, concerning high reflectivity of the mirrors and filter transmission linewidth. Approximately 125 nm of stopband was achieved. This choice based on the simulation and measurement results, as shown in the Fig. 4.2. From the simulation results, the filter that consisted of 23.5 pairs of DBRs showed the sharpest linewidth of transmission, however, the measurement result

showed that higher mirror pairs resulted in high absorption, hence no spectral transmission was observed.

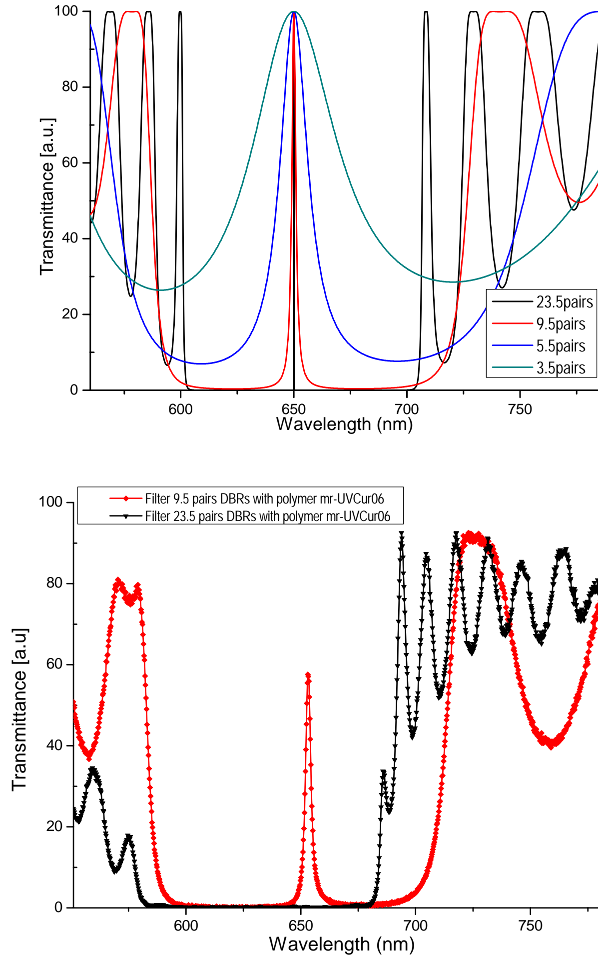

Figure 4.2: *Simulation of the filters with different pairs of Si_3N_4/SiO_2 DBRs (top). Measurement results of the 23.5 and 9.5 pairs of DBRs-based filters, where the mr-UVCur06 was used as the cavity layer material (bottom).*

TiO_2/SiO_2 DBRs-based filters were fabricated as well in this work. Since these TiO_2/SiO_2 DBRs have higher index contrast materials, they lead to broader filter stopbands than the ones from Si_3N_4/SiO_2 DBRs with only fewer number of layers (Fig. 4.3). UV-NIL polymers were used as filters cavity layer material, as mentioned in the previous chapter, they worked as sacrificial layer and supporting post structures. The detail of spin coating process of the polymers are given in the appendix. The adhesion to the DBRs, and the underetching process of the polymers are described in Chapter 5 and 6.

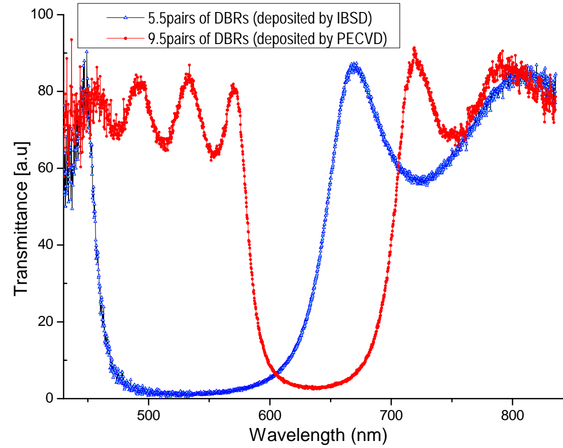

Figure 4.3: *Measured transmission bandwidths of 5.5 pairs of TiO_2/SiO_2 DBRs and 9.5 pairs of Si_3N_4/SiO_2 DBRs. Since TiO_2/SiO_2 has higher index contrast, only few number of pairs of DBRs are required to obtain broader bandwidth, and higher reflectivity.*

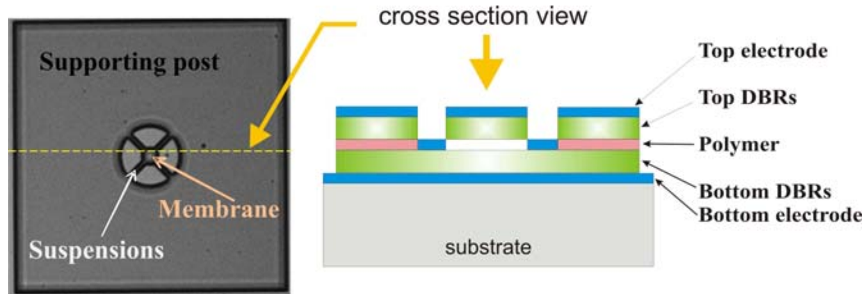

Figure 4.4: *A micrograph of one filter element (left) and its cross section (right). The filter was formed by top and bottom DBRs with air gap as the resonance cavity.*

4.2 Filter Arrays for the Sensor Application

Filter structures design in the IMA3-photomask were used for the initial experiments in this work, to investigate the properties and the whole process flow and materials that are suitable for the fabrication. Only one photomask i.e. for patterning filter structure, called mesa which consists of membrane with the suspensions and the supporting post, was required in the first design. The bottom and top electrodes were not structured. The illustration of this first design is shown in Fig. 4.4, a filter structure with four suspensions and its cross section are presented. The air gap cavity will be obtained after the removing of the polymer sacrificial layer. The fabrication process flow for the first design is shown in Fig. 4.1.

The second design for tunable optical filter array uses two photomasks, i.e. top electrode and mesa photomasks. In this work, top electrode photomask is used for patterning Al top electrode. Microscopic top view of the filter membranes with three suspensions can be seen in Fig. 4.5, small holes in the middle of each membrane are not covered by a reflective material film, therefore, the optical properties of filters can still be measured by observing the transparent membrane centre. A mesa photomask is used for lateral struc-

turing of the top DBRs, wherein the filter structures are designed in arrays, and according to the post structures around the filters, they can be actuated separately or simultaneously.

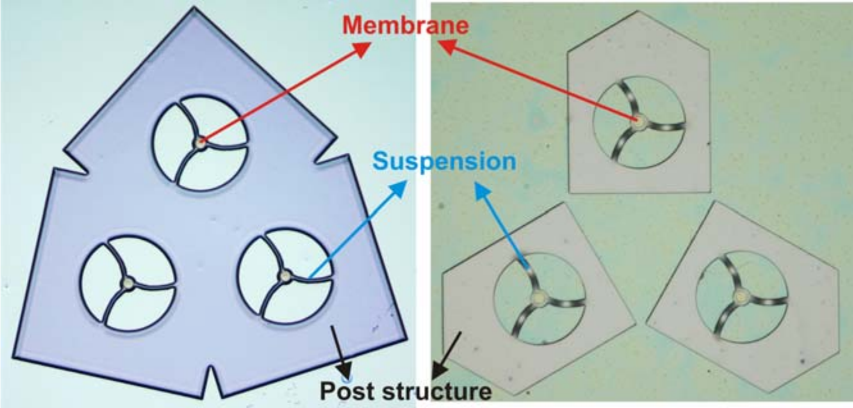

Figure 4.5: *Microscope images of the filter arrays, where each filter membrane has three bent suspensions, and the post structures connected together. These three filters can be actuated simultaneously (left). Separated actuation (right) for each filter can be made also for these designs.*

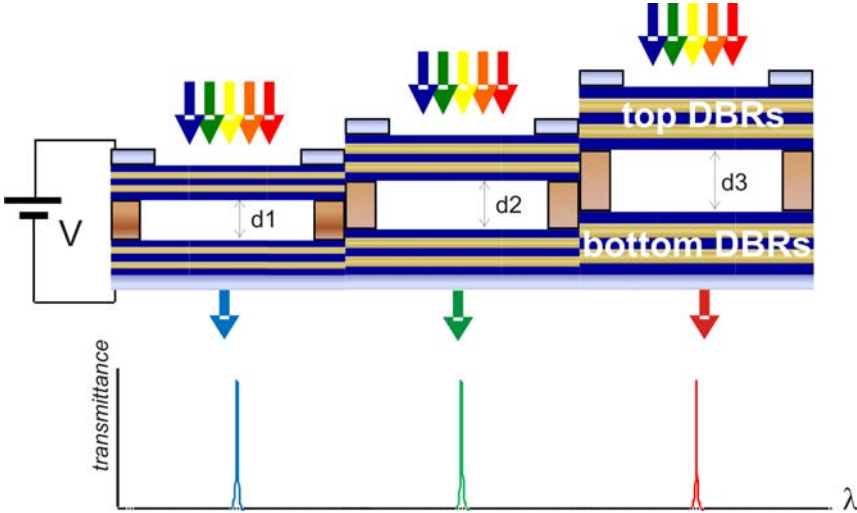

Figure 4.6: *An Illustration of filter arrays with three stopbands arranged in series, hence, a broad tuning range can be achieved.*

Three stopband photomasks and a bonding photomask (for patterning of the bottom electrodes), are later produced for the third design, wherein the filters are ready to be integrated to the detector (CCD or pin diode) array for the color sensor implementation. Experimental results regarding the third design will not be reported in this work. The

three stopbands are designed for the arrays, regarding the filters which composed of three elements. Three filters with different central wavelength are assembled in an array according to the structure of detector array which is designed for the color sensor. As illustrated in Fig. 4.6, broad tuning range and higher spectral resolution can be attained with these stopbands, and applying nanoimprint technology to obtain different thicknesses of the filter cavities will benefit the production. The template fabrication and the imprint technology will not be discussed here. The experimental results that will be reported in the next chapters are the preliminary ones, concerning the first and the second design, that can be used further for spectrometer applications.

4.3 Numerical Analysis on Filter Geometric Structures

In this section, a model simulation presents to examine the displacement or bending of the filter membrane due to the stress in the dielectric materials. The purpose of this simulation is to investigate the geometric shape and size of the DBRs-based filters that influences the displacement of the filter membrane, since various structures are introduced in the filter-arrays design. Simulation on the Si_3N_4/SiO_2 and TiO_2/SiO_2 DBRs material system are presented.
A numerical modeling tool, FEMLAB (later Comsol Multiphysics)[1] is used for this task. With this software, conventional models concerning one branch of physics can be extend to multiphysics models that address multiple branches of science and engineering. The software applies Finite Element Method (FEM) to solve the equations that describe a model. FEM theory in the structural analysis uses the virtual work principle approach for solving the displacement formulation [43]. Review on basic theories regarding the model simulation such as theory of the thin plate, the elastic energy and the virtual work principle, are given in the appendix.
Since the FEM is only a tool for approximating the real geometric shape of structural elements, hence, it is error-prone. Accuracy of the FEM solutions depend on the capability to accurately perform the meshing of the elements, and accurately approximate influence functions, that is boundary elements method for the displacements and stress [94].
Solid-stress-strain application mode as one of the modes for analyzing structural mechanics provided by FEMLAB, is selected to evaluate the displacement of the top mirrors viz. the filter membrane. How to define the material properties, sources and boundary conditions used for the model will be presented in the following.

4.3.1 Membrane Displacement due to the Stress

In this subsection, filter geometric structures that are used in the model are described. Some structures are depicted in the following. The metal layers as contact electrodes are omitted in the model simulation, only multilayer of the dielectric materials will be considered. Filters with membrane diameter of 20 μm up to 70 μm and a number of

[1] FEMLAB/Comsol Multiphysic is the software engineering tool that performs partial differential equation (PDE)-based multiphysics modeling to solve many kinds of science and engineering problems.

suspensions with different lengths and widths, are introduced. Filter structures with varied three suspensions are illustrated in Fig. 4.7, we can see that larger 'trench' diameter leads to longer suspensions. The suspension sizes are considered in the model simulation, meanwhile the supporting post structures will not be included, and the edge of suspensions will be fixed as declared in the boundary settings.

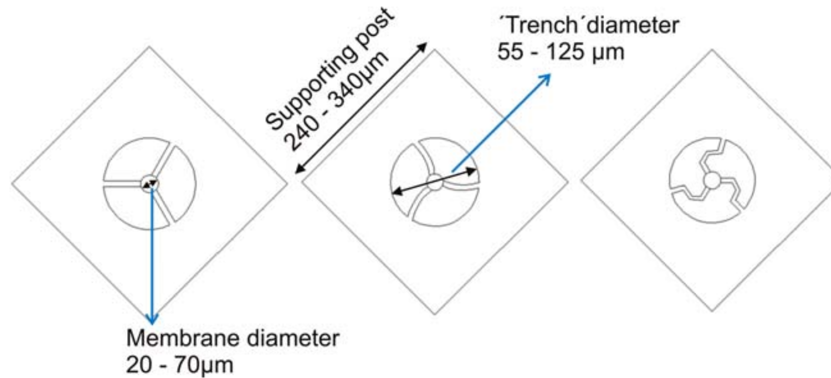

Figure 4.7: *Three mesa filter structures with three suspensions which have different geometric shapes: straight (left), bent (middle) and curl-bent (right) suspensions.*

Multilayer DBRs: Equivalent Material Parameters

The model considers only the top DBRs that consists of a certain pairs of Si_3N_4/SiO_2 layers deposited by PECVD, or the TiO_2/SiO_2 layers deposited by IBSD process. Material properties required for the model are Young's Modulus, Poisson ratio, density and thermal expansion coefficient. Treating one material layer in the simulation leads to a very efficient computation time and reduce the complexity, hence, bulk equivalent materials system calculated by MATLAB[2] will be employed representing the multilayer dielectric materials. These equivalent materials system had been investigated by Vasu [95] to obtain the material properties that represent the pairs of DBRs being used.

Si_3N_4/SiO_2 DBRs

The 9.5 pairs of Si_3N_4/SiO_2 DBRs are selected for the filters due to their optimal bandwidth and high reflectivity. The first and second column shown in Table 4.1 are the Si_3N_4 and SiO_2 material data, respectively, where the parameters were selected from [96]. The third column shows parameters of the bulk equivalent material representing 9.5 pairs of the DBRs.

TiO_2/SiO_2 DBRs

The 5.5 pairs of the TiO_2/SiO_2 DBRs is selected for the model, based also on the optimal optical properties of the filter, for instance its broad bandwidth and high reflectivity. Since index contrast of those dielectric materials is relatively high, their physical thicknesses are less compared to the Si_3N_4/SiO_2 DBRs.

[2]MATrix LABoratory, a high level technical computing software.

Table 4.1: Parameters of the DBRs used in the model I: Si_3N_4, SiO_2 and the bulk equivalent material (of 9.5 pairs of Si_3N_4/SiO_2).

Parameter	Si_3N_4	SiO_2	Bulk equivalent material
Young Modulus	3.23e5 MPa	7e4 MPa	1.86e5 MPa
Poisson ration	0.25	0.17	0.2067
Density	3100 (kg/m^3)	2300 (kg/m^3)	2670 (kg/m^3)
Thermal expansion coeff.	2.8e-6 (/K)	3.5e-7 (/K)	2.3e-6 (/K)

Table 4.2: Parameters of the DBRs used in the model II: TiO_2, SiO_2, and the bulk equivalent material (of 5.5 pairs of TiO_2/SiO_2 DBRs).

Parameter	TiO_2	SiO_2	Bulk equivalent material
Young Modulus	145 GPa	92 GPa	60.77 GPa
Poisson ration	0.2	0.17	0.1826
Density	3800 (kg/m^3)	2300 (kg/m^3)	2928.7 (kg/m^3)
Thermal expansion coeff.	9e-6 (/K)	3.8e-7 (/K)	4.9667e-6 (/K)

The utilized parameters for the model are presented in the Table 4.2. The data for each dielectric TiO_2 and SiO_2 were selected from [97, 98].

Subdomain and Boundary Settings
The aforementioned bulk equivalent materials that represented the multilayers of the mirrors, were used to define the structures in the subdomain. Subdomain settings define the physics on the main model, in our case the material properties and the initial stress were described. The suspension and membrane of the filter had the same physical thicknesses. The thickness of the structure was given as the meshed two-dimensional (2D)-structure, using triangular mesh elements, being extruded to three-dimensional (3D)-structure. For the Si_3N_4/SiO_2 DBRs, it was extruded from 0 to 1 μm then followed by 1 to 2 μm, hence, totally 2 μm of the thickness was obtained. The same quantity of initial stress, compressive and tensile, are applied on each 1 μm layer. No forces were applied, that is the load was equal to zero. The TiO_2/SiO_2 DBRs had a total thickness of 1 μm which was formed by two 500 nm layers, hence, the same initial stress was applied on each layer of 500 nm. The interface between the model structure and the neighborhood areas is specified by boundary conditions. Constraint in boundary setting was performed by choosing fixed boundaries located at the edge of the suspensions.

4.3.2 Simulation Results and Discussion

According to the measurement of the stress that resulted from the PECVD process [101], the total stress in the Si_3N_4/SiO_2 DBRs-based filter was approximately -70MPa in maximum. A range of stress between 0 up to -0.1 GPa was selected as the values in the solver parameters for this type of filter, where parametric analysis was used to solve the model.

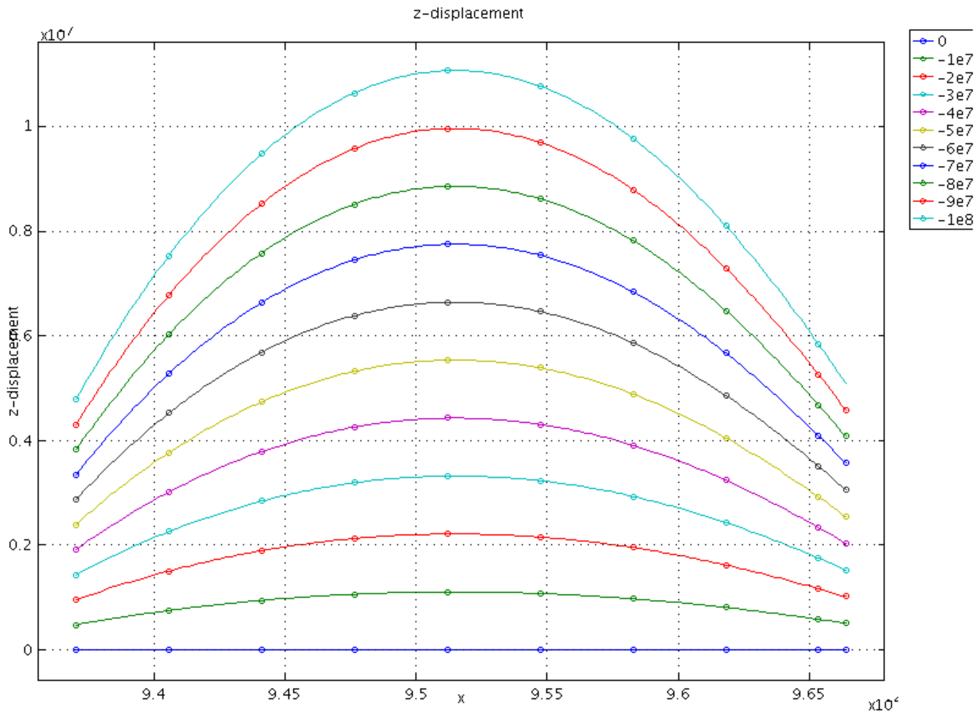

Figure 4.8: *The displacement at z-axis by applying the stress; the graph was depicted by cross-section post-processing step performed in FEMLAB. The x-axis represented the diameter of the filter membrane. The legend shows the increment of stress [Pa] induced in the Si_3N_4/SiO_2 layers.*

Figure 4.8 shows the stress led to a displacement at z-axis direction, viz. the filter membrane bent away, after removing of the sacrificial layer. The displacement profile showed strong deformation at the center and smaller deformation at the edges of the membrane. The picture was directly plotted using cross section post processing step, facilitated by FEMLAB, where the x-axis represented the membrane that is 30 μm in diameter. The result was taken from a filter structure with three curl-bent suspensions which had a displacement of 110 nm. The figure also shows that the increment of stress in the layers (legend) leads to higher displacement.

Simulation results regarding the filter with two suspensions are shown in Fig. 4.9. The straight suspension with width of 8 μm yielded larger membrane displacement than the one with the width of 10 μm. The graphs also showed that longer bent suspensions led to higher displacement for the filter with membrane diameters bigger than 40 μm. Hence, longer and narrower suspensions both led to larger displacements of the membranes. If the filters had curl-bent suspensions, they produced lower displacements compared to the ones with straight and bent suspensions. Membranes diameter influenced also the displacements, it is shown that 10 μm increasing in diameter led to displacement of approximately 75 up to 100 nm.

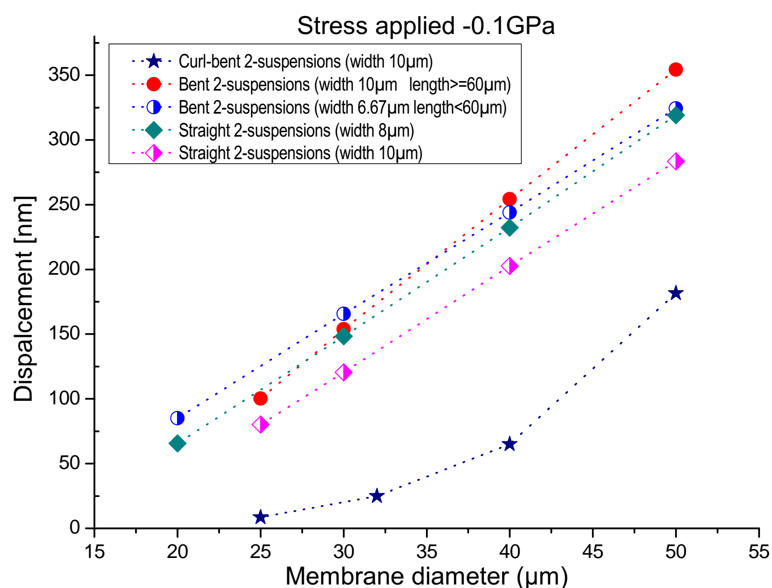

Figure 4.9: *Graph mirror displacement as a function of Si_3N_4/SiO_2 membrane diameter, with stress of 0.1 GPa, for the structures with two suspensions: straight, bent and curl-bent.*

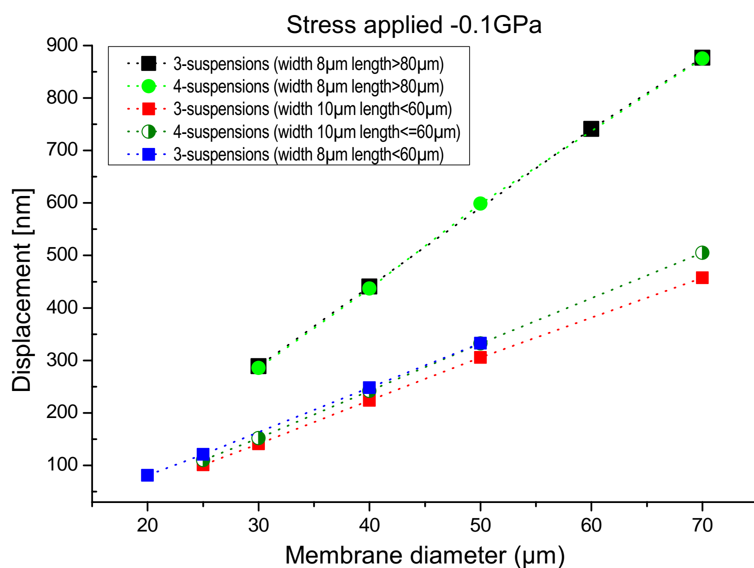

Figure 4.10: *Graph of mirror displacements as a function of Si_3N_4/SiO_2 membrane diameter with stress of -0.1 GPa, for the structures with three and four straight suspensions. The longer the suspensions or the bigger the membrane area, the membrane bends more.*

Figure 4.10 depicts the simulation results of the displacement of the membranes formed by Si_3N_4/SiO_2 layers, with three and four straight suspensions. For these filter types, each 10 μm increasing in membrane diameter led to approximately 150 nm in displacement height. These results showed that filter structures with three or four suspensions which had the same sizes, led to the same displacements. This graph also showed that the narrower suspension widths and the longer suspension lengths led to higher displacements of the membrane.

Displacement of the filter membrane with three bent and curl-bent suspensions are depicted in Fig. 4.11. It showed also that suspension length effected the displacement. The width of the suspensions had less effect to the displacement magnitude, however, shorter suspensions helped strongly to reduce membrane displacements. The graph in Fig. 4.11-bottom, shows the displacement profiles of the filter membranes with applied stress of -0.1 GPa, wherein the one with curl-bent type suspension exhibited less amount of displacement than the other with bent suspension. Both of the filter membranes had diameter of 30 μm.
Simulation on one pair of Si_3N_4/SiO_2-DBRs produced slightly higher displacements compared to the 9.5 pairs of the DBRs.

The profiles in Fig. 4.12 show the different amount of displacement of the membrane made of multilayers of TiO_2/SiO_2 with four straight and bent suspensions, under the same applied stress of -1 GPa. It also shows that the filter membrane with curl-bent suspensions led to less displacement than the one with straight suspensions. An image of post-processing simulation of a structure with four curl-bent suspensions is shown in Fig. 4.13. It exhibited a displacement of approximately 1.6 μm.

In Fig. 4.14, comparison of membrane displacement of two types of DBRs with applied stress of -1 GPa is shown. The filter structures with three and four straight suspensions were evaluated.
The figure shows that the displacement step of TiO_2/SiO_2 membranes with increasing diameter of 10 μm was 250 nm. For these TiO_2/SiO_2 DBRs, the filter with four suspensions had higher displacement than the one with three suspensions, and these differences in the displacement tended to increase as the size of the membrane were expanded. For instance, with a membrane diameter of 40 μm the filter with four suspensions bent 200 nm higher than the other with three suspensions. And with 70 μm of membrane diameter, the four suspensions had a displacement of nearly 350 nm higher than the three suspensions.
This phenomena was not found in the Si_3N_4/SiO_2 DBRs as -0.1 GPa of the stress was applied. However, as -1 GPa was utilized in the model, it was observed that they had slightly differences in the displacement. The four suspensions displaced orders of tens of nanometer higher than the three suspensions, with filter membrane diameter of 70 μm.

Conclusion
Using this model simulation several filter designs were evaluated regarding the behaviour of the membrane displacements. The simulations showed that the size of the filter mem-

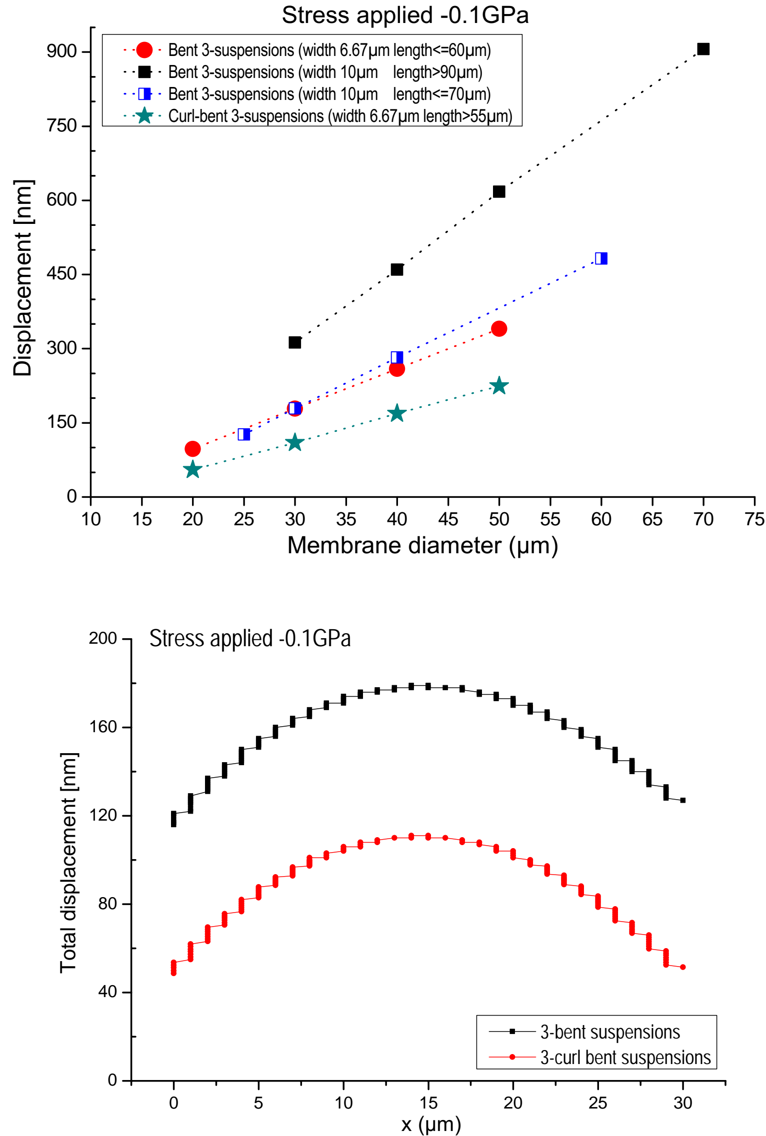

Figure 4.11: *Graph of mirror displacement as a function of membrane diameter, for the structures with three bent and curl-bent suspensions (top). Displacement profiles of the structures with three suspensions, where the x-axis represents the cross section of the membrane (bottom). The membranes are made of multilayers of Si_3N_4/SiO_2, and both have diameter of 30 µm. The filter with bent suspensions led to higher membrane displacement than the one with curl-bent suspensions.*

brane influenced the displacement magnitude. Moreover, the geometric shape and size of the suspensions are crucial, since their influences resulted in different membrane displacements.

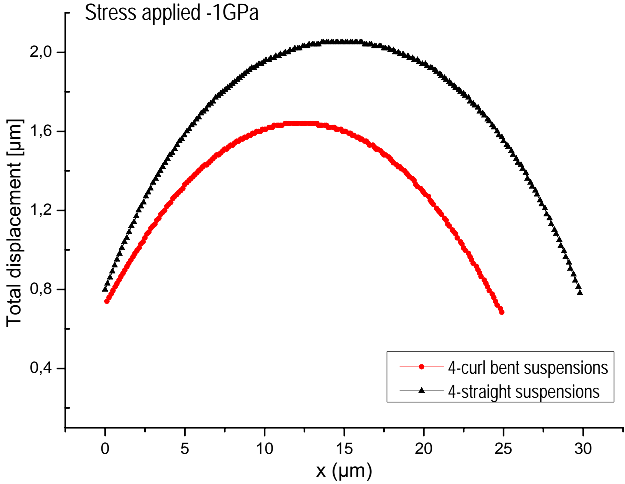

Figure 4.12: *Displacement profiles of the filter membranes, made of TiO_2/SiO_2, with four suspensions. The x-axis represents the cross section of the membrane. The type of suspensions differs the displacement magnitude; the filter (membrane d=30 µm) with straight suspensions bent more than the one (membrane d=25 µm) with curl-bent suspensions.*

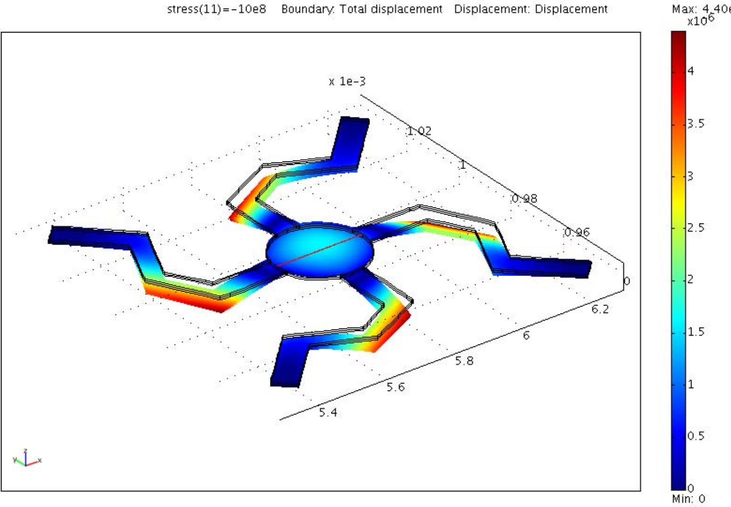

Figure 4.13: *Post-processing image of the structure with four curl-bent suspensions, the line shown on the membrane represents the cross section in x-axis plotted in Fig.* 4.12*, that is the membrane diameter.*

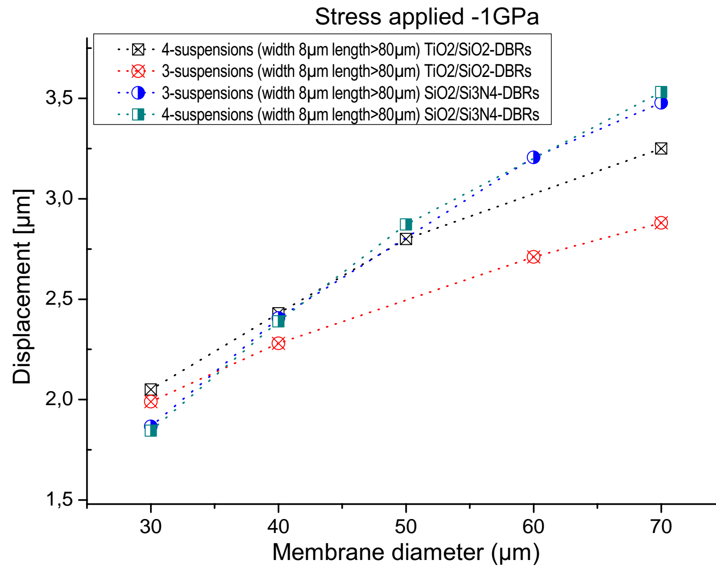

Figure 4.14: *Comparing the displacement of the mirrors (Si_3N_4/SiO_2 and TiO_2/SiO_2) as a function of membrane diameter. The applied stress of -1 GPa is given for the structures with three and four suspensions.*

Longer and narrower suspensions led to higher displacements of the membranes. Bigger membranes led to higher displacements than the smaller ones. At higher applied stress ($\geq$1GPa), the filter with three straight suspensions resulted in less displacements than the one with four straight suspensions. The differences in the displacements had tendency to increase as the size of membranes expanded. Curl-bent suspensions lead to the least displacements, compared to bent and straight suspensions.
Material properties of thin films depend strongly on the process conditions, and since approximation was made for the aforementioned dielectric mirrors, the selected data material has important influence on the simulation results. The results are compared to the fabricated structure, and it showed good agreements in terms of the geometric design that influences the membrane displacements. However, the differences in values of the displacements were detected, after comparing the displacements of membrane resulted from the experiments. This shortcoming cannot be avoided since the reference data, i.e materials system and thin films stress, that were used for the model, were varied from the one obtained from the fabrication process. The model considered that the membrane started to deform (displace) as the sacrificial layer is removed completely, however, in the fabrication step the removing of the sacrificial layer occured not instantaneously. This phenomenon also effected the results.

Chapter 5

Tunable Si_3N_4/SiO_2 DBRs-based Filters

DETAIL experimental fabrication processes for SiO_2/Si_3N_4 DBRs-based tunable filter, regarding lateral structuring of the top DBRs, spin coating of the cavity layer and underetching process to release the filter membrane are documented in this chapter. Two types of contact electrodes used in the fabrication will be reported as well. The filters were characterized by means of a microscope-spectrometer and a white-light interferometer to study their optical and mechanical properties, respectively. The results and discussion will conclude this chapter.

5.1 Lateral Structuring of the DBRs

The top DBRs, Si_3N_4/SiO_2, were structured in a reactive ion etcher, using photoresists and Al as etch masks. Optical lithography was applied for patterning the photoresist mask, and wet etching was performed for patterning Al mask. Details regarding the lithography steps are given in the appendices. In the following the etching process in the CCP- and the ICP-RIE are presented. The processes in the ICP defined into two part, the first one was the process which utilized both the ICP and the RF power. The second etching process in the ICP used only the RF power, this is called as *RIE-mode* process. The parameters used in the etch conditions were selected based on the references [7, 77] and adjusted to achieved the optimal results.

5.1.1 Etching Process in the Capacitively Coupling Plasma - RIE

This subsection presents the etching processes to structure the Si_3N_4/SiO_2 DBRs which were held in the CCP-RIE using AZ1518 photoresist mask. The processes are shown in tabular form (Table 5.1). At the beginning, the two dielectric films, Si_3N_4 and SiO_2, were etched. The etch condition was using 50 W RF power, with a pressure of 18.75 mTorr, and a mixture of $Ar/CHF_3/SF_6$ gas flow rate of 5.1/3/2 sccm at the temperature of 12.5°C. The etch rate of approximately 38 nm/min and 22 nm/min were obtained, for the Si_3N_4 and SiO_2 films, respectively. After that, the etching process of the Si_3N_4/SiO_2 DBRs was performed in the same condition. The etch rate and etch selectivity of the DBRs over the etch mask can be calculated with the relations given by Eq. 3.25c.

Table 5.1: Etch experiments for structuring of Si_3N_4, SiO_2, and the DBRs.

Material	Etch condition	Etch rate (nm/min)
SiO_2	$Ar/CHF_3/SF_6$	22
Si_3N_4	5.1/3/2 sccm	38
Si_3N_4/SiO_2	50W,18.75mTorr,12.5°C	≅32-35

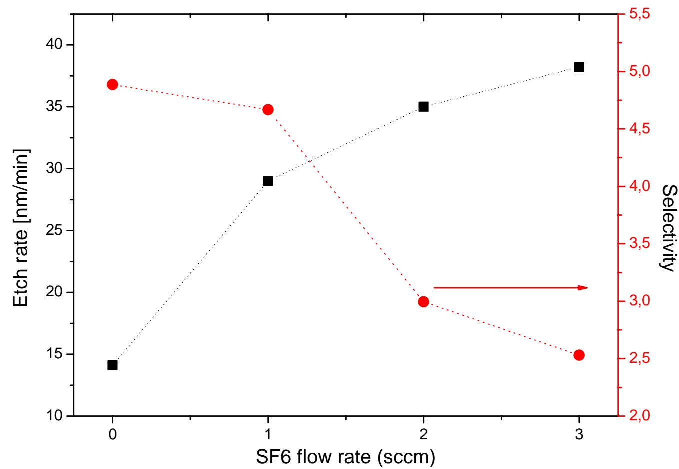

Figure 5.1: *Etch rates and selectivities of Si_3N_4/SiO_2 as a function of SF_6 flow rate (left). Etch experiments were performed in the CCP-RIE (redraw after [102]).*

Figure 5.1 shows the etch rates and selectivities as a function of the variation of SF_6 flow rate. By increasing the chemical component that is required for oxide etch mechanism, the etch rate increased and the selectivity decreased. The processes with different etch time were also performed, using a mixture of Ar/CHF_3 of 5.1/3 sccm and $Ar/CHF_3/SF_6$ of 5.1/3/2 sccm. The results in Fig. 5.2 show relatively stable etch rates. The selectivity decreased for the etch condition using the SF_6 gas, as the time increased (Fig. 5.2-inset). Hence, the presence of SF_6 gas had increased the etch rate of the photoresist mask. At SF_6 of 2 sccm, we observed that the selectivity depicted in Fig. 5.1 was around 3, meanwhile in Fig. 5.2-inset the seectivity was only 1.5. The reason that caused different etch selectivity can be described in the following. The samples used for the process in Fig. 5.1 have a size of one square inches (1 mm^2), and the samples used for the experiment with different etch time (Fig. 5.2) were smaller than those ones, i.e. approximately a quarter of to one-eight of one square inches. Since an increment of an etch rate can be obtained if the target area to be etched is decreased, it leads to higher etch rates in lateral direction if the target material has been etched completely, hence, higher etch rates of the photoresist mask resulted in less etch selectivities (Fig. 5.2).

Figure 5.3 shows SEM graphs of the excellent etch profile of 9.5 pairs of DBRs. Vertical slope angle of the sidewalls, and clean structure surface were observed.

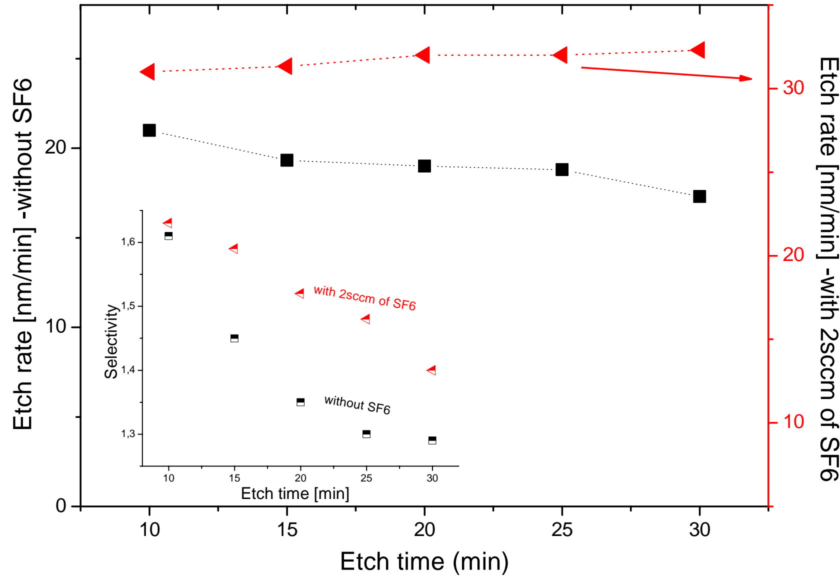

Figure 5.2: *Etch rates and selectivities of Si_3N_4/SiO_2 as a function of the etch time, with and without applying the SF_6 gas. Etch experiments were performed in the CCP-RIE.*

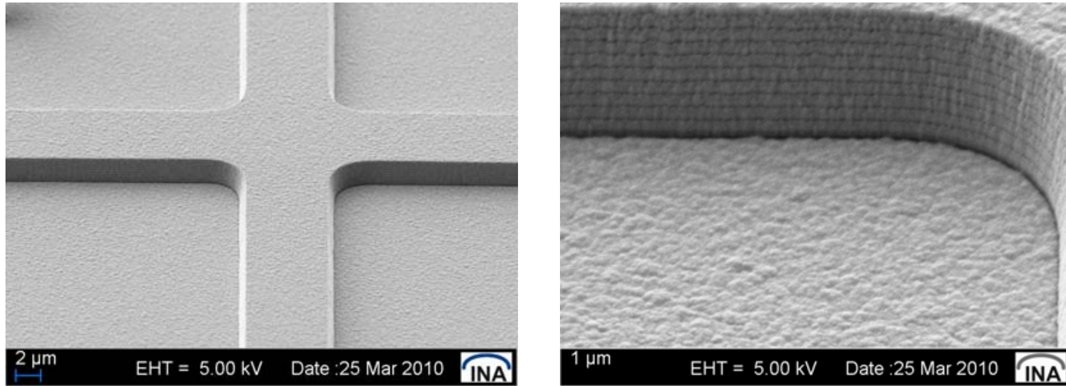

Figure 5.3: *SEM graphs show the etch profile of the 9.5 pairs top DBRs (approximately 1.85 μm in thickness) after lateral structuring in the CCP-RIE, the mask was removed (left), the close up of the structure sidewall (right). Etch condition: Ar/CHF_3/SF_6: 5.1/3/2 sccm, 50W of RF power, 18.75 mTorr at 12.5°C; etch time was 68 min.*

5.1.2 Etching Process in the Inductively Coupling Plasma- RIE

In this subsection, the results of the DBRs that were structured in the ICP-RIE using different etch conditions, with Al and AZ1518 photoresist mask are presented. The experiments are summarized in Table 5.2, they were performed with an expectation that

Table 5.2: Etching process in the ICP for structuring of the Si_3N_4/SiO_2 DBRs.

Etch mask	Etch condition	Etch rate (nm/min)
Al	SF_6/Ar:10/15 sccm,10mTorr,20°C 500W ICP/300W RF	80
	CHF_3/Ar/SF_6:10/40/5 sccm,10mTorr,20°C 750W ICP/175W RF	40
Photoresist	CHF_3/Ar/SF_6:10/40/5 sccm,10mTorr,20°C 100W ICP/175W RF	54

higher etch rates could be achieved by dry etching process in the ICP.

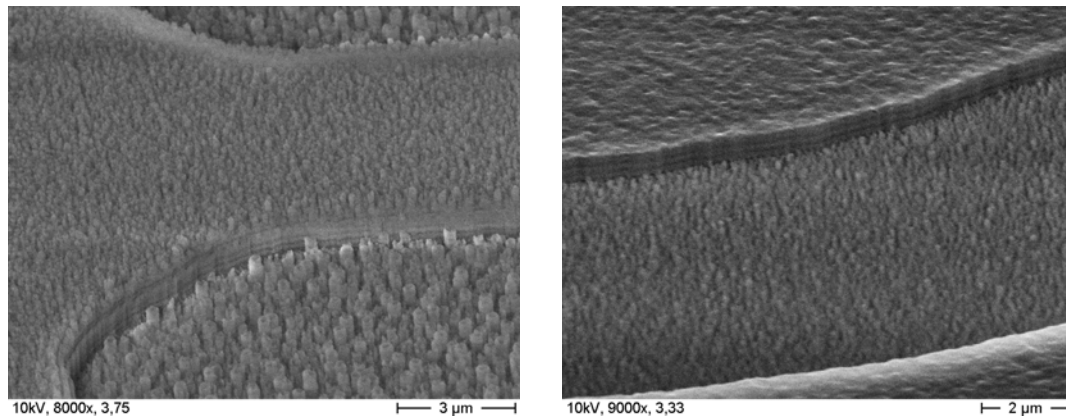

Figure 5.4: *SEM graphs of etch profile mirror, with Al mask. Etching without the CHF_3 flow rate, in an etch condition of SF_6/Ar=10/15 sccm, 500W ICP/300W RF, 10 mTorr and 20°C for 10 min. Al mask exhibited grassy surface (left). The structure result after process in an etch condition of CHF_3/Ar/SF_6=10/40/5 sccm, 750W ICP/175W RF power, 10 mTorr and 20°C for 10 min (right).*

The implementation of Al mask for dry etching of the DBRs are presented here. The first test using the etch condition of 500 W ICP/300 W RF and a mixed of SF_6/Ar flow rates of 10/15 sccm, at 10 mTorr and 20°C, with an etch time of 10 min. The results in Fig. 5.4-left show pits resulted on the structure surface and on the Al mask itself. These pits were possibly caused by high Ar flow rates or ion bombardment, while higher RF power actually can lead to good qualities of the sidewall and the surface. The depth structure of around 800 nm was measured, hence, a relatively high etch rate of approximately 80 nm/min was achieved. The second test was held in an etch condition of 750 W ICP/175 W RF power, mixed of CHF_3/Ar/SF_6=10/40/5 sccm, at a pressure of 10 mTorr and 20°C. The polymer formation contributed by CHF_3 reduced the etch rate. And for this test, higher ICP power (750 W) was utilized which also resulted in lower etch rate than the first result. The depth of 400 nm was obtained as the structure was etched for 10 min. An SEM graph with Al mask on the structure is shown in Fig. 5.4-right, the Al mask looked smooth, however the roughness of the mirror surface caused by the high ICP power, was

observed.

Etching of the DBRs using the photoresist mask was performed in an etch condition of 100 W ICP/175 W RF power, a mixture of CHF_3/Ar/SF_6 of 10/40/5 sccm, at 10 mTorr and 20°C. The etch rate of approximately 54 nm/min and selectivity of 1 were obtained. The micrograph in Fig. 5.5-left shows the structure after the etching process, with the photoresist mask was still on it. Removing of the mask can be performed directly in the ICP by using 10 sccm of O_2 at 2000 W ICP/200 W RF power, with a pressure of 6 mTorr and a temperature of 20°C. Another sample which was etched and subsequently its mask was removed in the ICP, is shown in Fig. 5.5-right. Removal of photoresist mask took 5 min. The surface profile was not completely clean, however, compared to Fig. 5.4 it showed smoother etched profile. In this process, oxygen helped to remove the residue and less coil power, of 100 W, led to less surface roughness.

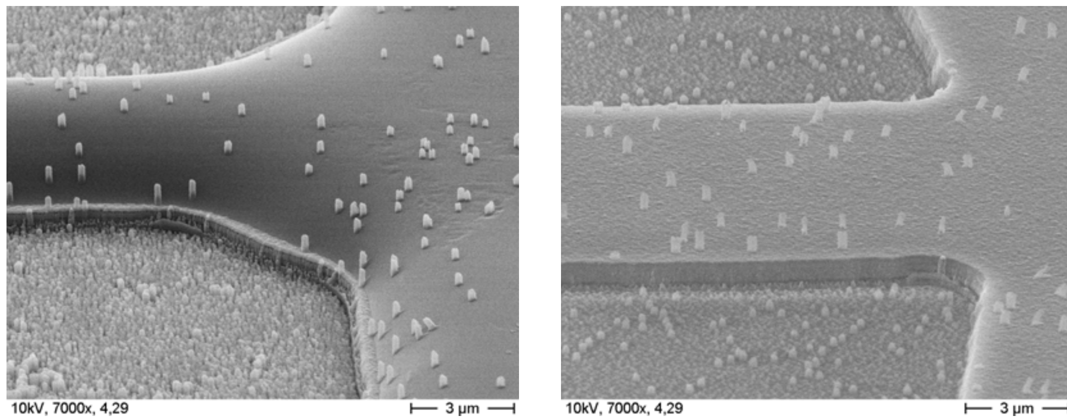

Figure 5.5: *SEM graphs of etch profile mirror, with the photoresist etch mask still on the mirror (left), after process with oxigen the photoresist was removed (right). Etch condition in the ICP: CHF_3/Ar/SF_6=10/40/5 sccm, 100W ICP/175W RF, 10 mTorr, 20°C, 10min.*

5.1.3 *RIE-mode* in the Inductively Coupling Plasma - RIE

This part presents an *RIE-mode* process in the ICP-RIE. The process utilized the RF power during the etching while the ICP power was set to zero. The purpose was to obtain higher etch rates by increasing the RF power and varying the process pressure, and to investigate the etch profile.
Two positive photoresist, AZ1518 and AZ1505, and a negative photoresist AZnLoF2070 diluted 5:1, were used as the etch masks in these experiments, at the condition of 250 W RF power, and temperature of 20°C. Etch behaviour at different process pressures under AZ1518 mask is depicted in Fig. 5.6, these results were obtained with Ar/CHF_3/SF_6 flow rates of 5.1/3/2 sccm. It was observed that at a low pressure, 6 mTorr, a relatively high etch rate of was obtained. Within low pressure, the collisions in plasma were relatively small, in that way, ions with high energy reached the target surface. The etch rates and

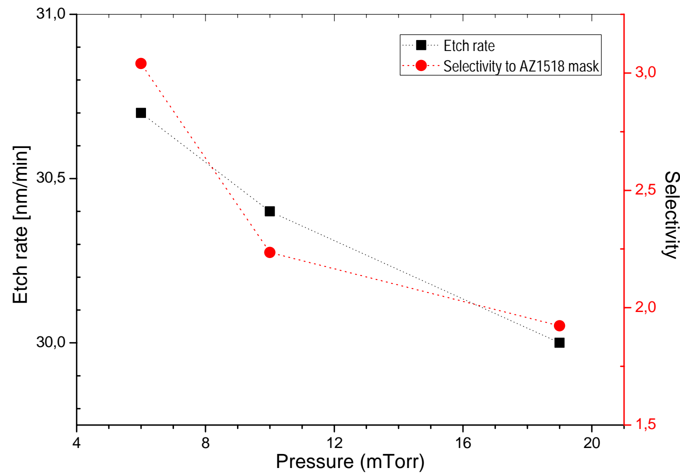

Figure 5.6: *Etch rates and selectivities as a function of the varied process pressure. Increasing the pressure decreased both etch rates and selectivities. Etch experiments were performed with AZ1518 photoresist masks in the ICP using RIE-mode.*

selectivities tended to decrease as the pressure increased. This high pressure condition led to higher particle densities, wherein many collisions happened and the ions had shorter free path, hence, the ion energies were low.
This phenomenon was also observed as SF_6 flow rate of 4 sccm in the etch experiments with AZnLoF2070 5:1 mask was performed, an etch rate of approximately 85 nm/min was achieved as shown in Fig. 5.7. However, a minor deviation was observed at 2sccm of SF_6, a slightly increment of the etch rate occured at pressure of 11 mTorr. This deviation might be happened due to the inhomogeinity of the film deposition of the sample used in the experiments.

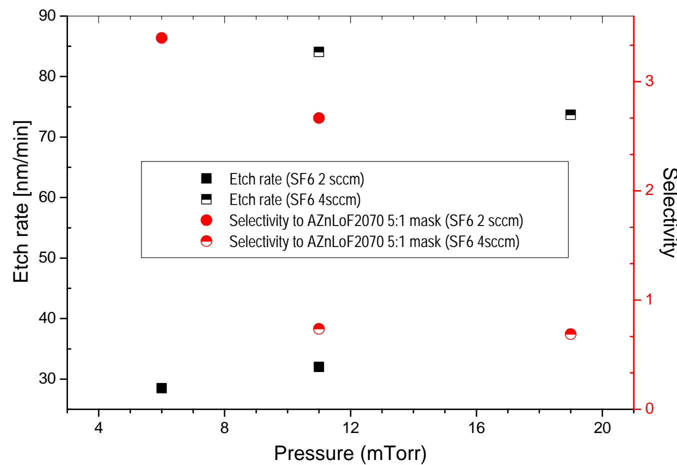

Figure 5.7: *Etch rates and selectivities as a function of process pressure. Increasing SF_6 flow rate increased the etch rates. Etch experiments were performed with AZnLoF2070 5:1 photoresist mask in the ICP using RIE-mode.*

A thin photoresist, the AZ1505 of approximately 500 nm in thickness, was also used as etch mask. An etch rate of approximately 40 nm/min and etch selectivity of 2:1 for the mirror over the mask were achieved. However, compared to etch profile under the AZ1518 mask, the result showed lower quality of the sidewall, i.e. polymerization or sidewall passivation and gradual sidewalls were observed, as shown in SEM graphs of the etch profile of the DBRs, after the *RIE-mode* etching process with AZ1518 and AZ1505 masks (Fig. 5.8). Removing photoresist etch masks after these processes can be easily performed using NMP (N-methyl-pyrollidone) based solvent that is heated on a hotplate at temperature of 70-80°C.

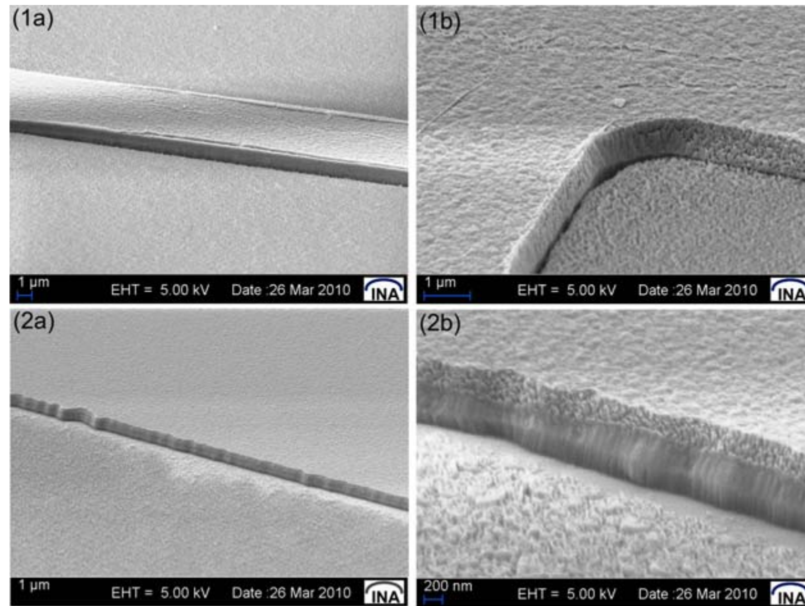

Figure 5.8: *SEM graphs of the etched mirrors. The AZ1518 mask was used (1a and 1b) in the process, resulted in an etch rate of 30 nm/min and selectivity of 1.9; the etch time was 25 min. The AZ1505 mask was used (2a and 2b) in the process, resulted in an etch rate of 40 nm/min and selectivity of 2; the etch time was 15 min. The etch condition was Ar/CHF_3/SF_6 of 5.1/3/2 sccm at 19 mTorr, 20°C, and 250 W of RF power.*

Table 5.3 summarized the processes performed for the structuring of the Si_3N_4/SiO_2 DBRs. AZ1518 photoresist was found to be a good candidate as the etch mask for the processes in the CCP- and ICP-RIE. Low power should be utilized in the ICP, 100 W ICP/175 W RF, to achieve relatively good qualities of the etched profiles. At 10 mTorr, 54 nm/min of etch rate was obtained, and removing of the photoresist mask was accomplished subsequently in the ICP using O_2 gas. A good etched profile was also observed as the process held in the *RIE mode*, where an etch rate of 30 nm/min was achieved at 19 mTorr with applied RF power of 250 W. However, compared to these results, a better quality of the etched structure profile was yielded from the process in the CCP (Fig. 5.3).

Table 5.3: Etch experiments for structuring of the Si_3N_4/SiO_2 DBRs.

Process	in the CCP-RIE	in the ICP-RIE	
Power	RF (50W)	ICP and RF	RF (250W *RIE-mode*)
Etch mask	AZ1518 photoresist	Al, AZ1518 photoresist	photoresists: AZ1518, AZnLoF2070,AZ1505
Etch rate	32 nm/min	40 - 54 nm/min	30 - 85 nm/min
Etch profile	++	+	+

+ expresses good qualities of the structure's sidewall and surface

5.2 UV-NIL Polymers as the Cavity Layers

In this work, three UV-NIL polymers, i.e. the mr-UVCur06, mr-UVCur21 and PAK-01, as the filters cavity layer materials were investigated. They worked as sacrificial layer and supporting post structures. The polymers were applied by spin coating process, with the speed correspondent to the required thickness. A half-wavelength cavity thickness required by the filter design was obtained by adjusting the rpm. In the first and the second subsection, the polymer's coating processes are described. And in the third subsection, the underetching process of these polymers will be presented.

5.2.1 mr-UVCur06 and mr-UVCur21 Polymers

The polymers are coated on the top of bottom DBRs, that is the Si_3N_4 layer which has hydrophilic surface. Applying adhesion promoter can improve the polymer adhesion. For this purpose, adhesion promoter mr-APS1 was used. Before applying the mr-APS1, the substrate was baked for 20 up to 30 min on a hotplate at 150°C for desorption of water. The mr-APS1 was spun at 5000 rpm for 60s and baked at 150°C for 30-40s. Subsequently, the polymer was coated and baked at 80°C for 1 min and exposed under UV light for 5 min in nitrogen ambient, to avoid oxygen that could prevent the crosslinking process of the polymer. These polymers withstood the process steps utilized in the filters fabrication, such as wet etching (in Al or ITO etchant solution) and soaking into a solvent (acetone or NMP).
Thicknesses of approximately 275 nm and 325 nm were delivered as the filter cavity layers with the reference wavelengths of 550 and 650 nm, respectively. Figure 5.9 shows transmission linewidths of the filters. Good adhesion of these polymers to the Si_3N_4/SiO_2 DBRs was achieved.

As mentioned in previous chapter, determination of polymer thickness was performed by an ellipsometer following a test coating of polymer on a Si wafer. An attempt to determine the thickness by using a white light interferometer (WLI) was performed, however, this method was not quite adequate for this purpose, since it was inefficient in time and materials. Before the measurement by the WLI took place, a reflective thin film (e.g. Al) was required to be deposited on the polymer and then structured. Subsequently, the polymer had to be underetched, to remove some parts which were not covered by Al film, after that

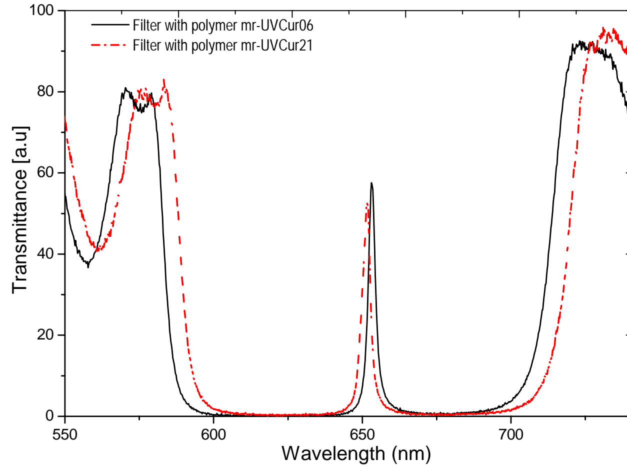

Figure 5.9: *Spectral transmission of the filters, with mr-UVCur06 and mr-UVCur21 as the cavity layers. Measurement were taken before underetching process.*

the WLI measurement could be applied. Hence, patterning of Al film and underetching of the polymer were necessary before the WLI measurement took place. Evidently, an effective way to determine the polymer thickness was by means of an ellipsometer, since it required only the coated polymer on a silicon substrate.

5.2.2 PAK-01 Polymer

As shown in Table 3.1, the PAK-01 has high viscosity, therefore, it was diluted to obtain the required thickness of the filter cavity. Diluting the PAK-01 into 20wt% up to 25wt% with ether (Ethylen-glycol-monomethylether, $C_3H_8O_2$ [1]) was performed to obtain polymer thicknesses between 300 nm up to 500 nm. The diluted solution was filtered before it was used in the spin coating process. This coating process used low spin speed at the beginning and ramping speed upwards to the final spin speed [66]. Hence, in these experiments, spin speed of 350 rpm (or 500 rpm) for 5s, then 1000 rpm for 5s, and finally the speed regarding to the required thickness for 20s, were applied. The ramp spin speed leads to homogeneous coating results. The polymer thicknesses as a function of the spin speed are depicted in Fig. 5.10. The curves were fitted to exponential model function, the data regarding the exponential model are given in the appendix.

An adhesion promoter to obtain a good adhesion between the polymer and the bottom DBRs is required. The adhesion promoter TI-Prime was finally selected after the investigation on other promoters and experiments using varied treatments. As an adhesion promoter TI-Prime can change the Si_3N_4 surface to hydrophobic. Hence the adhesion of the polymer can be improved. Experiments with the promoter mr-APS1 and TI-Prime, treatment without any promoter, and treatment using an oxygen plasma were applied on the samples before applying the polymer. Relatively homogeneous polymer surface was detected as the TI-Prime as the adhesion promoter was utilized. The comparison to the sample with the mr-APS1 is shown in Fig. 5.11. Unhomogeneous surface revealed by the

[1] its chemical and physical data are given in appendix

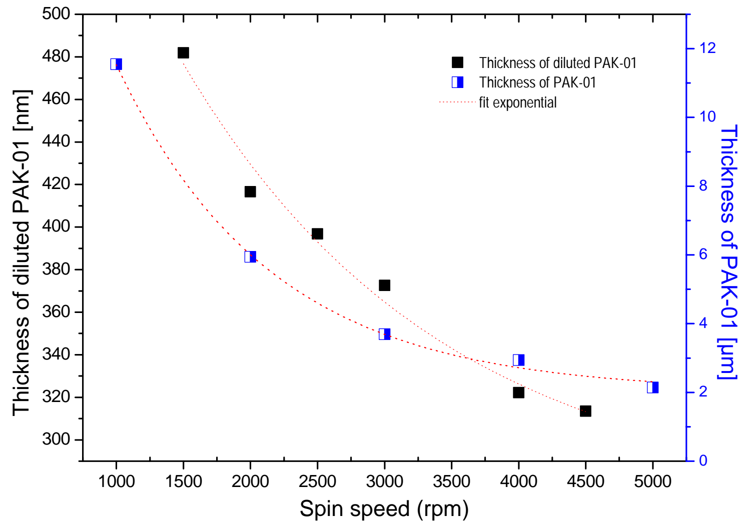

Figure 5.10: *Spin curve of PAK-01 polymers; represents undiluted PAK-01 [courtesy of Toyo-Gosei] and diluted PAK-01 (4:1 with ether). The measurement was taken after softbake and subsequent exposure. Higher spin speeds lead to thinner polymer layers.*

polymer that used the adhesion promoter mr-APS1 (Fig. 5.11-right).

Figure 5.11: *Coating process of PAK-01 polymer, the surface looked homogeneous with adhesion promoter TI-Prime (left), and with mr-APS1 (right) where the inhomogeneity of the surface showed different colors.*

After the deposition of the top Si_3N_4/SiO_2 DBRs on the polymer, the sample was observed under the optical microscope. The surface profile was quite homogeneous, and the spectral transmission measured by the microscope-spectrometer showed a sharp transmission peak. However, the filter linewidth was slightly shifted, as shown in Fig. 5.12, probably due to the thickness of the cavity layer was not exactly fit to a half-wavelength, or the

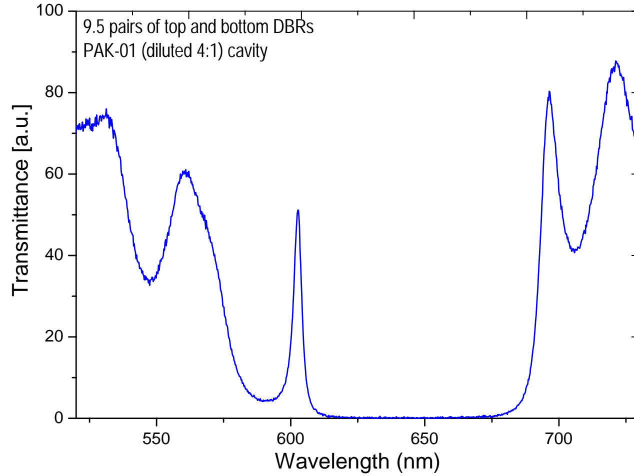

Figure 5.12: *Spectral transmission of the filter with 9.5 pairs of Si_3N_4/SiO_2 DBRs and PAK-01 diluted 4:1 as the cavity layer (spin speed at 3950 rpm).*

fabrication parameters of the mirrors and contamination in the chamber during deposition process caused the shifting in the center-wavelength (650 nm) of the filter.

5.2.3 Underetching Process in the Oxygen Plasma

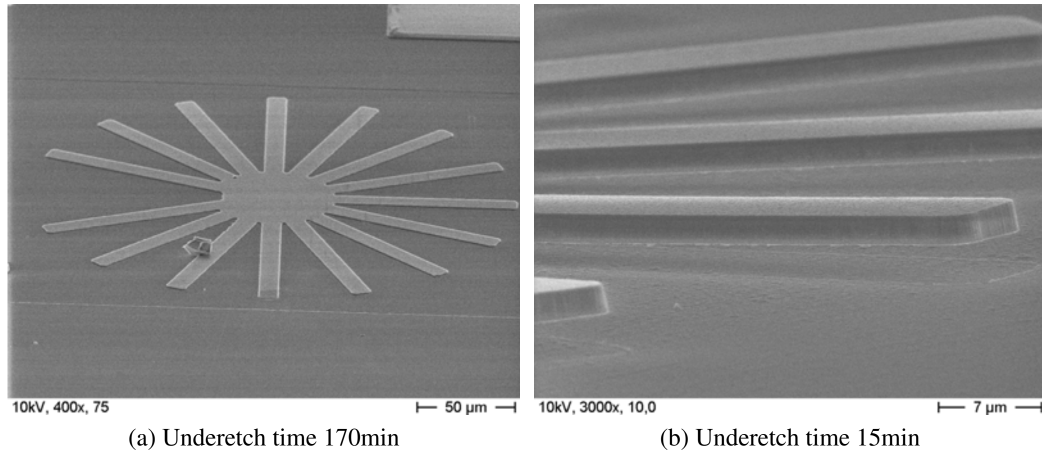

(a) Underetch time 170min (b) Underetch time 15min

Figure 5.13: *SEM micrographs of the star-structure for varied underetching time. (a) The polymer was treated without nitrogen during the exposure, the structure was not completely released for 170 min. (b) Nitrogen was applied during the UV-exposure, the structure was released in only 15 min underetching time.*

The underetching process concerns of removing of the polymer sacrificial layer underneath the filter membrane and suspensions. Nitrogen ambient is required for the polymers crosslinking process, then the crosslinked polymer can be removed in an oxygen plasma. This process was performed in a plasma asher Tepla 200-G at process pressure of 0.60 up to 0.70 mBarr and power of 250 W. The following SEM graphs (Fig. 5.13 show comparison of underetching time applied on the samples whose polymers were treated differently

during the exposure. In Fig. 5.13)-a, the exposure of the polymer was not performed in nitrogen ambient, and since there was no crosslinked-polymers obtained, the underetching process could not attack or removed the polymers. The sample in Fig. 5.13-b, where the released of cantilevers of a star structure were shown, was treated in nitrogen ambient during the UV exposure. Therefore, the crosslinked-polymers were established, and the underetching step in the oxygen plasma was able to remove it completely only in 15 min.

Cantilever structure as shown in Fig. 5.14 worked as an indicator element of underetching process. The structure consisted of different cantilever width (varied from 10 μm up to 60 μm) and the same length (310 μm and 100 μm). For instance, Fig. 5.14 shows that releasing 10 microns cantilever was completely done in 10 min underetching process, hence the estimated rate was 1 μm. Beside those cantilevers, an investigation on the star structure (Fig. 5.15) gives also an important information for determination of the underetch rate. After 10 min underetching process, the polymer underneath the star was removed 8 μm to 10 μm, and the rest of polymers underneath the suspensions were still left. And after 20 min underetching, an approximately 18 μm of the polymer was underetched. By investigating those structures the underetching process can be controlled, and the rate can be estimated. The time required for underetching of a structure depended not only on the structure size but also on the opening space or area nearby the structures, where the oxygen plasma could easily reach the polymer. These estimated results were compared to determine the average underetch rate of the polymer, hence, the underetch rate of mr-UVCur06, mr-UVCur21 and PAK-01 4:1 are approximately 1 μm, 850 nm and 900 nm, respectively.

The filter membrane shown in Fig. 5.16 was released by removing the mr-UVCur06 sacrificial layer in the oxygen plasma for 15 min. To avoid undercutting of the polymer post structures during the underetching process, a presence of the protection layer is necessary. However, experiments regarding the protection layers together with the optimization of the process, will not be discussed in this report.

5.3 Contact Electrodes

Two compositions of the electrodes for the filters were examined, and in this section they are presented. In the first design, transparent Indium-Tin-Oxide (ITO) thin films were selected as the bottom and top electrodes. The second design used the ITO layer as the bottom electrodes and aluminum (Al) layer as the top electrodes.

5.3.1 Indium-Tin-Oxide as the Bottom and Top Electrodes

ITO film is well known as transparent conducting oxides. The simulation results in Fig. 5.17 show different thicknesses of ITO film and its reflection. Regarding its conductivity and optical transparency, a compromise in the deposition process should be made. Thicker film leads to higher material's conductivity, however, its optical transparency decreases. In these experiments, borosilicate glass substrates coated with ITO films, were used as

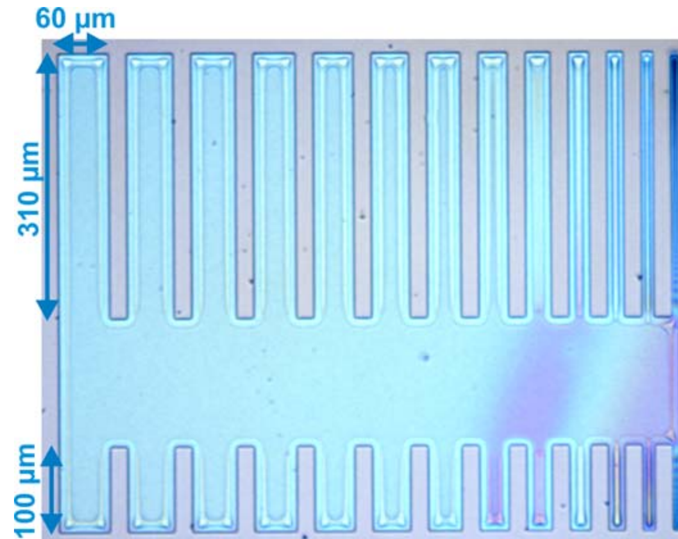

Figure 5.14: *An image (taken by Leica microscope) of the cantilever structure for estimating the underetch rate. The image shows the result after underetching of PAK-01 diluted 4:1 for 10 min, cantilever with width of 10 µm was completely released.*

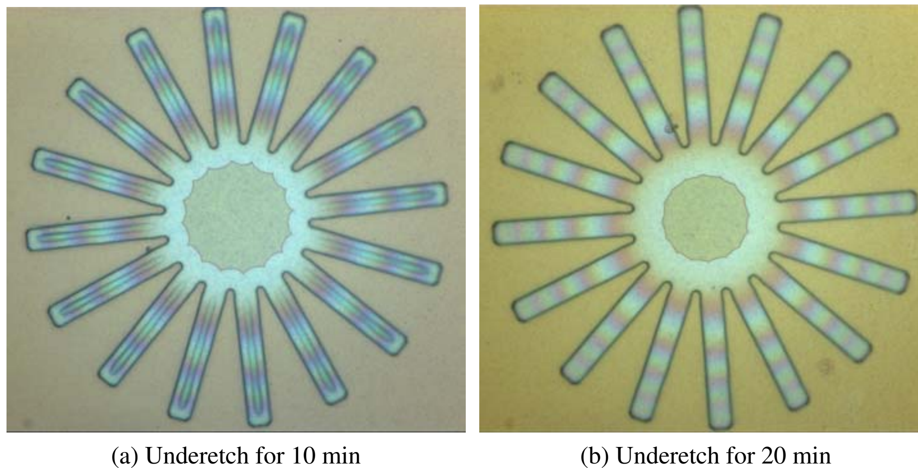

(a) Underetch for 10 min (b) Underetch for 20 min

Figure 5.15: *Images were taken by Leica microscope of the star structure (diameter 50 µm, the cantilever 65 µmx10 µm) was taken from two samples (9.5 pairs of top and bottom DBRs with PAK-01 4:1 as cavity), after underetching for 10 min (a), and underetching for 20 min (b).*

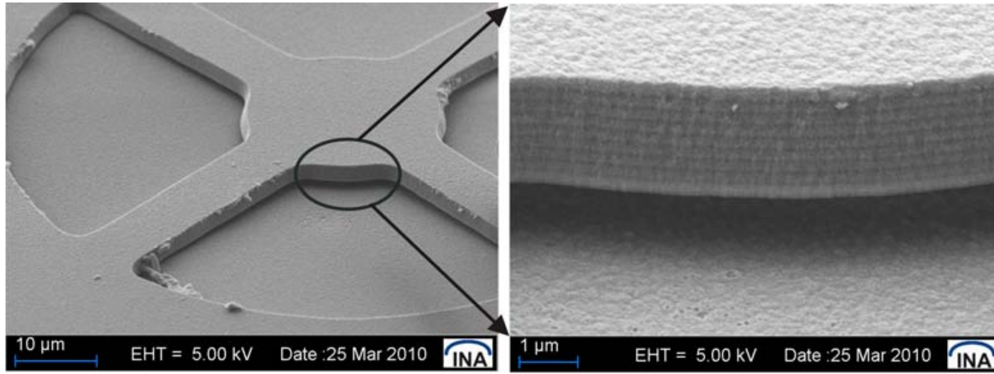

Figure 5.16: *SEM graphs of the filter membrane that was released after the underetch process for 15 min. The sample has ITO top electrodes which was deposited after the underetch process.*

the substrates for several tests for filters fabrication. The deposited ITO film on these substrates has 23 nm in thickness which represents 0.07λ (where λ= 650 nm). Since these ITO thicknesses unfit to a quarter-wavelength of the mirror layer design, some absorption emerged decreasing the spectral transmission peak. Therefore, a quarter-wavelength or $\lambda/4$ which is equal to approximately 83 nm of ITO film thickness was selected to fulfill the optical requirement, and the film was prepared by the IBSD. In addition, a rapid-thermal-annealing (RTA) process, to reduce ITO's sheet resistance, was performed after the sputtering step for the bottom electrodes.
The deposition of ITO as top electrodes was performed after the underetching process applied, hence, the top electrodes was deposited all over the samples. This might be the reason which caused a short-cut that could happen during the electrostatic actuation. One way to avoid that is by separating each block of the filter structures before the deposition of the top electrodes, or by structuring the top electrodes. Structuring of ITO top electrodes can only be obtained before the underetching process. However, the oxygen plasma that was required for the underetching process, led to an increment in ITO resistances. Hence, higher ITO resistances caused high applied voltages for the electrostatic actuation of the filters. Investigation on the sheet resistance of the ITO film was reported in [93], the resistance was raised to several MΩ due to the oxygen plasma process which was held for hours. The RTA that was used for ITO films reduced this effect, therefore, the resistance could be reduced. However, handling of ITO top electrodes in the RTA process might effect the polymer layers. Therefore, another conductive material, Al thin film, was investigated as the top electrodes.

5.3.2 Aluminum as the Top Electrode

The choice of Al films as top electrode is made in terms of its low cost and easy fabrication. The material films also withstand in the oxygen plasma process, compared to Cr film which can be etched away in the process. Deposition of Al film on the top DBRs was performed by the electron-beam evaporation. Evaporation was performed at pressure of

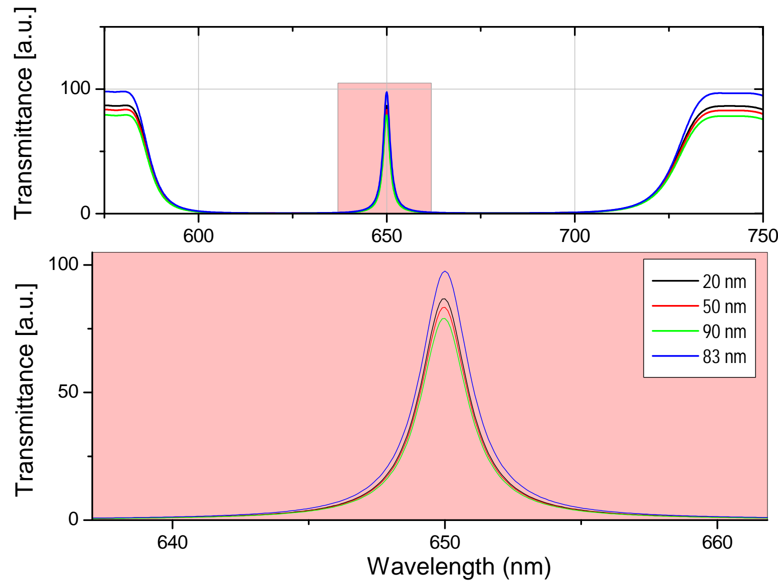

Figure 5.17: *Simulation OpenFilter on different thicknesses of ITO as electrodes for the filter, which uses Si_3N_4/SiO_2 DBRs and mr-UVCur06 cavity material. Thicker film of ITO reduced the optical tranparency. Film thickness of 20, 50 and 90 nm are simulated using ITO material data with refractive index* n = *1.88. Close-up image of filter linewidth is shown (bottom). 83 nm is an optimized thickness of ITO that fits to a quarter-wavelength, with refractive index of approximately 2.*

less than $10x10^{-6}$ mbar and a rate of 0.3 nm/s. A film thickness of 50 nm was chosen since at this thickness Al film has sufficiently high reflectivity (98%) and less stress in its layer. After the evaporation, a lithography process of AZ1518 photoresist to pattern the Al film was performed. Subsequently, the Al film was structured by wet etching process. The utilized structure design is set accordingly to the filter mesa design (i.e. membrane, suspensions and post structure), it means that the Al layer covers the filter structures, and only a small circle on each of the membrane center (as shown in Fig. 4.5 page35) is left uncovered. With this design, the optical properties of the filter still can be measured by focusing the light onto the circle.
Relatively lower actuation voltages were recorded for the tuning mechanism of the filter with Al top electrodes than the one with ITO top electrodes. These results are presented in the following section.

5.4 Results and Discussion

The filter transmission linewidths were observed by evaluating their optical properties under the microscope-spectrometer. Meanwhile, an investigation on their mechanical properties was performed by a WLI. In the following, the measurement results representing

the tunable filters properties are presented.
The measured filter as shown in Fig. 5.18, with ITO as the contact electrodes, has a 25 μm membrane diameter held by four suspensions with the width of 8 μm and length of 30 μm (Fig. 5.18-inset). The white square on the membrane center was the local active area which was illuminated and measured. However, the measured transmittance was only approximately 60%, this was possibly due to the absorption in ITO bottom electrode whose only 23 nm in thickness.
This tunable filter had 125 nm stopband and range of tuning wavelength was 75 nm by varying the voltage between 0 V and 30 V. The filter linewidth or the FWHM of less than 4 nm was observed.

The displacement of the top mirror as a function of the actuation voltage were investigated under the WLI, the results are shown in Fig. 5.19. Both of the measurement and analysis methods could be performed automatically using the WLI, to obtain the mechanical properties of the filters.

The measurement was performed on the filter with membrane diameter of 25 μm and three suspensions whose width of 8 μm (Fig. 5.19-left). A step width of 5 V was used and an applied voltage was given for every 33s. The membrane was attracted to both voltage polarities, negative and positive polarities. It revealed a tuning range of approximately 75 nm for the actuation voltages between 0 V - 30 V.
As can be seen from the simulation results (Chapter 4 page40) that by applying the same stress value, the filter membranes with three or four suspensions exhibited nearly the same deformation. Hence, this filter structure can be compared to the structure whose four suspensions, that was examined under the microscope-spectrometer. The filter observed by WLI has 3.5 pairs of DBRs which actually could deflect more than the filter observed by the microscope-spectrometer (whose 9.5 pairs of DBRs), however, it has smaller membrane area which in turn could compensate it.

The structure with membrane diameter of 10 μm and three suspensions (width of 6 μm) exhibited tuning range of approximately 50 nm, it was an expected result coming from the smaller membrane. The actuation curve is shown in Fig. 5.19-right. For this sample a step width of 2 V was used, and the voltage was applied for every 35s. However, a slight asymmetric curve, that is the membrane attracted more to negative polarity, was observed. And the displacement height of the filter at 0 V was changed after a reverse tuning. This was possibly due to charging effect in the dielectric film during the forward tuning actuation.

In the following, measurement results from the tunable filter arrays are presented. The filter arrays as shown in Fig. 5.20-inset, which have ITO as the bottom electrode and Al as the top electrode, revealed a tuning range of approximately 70 nm by varying voltage between 0 V up to 13 V. Figure 5.20-inset shows three filters *a*, *b* and *c*, with the membrane diameter of 30 μm and suspensions width of 10 μm. An array consist of three filters can be actuated simultaneously, however, the investigation of the transmission linewidth can only be performed for one filter at a time. The residual stress due to the actuation on the first membrane (filter-*a*) affected the displacement or deflection of the second one (filter-*b*) and also the third one (filter-*c*). This probably the reason why each of the filter

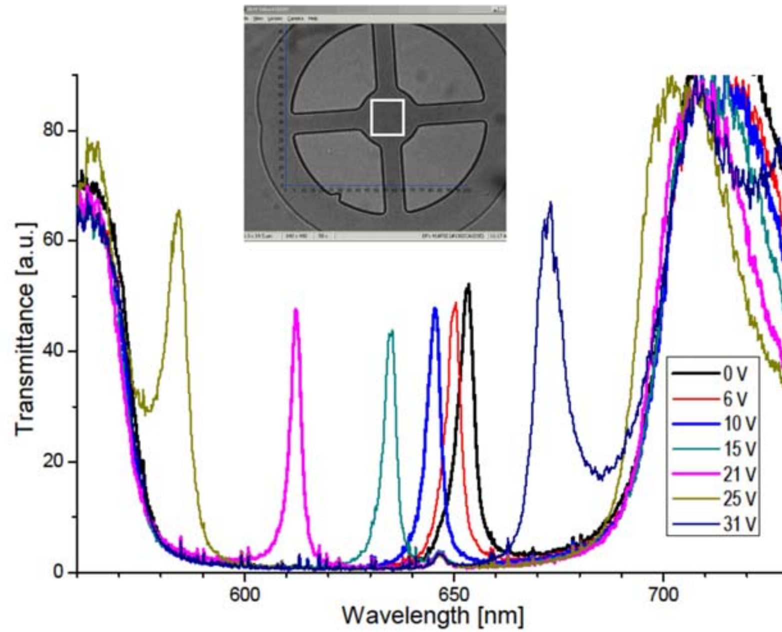

Figure 5.18: *Spectral transmission of one filter element, during the electrostatic actuation. Filter tuning range was approximately 75 nm, with FWHM of less than 4 nm.*

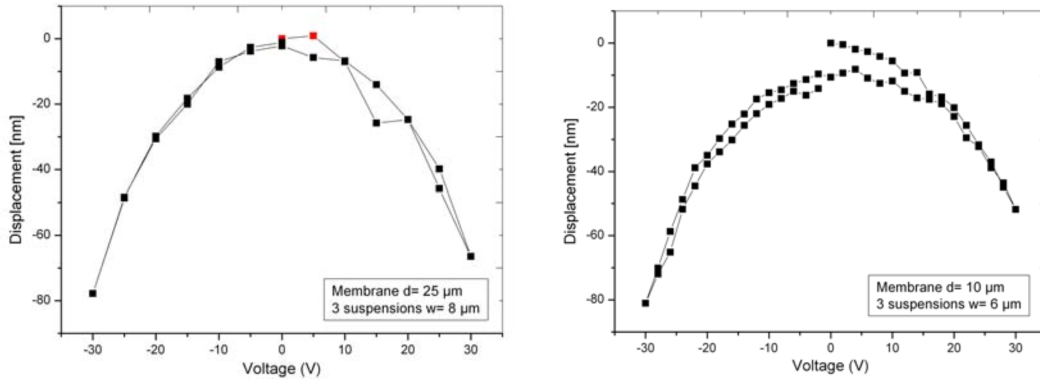

Figure 5.19: *Mechanical properties of the filters: membrane displacement as a function of tuning voltage (redraw after [93]). Measurements were taken for the membrane with diameter of 25 μm (left), and membrane with diameter of 10 μm (right).*

membrane had a different initial position at 0 V.
The spectral transmission of the filter-*a* is shown in Fig. 5.21. The measured filter linewidth is approximately 8 nm. The spectra revealed by the filter-*b* and filter-*c* were quite the same as the filter-*a*, as swhon in Fig. 5.22. However, the transmission peak at 0 V experienced a blue-shift due to the electrostatic charge in the materials. A borosilicate glass with ITO film as bottom electrodes was used as the substrate for this sample,

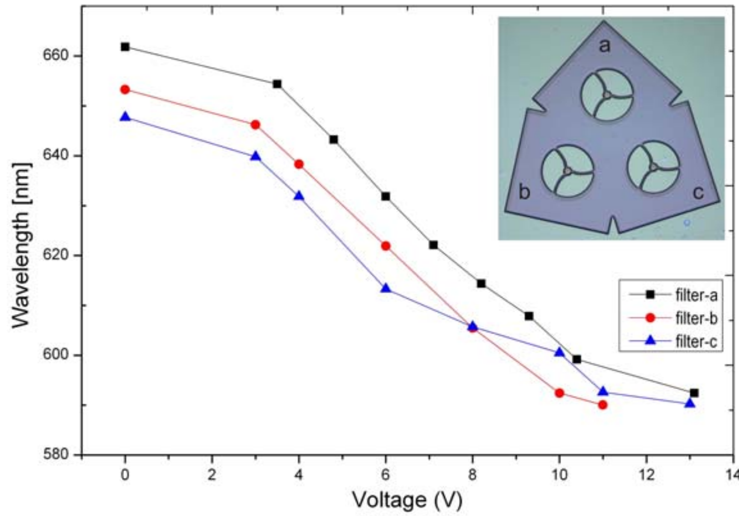

Figure 5.20: *The tuning spectral range of the filter arrays, consisted of three filters a, b and c. The filter structure is shown in (inset).*

wherein the ITO film thickness was equal to 0.07λ. And it had no RTA treatment as compared to the sample shown in Fig. 5.18. Hence, less transmission peak was obtained due to the absorption in the ITO film. It might also depend on the deposited dieletric layers since only a fair control on the deposition process could be attained, hence, their optical properties might lead to a shift in wavelength or reduce the transmission peak.

Another sample of filter array structures was characterized, and the results are given in the following. The sample has the ITO bottom electrode of 83 nm in thickness, which was treated in RTA before the deposition of the DBRs. After the structuring of the top DBRs, that is before the underetching took place, the filter linewidth was measured, and it is shown in Fig. 5.23. The filter showed approximately 70% of transmittance with a FWHM of 4 nm.

After the filter membrane was released, the actuation was performed. Spectral transmission as a function of tuning voltage of one of the filter was depicted in Fig. 5.24. Relatively higher peak transmission was observed, compared to the filter in Fig. 5.21. Tuning range of approximately 55 nm for the actuation between 0 V to 22 V was achieved. However, the filter linewidth was getting broader as it shifted to shorter wavelengths range, FWHM of approximately 4 nm shifted to 7 nm. In addition to that, the other two filters, which were in arrays, revealed two linewidths instead of only one transmission peak. These altered spectra might be resulted from unsimultaneously measurement that was performed under the microscope-spectrometer, hence, electrostatic charge which was experienced by one filter in arrays might be higher than the others.

The mechanical properties of these arrays were recorded as shown in the following (Fig. 5.25). The different heights were observed as the forward and reverse tuning being applied. Half-parabolic curves in this figure show that the filters worked in stable operation

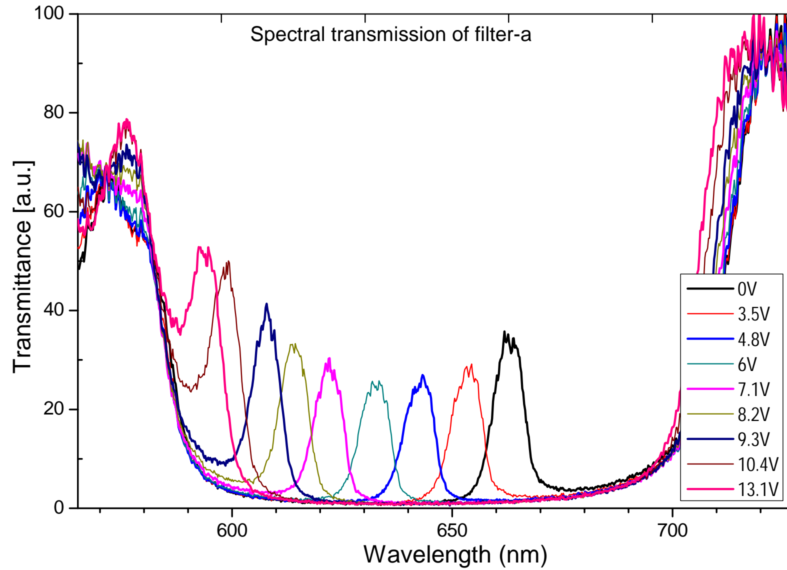

Figure 5.21: *Spectral transmission of one of the filter array during the electrostatic actuation. The tuning range was approximately 70 nm.*

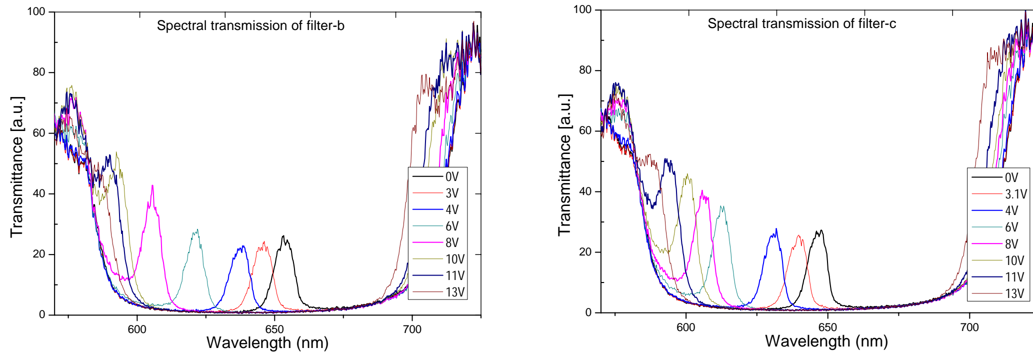

Figure 5.22: *Spectral transmission of the filter*-b *and filter*-c *in one array structure (the structure in Fig.*5.20*-inset) during the electrostatic actuation. The transmission peak at 0 V was shifted due to the electrostatic charge.*

range [43, 103]. The filter arrays revealed 100 up to 120 nm displacement during the actuation. The measured filters have four curl-bent suspension, their geometric structures and the hysteresis curve of the first-step actuation data are shown in Fig. 5.25-bottom.

Comparing these results to the measured displacement of the filters with bent suspensions, as shown in Fig. 5.20-inset (page62). Those filters exhibited larger displacement as the measurement took place several weeks after the fabrication. The displacement was approximately 300 nm within actuation voltage of 0 V to 80 V. Those filters with curl-bent

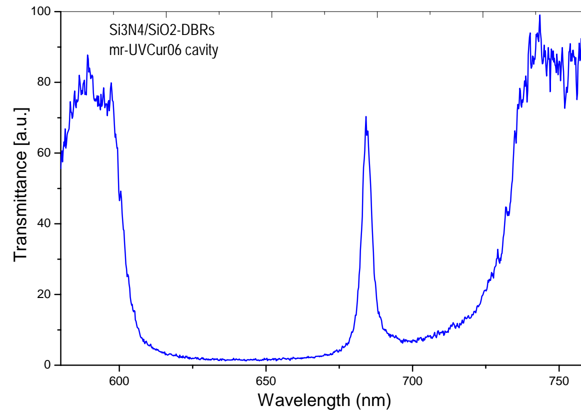

Figure 5.23: *Filter linewidth of a sample (9.5 pairs of DBRs and mr-UVCur06 cavity) after lateral structuring of the top DBRs, before the underetching process.*

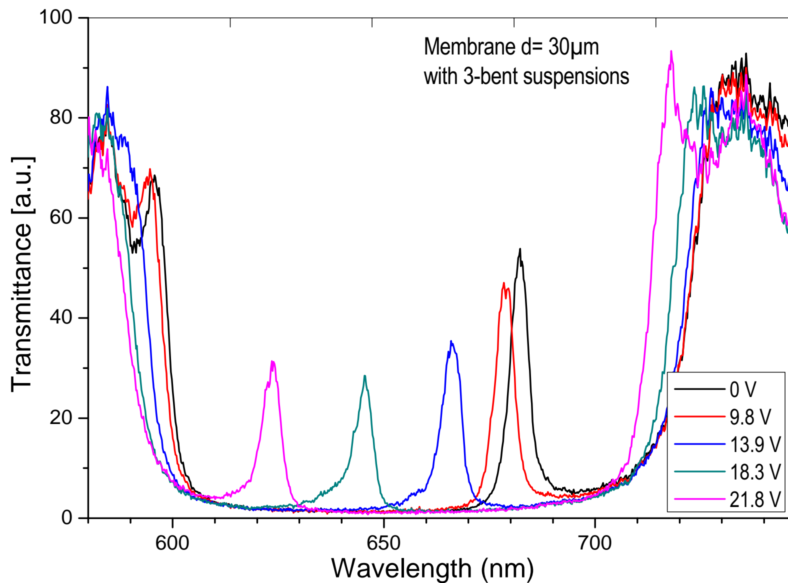

Figure 5.24: *Spectral transmission of one of the filter arrays as a function of actuation voltage, with tuning range of approximately 55 nm for the actuation between 0 V to 22 V. The membrane had a diameter of 30 µm and three bent suspensions with width of 10 µm.*

suspensions displaced less than those with the bent suspensions.

Conclusion

The Si_3N_4/SiO_2 DBRs-based tunable filter arrays with the aforementioned layer design have been successfully fabricated. The DBRs were fabricated by means of a PECVD method as a low cost deposition technology. The filter sacrificial layer, which later was removed to obtain an air gap cavity, was made of the UV-NIL polymers. Excellent etch profiles, i.e. steep sidewalls and smooth surface, of the mirror structures can be obtained in the CCP-RIE using AZ1518 photoresist as the etch mask, in the etch condition of

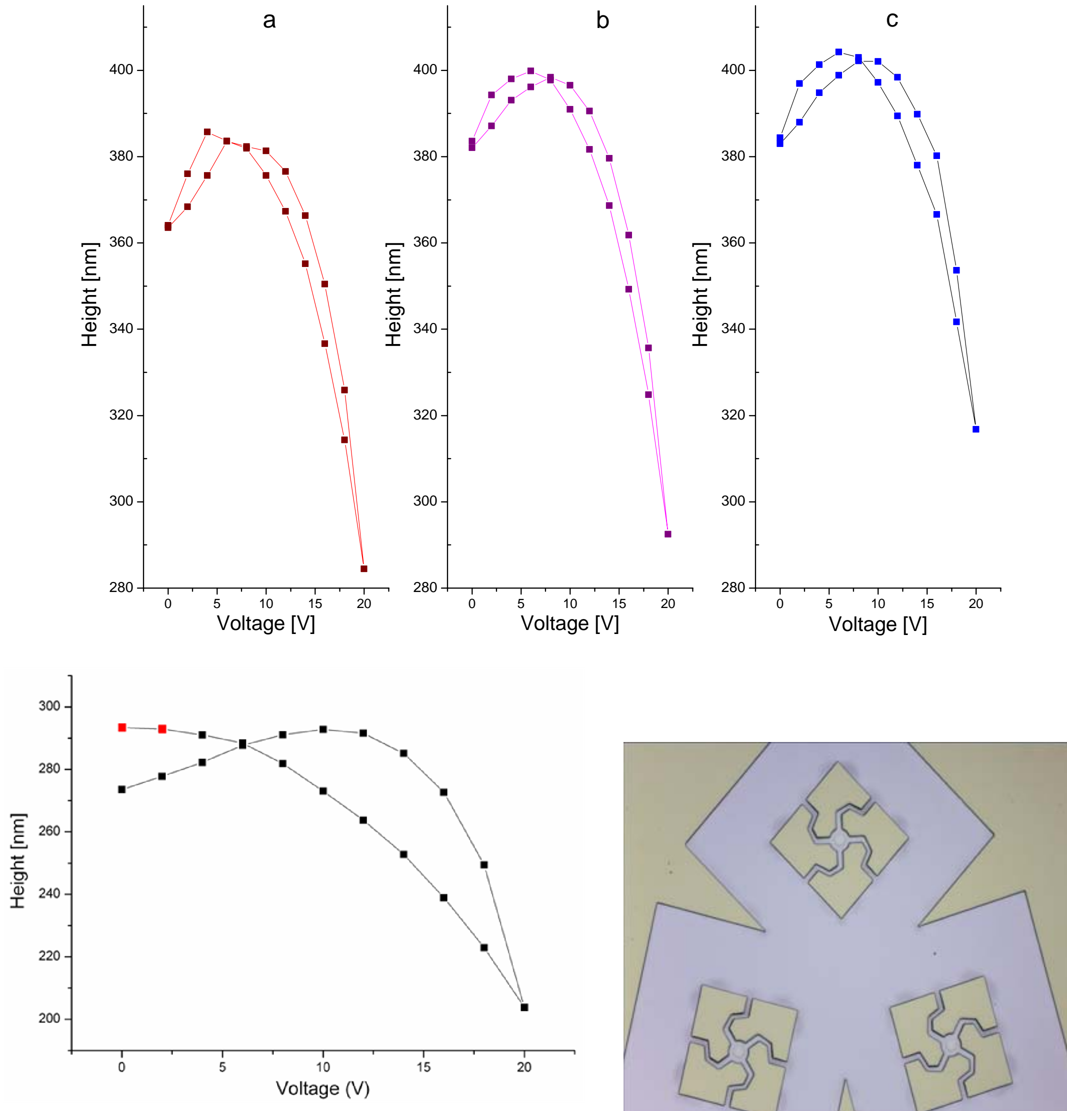

Figure 5.25: *Mechanical properties of the filter arrays: Membrane displacement of approximately 120 nm was observed for the actuation voltage between 0 V to 20 V, where the third-step measured data was captured (top), the first-step measured data showed a hysteresis curve and the filter geometry that was characterized (bottom). The measurement was performed using the WLI [measured by M. Mondragon-Marquez], and analyzing the displacement of filters could be accomplished simultaneously .*

$Ar/CHF_3/SF_6$: 5.1/3/2 sccm, 50 W of RF power, with a process pressure of 18.75 mTorr at 12.5°C. An etch rate of approximately 30 nm/min was achieved from this etching process. The ICP-RIE can also be used as an alternatif for structuring of the mirrors to save the process time, since the obtained etch rate was relatively higher, 54 nm/min, with a photoresist mask. However, the etch profile resulted from the CCP process shows better quality than the one resulted from the ICP.
Compatibility of the acrylate based polymers, the mr-UVCur06, mr-UVCur21 and PAK-01, to these dielectric mirrors and to the whole filter fabrication process had been examined as well. The homogeneity of the polymer after spin coating process determines the parallel plane of the two DBRs.
Optimization on the ITO bottom electrodes was required to match the DBRs layer design, and its treatment in the RTA would also help to improve the filter transmission peak. Mechanical properties of the filters measured by a WLI showed that the displacement of the membrane also depends on the filter geometric structures. The structure with the curl-bent suspensions exhibited less displacement than the one with bent or straight suspensions.
Due to the residual stress, the tilting of the filter membrane may lead to the change in filters transmission linewidths. To prevent this effect, a new design in structuring of the filter has been proposed, for instance, thinning of the suspensions to reduce the actuation voltage and to select the filter geometric structure that brings out less membrane displacements. These information will take into consideration for the new filter arrays design.

Chapter 6

TiO_2/SiO_2 DBRs-based Filters

EXPERIMENTS regarding the fabrication of the TiO_2/SiO_2 DBRs-based filters will be presented in this chapter, focusing on the characterization of dry etching process for the lateral structuring of the DBRs in the ICP- and CCP-RIE. The process concerning the UV-NIL polymers as sacrificial layers and the characterization of the filter properties will be described as well.

6.1 Lateral Structuring of the DBRs

For the etching experiments in this work, the TiO_2/SiO_2 DBRs with varied number of pairs were prepared. They were deposited using the IBSD method on a silicon wafer and glass substrates. The deposition on the Si- substrate was required to enable a reference measurement by the ellipsometry, for determination of the optical properties of each dielectric film. The data can be used in the model simulation by OpenFilter. The film deposition on the glass substrates was intended for the implementation of the filters.
The following subsections describe the etching process with hard etch masks in the ICP-RIE, and the processes with photoresist masks which were performed in the CCP- and also in the ICP-RIE. The utilized parameters for the process were selected from [70, 77, 104–107] and optimized to achieve excellent etched profiles.

6.1.1 Etch process in the ICP-RIE: using hard etch masks

At the beginning, an investigation on the etch behaviours of the DBRs in the ICP-RIE was performed through three attempts mentioned in the following.

(1) *Gas chopping-1*. The gas chopping technique was reported in detail by Volland including its model simulation for silicon in [81]. This technique comprises of repeated steps of etching, polymerization and sputtering, which leads to the structures with high aspect ratios. In this work, the etching step, the polymerization and the sputtering (for removing of the polymer) were accomplished using SF_6, C_4F_8, and O_2/Ar gases, respectively.

(2) *Gas chopping-2*. Within the second technique, the etching and sputtering steps were performed by using SF_6/Ar gases, and the polymerization by C_4F_8 gas.

(3) *Etching*. The third technique encountered only an etching step using SF_6 and Ar gases.

Better qualities of the structure sidewalls and surfaces, i.e. less sidewall passivation and smooth surfaces observed under an SEM, were obtained from the experiment wherein the third technique was utilized. Therefore, the following experiments were examined using only the combinations of SF_6/Ar gas flow rates, by varying the process pressure, power and temperature. In this part, three hard etch masks, i.e Al, Cr and ITO that were used in the experiments are presented.

6.1.1.1 Aluminum and Chrome etch masks

The Al and Cr films were evaporated on the top mirrors by electron-beam evaporation method. The thickness of 150 nm of each film was prepared. They were patterned as etch masks by wet etching and/or a lift-off process after the optical lithography step.

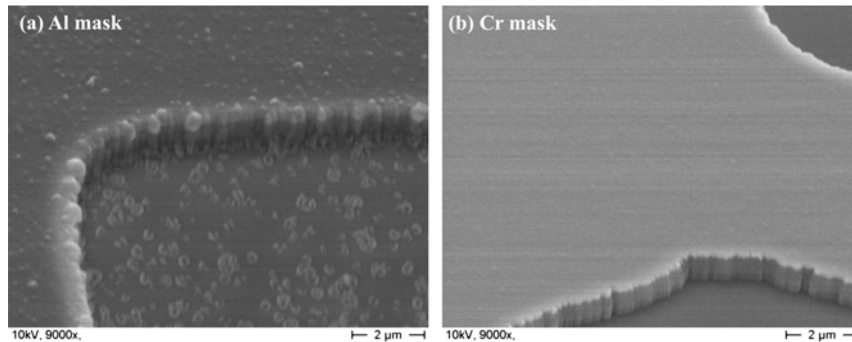

Figure 6.1: *SEM graphs show the mirror after the etching process, using Al mask (left), and Cr mask (right).*

The process in the ICP was executed for 15 min in a mixture of Ar/SF_6 gas flow rate:15/10 sccm, using 150 W RF/1500 W ICP power, at temperature of 20°C and a pressure of 10 mTorr. An etch rate of approximately 47 nm/min was obtained. At the same condition the results after the process using different masks are compared, as shown in Fig. 6.1. Plasma-induced damage or pits were observed for the structure using Al mask, meanwhile the structure using Cr mask showed a smoother surface. An etch selectivity of approximately 30 was calculated for the mirror over the Cr mask. However, lower quality of the sidewalls were still observed. This appearance was possibly caused by a high ICP power which induced the roughness. Adding more chemical components and controlling the applied power would be useful to obtain an excellent etched profile and relatively higher etch rates. For the next etching experiments using ITO etch mask, this information was taken

Table 6.1: Etch experiments for structuring of the TiO_2/SiO_2 DBRs in ICP-RIE: variation of gas flow rate.

Etch condition: 10mTorr,20°C,500W ICP/300W RF		Etch rate
Ar 20sccm	SF_6 varied	increased as SF_6 increased
SF_6 10sccm	Ar varied	decreased as Ar increased

into account. Optimization of the etching process using Cr mask will not be covered in this work.

6.1.1.2 Indium-Tin-Oxide etch mask

The Indium-Tin-Oxide (ITO) film of 92 nm in thickness was sputtered by the IBSD on the top mirrors. Patterning of the photoresist mask to structure the ITO was performed through the lithography, and subsequently the ITO film was etched in a mixed of HCl:water (1:1) etchant solution. Etch time of 20s - 30s was required for patterning 92 nm of ITO film.

The etching experiments of the DBRs using the ITO mask were performed in different etch conditions. In Table 6.1 the experiments regarding variation of gas flow rates are given. Figure 6.2 and 6.3 show the etch rates and selectivities with the variaton of SF_6, and Ar flow rates, respectively.

The SF_6 gas flow rates were varied, whereas Ar gas was set fixed at 20 sccm (Fig. 6.2), in the etch condition of 500 W ICP/300 W RF power, with the temperature of 20°C and a pressure of 10 mTorr. High content of the SF_6 gas influenced the sidewalls quality, as shown in Fig. 6.4-a with 10 sccm, and Fig. 6.4-b with 20 sccm. However, increasing of the SF_6 flow rate led to higher etch rates, of approximately 100 nm/min, due to the presence of higher chemical components in the etching process. Hence, reducing the bombardment of Ar ions increased the etch selectivity. The polymerization shown at the stucture sidewalls can be reduce by applying lower process pressure, this phenomenon can be seen as the variation of pressure was applied in the process (page75).

The influence of Ar flow rate was investigated by setting the flow of SF_6 at 10 sccm, the experimental results are shown in Fig. 6.3. As the Ar gas flow rate increased, fluorinated chemical components required for oxides etch mechanism would be reduced, hence, the etch rates and etch selectivities decreased. Fig. 6.4-a and 6.4-c, show SEM graphs as 20 sccm and 10 sccm of Ar were used, respectively. Higher Ar flow rate gave insignificant effect to the sidewall profile, however the mixture of 10/10 sccm of Ar/SF_6 exhibited smoother sidewall profiles, compared to the result shown in Fig. 6.4-b where 20/20 sccm of Ar/SF_6 was used.

Next experiments used variation of RF and ICP power in the etching process, as shown in Table 6.2. Figure 6.6 and 6.7 show the etch rates and selectivities as a function of the applied power. The increment in RF power increased the ion energy, and in turn, increased the etch rate and decreased the etch selectivity (Fig. 6.6). At relatively lower RF power (approximately $\leq$150 W), grassy sidewalls were observed as shown in Fig. 6.5-a, com-

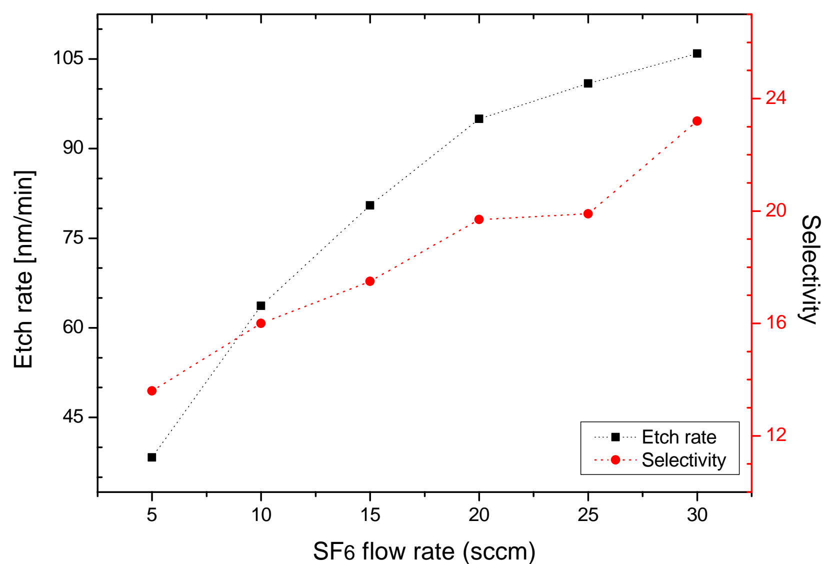

Figure 6.2: *Etch rates and selectivities as a function of varied SF_6, at fixed 20 sccm of Ar gas. ITO etch masks were used. Circles represent the selectivity, rectangles represent the etch rate.*

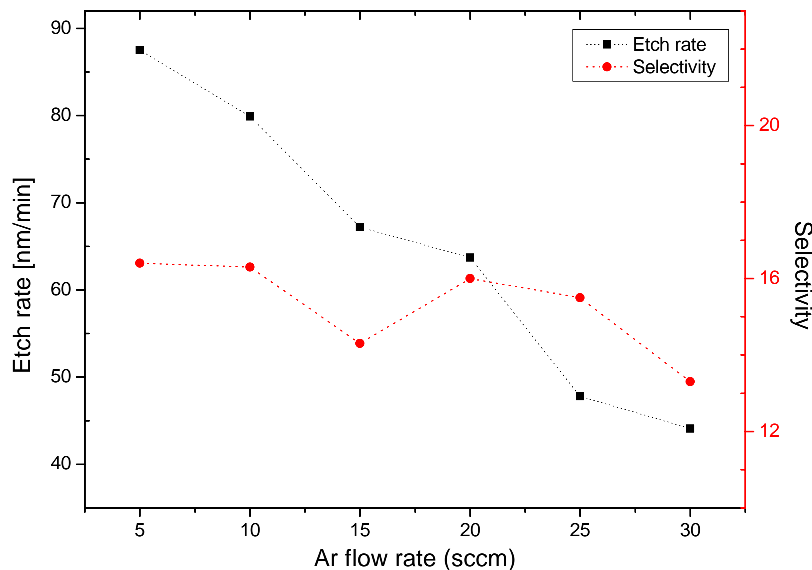

Figure 6.3: *Etch rates and selectivities as a function of varied Ar, at fixed 10 sccm of SF_6 gas. ITO etch masks were used. Circles represent the selectivity, rectangles represent the etch rate.*

pared to the micrographs in Fig. 6.5-b (at 250 W RF power) and in Fig. 6.4-a (at 300 W

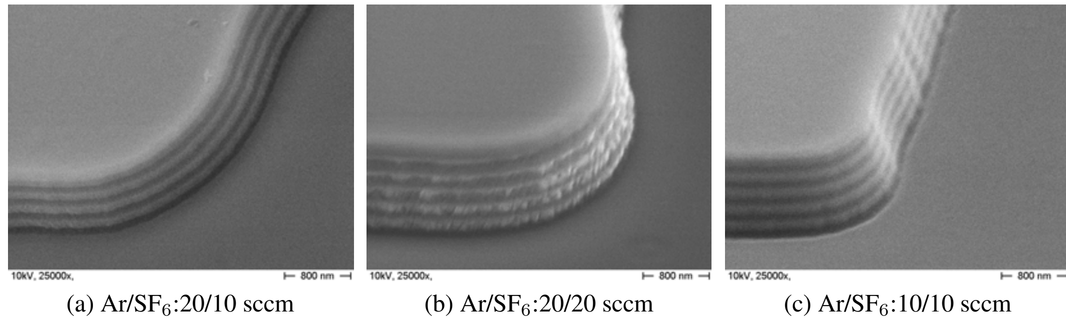

(a) Ar/SF_6:20/10 sccm (b) Ar/SF_6:20/20 sccm (c) Ar/SF_6:10/10 sccm

Figure 6.4: *SEM micrographs of the etched mirror at etch condition of 500 W ICP/300 W RF, 20°C, a pressure of 10 mTorr.*

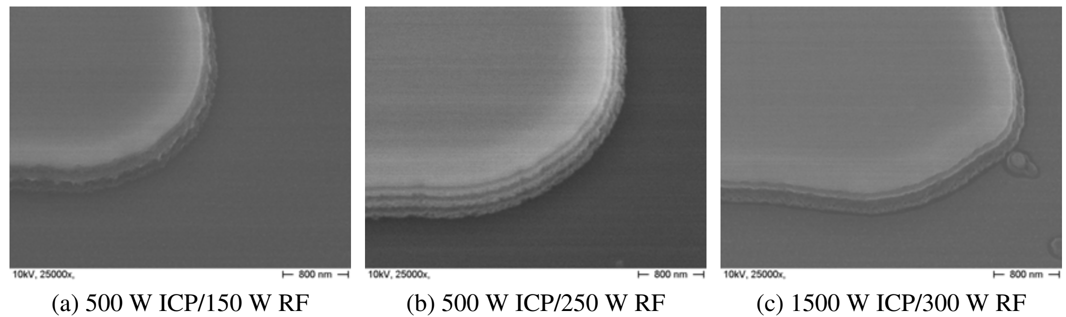

(a) 500 W ICP/150 W RF (b) 500 W ICP/250 W RF (c) 1500 W ICP/300 W RF

Figure 6.5: *SEM micrographs of the etched mirror with the etch condition: Ar/SF_6: 20/10 sccm, 20°C, a pressure of 10 mTorr.*

RF power). At 300 W RF power, relatively smooth vertical sidewalls was observed. The DC bias increased as the RF power increased, hence, the ion energy was enhanced and the etch rates increased.

Figure 6.7 shows that by increasing of the ICP power the plasma density will be increased. In high plasma density the particles (i.e. neutrals, radicals and ions) moved unfreely due to collisions between them. It caused ions with less energies that reached the target material being etched, hence, etch rates had tendency to decrease. This trend was observed as the power increased from 200 up to 1000 W. At 1000 W ICP power, high ion densities

Table 6.2: Etch experiments for structuring of the TiO_2/SiO_2 DBRs in ICP-RIE: variation applied power.

Etch condition 10mTorr,20°C,Ar/SF_6:20/10 sccm		Etch rate
ICP 500 W	RF varied	increased as RF power increased
RF 300 W	ICP varied	decreased as ICP power$\leq$1000 W increased as ICP power$>$1000 W

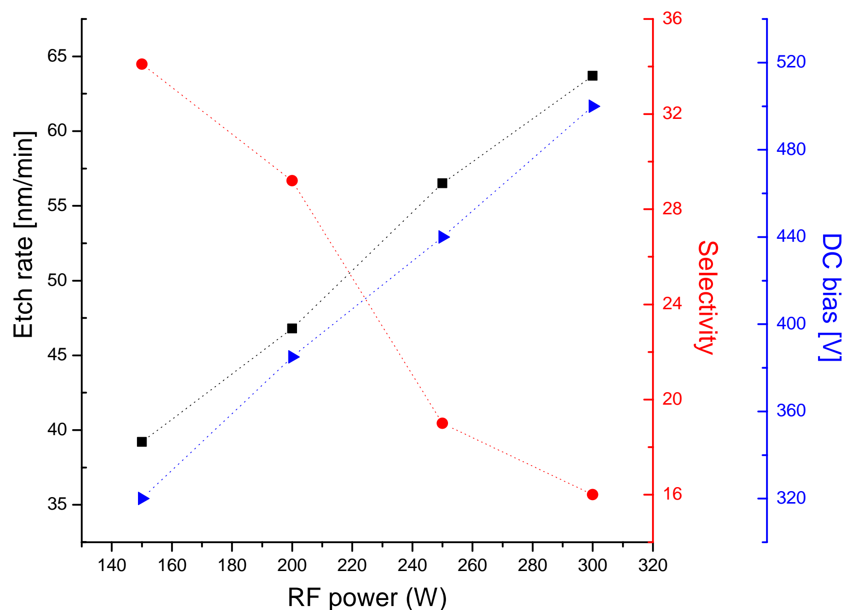

Figure 6.6: *Etch rates and selectivities as a function of RF power, at fixed 500 W ICP power. Etch condition: Ar/SF$_6$=20/10 sccm, 20°C, 10 mTorr. ITO etch masks were used. Circles represent the selectivity, rectangles represent the etch rate, and triangles represent the dc bias.*

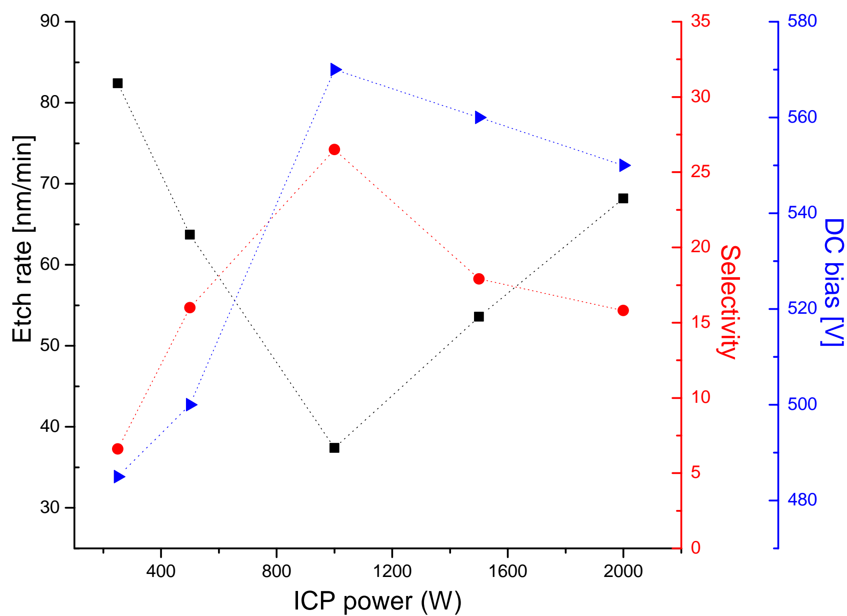

Figure 6.7: *Etch rates and selectivities as a function of ICP power at a fixed 300 W RF power. Etch condition: Ar/SF$_6$=20/10 sccm, 20°C, 10 mTorr. ITO etch masks were used. Circles represent the selectivity, rectangles represent the etch rate, and triangles represent the dc bias.*

Table 6.3: Etch experiments for structuring of the TiO_2/SiO_2 DBRs in ICP-RIE: variation pressure and temperature.

Etch condition		Etch rate
Pressure varied	20°C,500 W ICP/300 W RF, Ar/SF_6:20/10 sccm	decreased @pressure≤20mTorr increased @pressure>20mTorr
Temperature varied	6mTorr,500 W ICP/300 W RF, Ar/SF_6:20/10 sccm	increased,as temperature increased

induced the sputter rate to dominate the process. Meanwhile etch rates of the mirrors decreased, since at this stage the mirrors was etched unselectively. Important to note that at 1000 W ICP power with 20 mTorr, high concentration of ionizable particles were found to be sufficient, and they maximized the sputter rate. However, as the coil power increased, higher plasma density was again introduced and more collisions occured. Due to the collisions, large amount of less energized particles were produced, hence the sputter rate was reduced. Etch rates of the mirrors could be increased.

ICP power of higher than 700 W resulted in sidewalls roughness, it showed by the etched profile in Fig. 6.5-c (at 1500 W ICP power), compared to the one in Fig. 6.4-a (at 500 W ICP power).

The etching processes involving the variation of pressure and temperature are shown in Table 6.3. And the results are shown in Fig. 6.8, where the etch rates and selectivities as a function of the process pressure are depicted. A mixed of Ar/SF_6 flow rate of 20/10 sccm was selected, with the temperature of 20°C and a combination power of 500 W ICP/300 W RF. By increasing the pressure, from 6 mTorr up to 20 mTorr, the etch rate tended to fall whereas the selectivity showed a growing trend. Ion energies were high at low pressure, they have sufficient velocities to etch the mirrors, hence, higher etch rate was achieved. As the pressure increased, the collisions of ions reduced their velocities and ion energies became less, therefore the etch rates decreased. At pressure of 20 mTorr with 500 W ICP power, the condition where maximum of the sputter rate was obtained, the density of high ionizable particles was sufficiently high. The maximum sputter rate resulted in decreasing of the etch rate of the mirrors and increasing of the etch rate of the mask. At higher pressures ≥20 mTorr, lower quality sidewalls were observed. Further increasing of the pressure reduced the sputter rate, hence, etching process of the mirrors became more selective. The highest etch rate of approximately 80 nm/min and excellent etched profiles were obtained at pressure of 6 mTorr.

The etching process with varying temperatures was executed at the etch condition of mixture Ar/SF_6 gases was equal to 20/10 sccm, combination of 500 W ICP/300 W RF power with temperature of 20°C, and pressure of 6 mTorr. The etch rate increased following the increase in the temperature (Fig. 6.9). Relatively higher temperatures led to excellent etched profiles, as can be seen in Fig. 6.10. Residues or etch byproducts that were observed on the sidewall at temperature of -30°C, were eliminated as the temperature

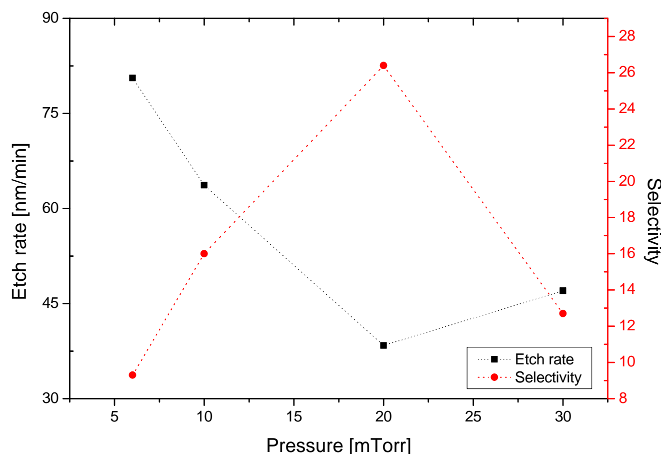

Figure 6.8: *Etch rates and selectivities as a function of the process pressure. Etch conditions: 500 W ICP/300 W RF, Ar/SF*$_6$*:20/10 sccm. ITO etch masks were used. Circles represent the selectivity, rectangles represent the etch rate.*

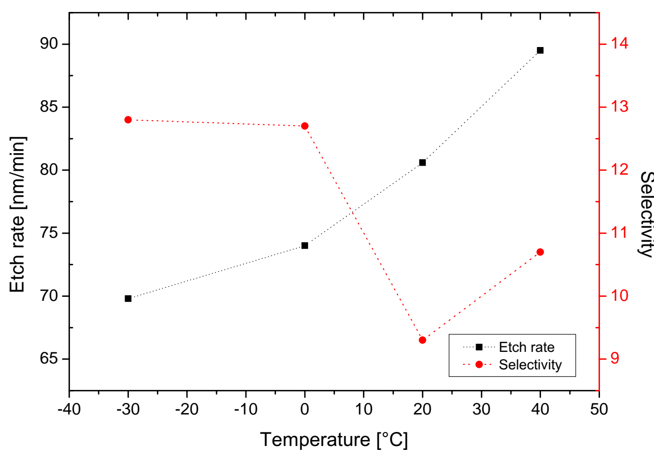

Figure 6.9: *Etch rates and selectivities as a function of the temperature. Etch conditions: 500 W ICP/300 W RF, Ar/SF*$_6$*:20/10 sccm. ITO etch masks were used. Circles represent the selectivity, rectangles represent the etch rate.*

increased, to 20°C (Fig. 6.10-b) and to 40°C (Fig. 6.10-c).

6.1.2 Etch process in the CCP- and the ICP-RIE: using photoresist etch masks

Two photoresists were examined as etch masks for the experiments. Etch mask made of photoresist was patterned by the lithography process. The resist was spun with a spin coating with the corresponding spin speed. To obtain 1.8 μm thickness of the AZ1518 photoresist, a 4000 rpm was used. For the negative photoresist, AZnLoF2070 diluted 5:1, 3.5 μm was obtained at a spin speed of 3000 rpm. The completed lithography steps for pattering the photoresist mask are given in the appendices.

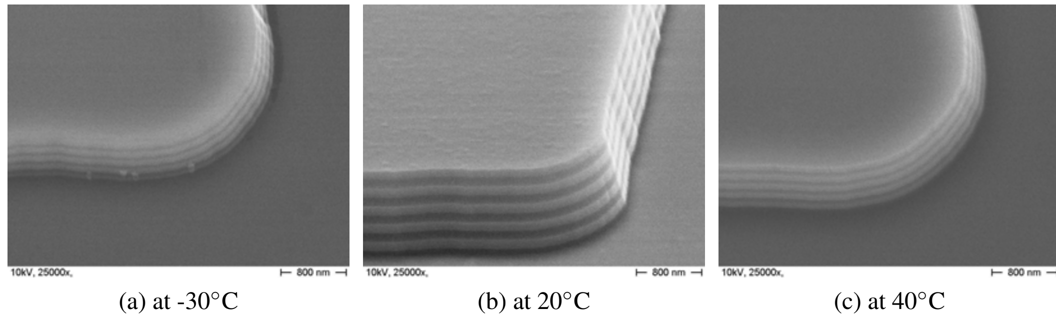

(a) at -30°C (b) at 20°C (c) at 40°C

Figure 6.10: *SEM micrographs show the etched mirrors. Etch conditions: Ar/SF_6: 20/10 sccm, 500 W ICP/300 W RF, 6 mTorr (a) at -30°C, an etch rate of approximately 70 nm/min was obtained; residue was observed on the sidewall, this effect can be eliminated by applying higher temperature; (b) at 20°C, an etch rate of 80 nm/min was obtained, and (c) at 40°C, an etch rate of approximately 90 nm/min was obtained. ITO etch masks were used.*

6.1.2.1 Etch process in the CCP-RIE

In the CCP-RIE an investigation on dry etching of each dielectric film was accomplished at the beginning, as shown in Table 6.4.

Table 6.4: Etch experiments for structuring of TiO_2, SiO_2, and the DBRs in the CCP-RIE.

Material	Etch condition	Etch rate (nm/min)
TiO_2	Ar 4sccm, SF_6 varied, 50W, 18.75mTorr, 12.5°C	8 up to 17
SiO_2		15 up to 21
TiO_2/SiO_2	Ar/SF_6:4/7sccm, 50W, 18.75mTorr, 12.5°C	≅20

The AZ1518 photoresist was used as etch mask. The etch rates and etch selectivities of TiO_2 and SiO_2 film were determined and plotted in the following graphs, Fig. 6.11 and Fig. 6.12. As expected, an increase in the etch rate of oxide films was observed along with the increasing of the SF_6 gas flow rate. The selectivities had tendency to decrease as the SF_6 flow rate increased, since at this condition etch rates of the photoresist masks increased.

Afterwards, the etching tests were performed for the DBRs, that is the multilayers of TiO_2/SiO_2. An etch rate of 20 nm/min of TiO_2/SiO_2 DBRs was obtained, by the process with Ar/SF_6 flow rate of 4/7 sccm, at a temperature of 12.5°C, a pressure of 18.75 mTorr and using 50 W RF power. The structure after etching was observed under an SEM showing a good quality of the structure surface, no pits or polymerization were shown. However, *step-like* sidewalls were detected due to the rounding of photoresist mask sidewall. From the equation (3.26) it is clear that a low slope angle of the mask leads to low slope angle of the etched profile. And since the selectivity was less than 1, i.e. of nearly 0.6, hence, the slope angle of the profile was only around 82° if the estimated mask's slope angle was 85°. This roundening photoresist sidewall was normally happened after

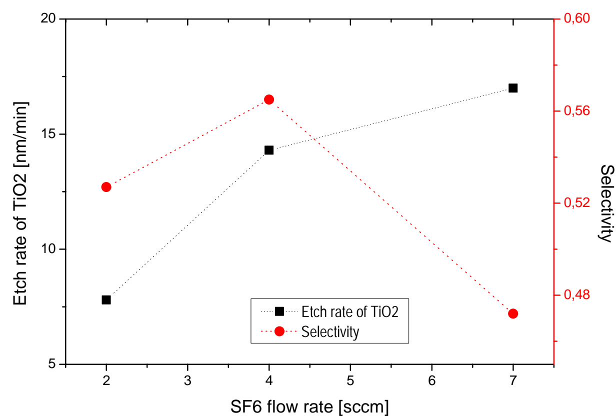

Figure 6.11: *Etch rates of TiO_2 film in the CCP-RIE, as a function of varied SF_6 flow rate. Etch condition: Ar flow rate of 4 sccm, 50 W RF power, 18.75 mTorr.*

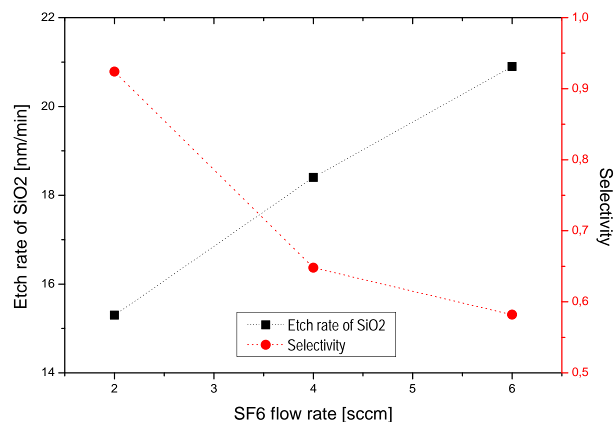

Figure 6.12: *Etch rates of SiO_2 film in the CCP-RIE, as a function of varied SF_6 flow rate. Etch condition: Ar flow rate of 4 sccm, 50 W RF power, 18.75 mTorr.*

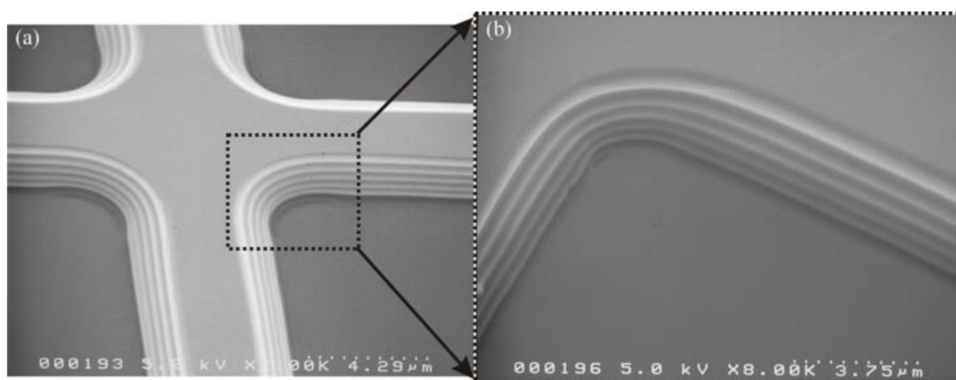

Figure 6.13: *SEM micrographs of TiO_2/SiO_2 DBRs after etching in the CCP-RIE for 40 min; the filter membrane with four suspensions (left). Step-like structure of etched edges was observed, due to the rounding sidewall of the photoresist mask (right).*

the hardbake step, therefore, reducing the hardbake-time or -temperature, is a possible solution to overcome this problem. Fig. 6.13 shows SEM graph of the DBRs etched profile.

6.1.2.2 Etch process in the ICP-RIE

The experiments were carried by varying the RF power at the pressure of 6 mTorr and 10 mTorr, as summarized in Table 6.5. Figure 6.14 and Fig.6.15 in the following show etch rates and selectivities of the mirror over the photoresist masks, as a function of RF power at a fixed ICP power of 500 W.

Table 6.5: Etch experiments for structuring of the TiO_2/SiO_2 DBRs in ICP-RIE: photoresist masks.

Etch mask	Etch condition: Ar/SF_6:10/10 sccm, 20°C, 500 W ICP/RF varied	Etch rate (nm/min)
AZ1518	6 mTorr 10 mTorr	75 @180 W RF 44 @180 W RF
AZnLoF2070 5:1	6 mTorr 10 mTorr	78 @180 W RF 45 @180 W RF

- *Positive photoresist as etch mask.* The AZ1518 photoresist was patterned through the optical lithography. Resist thickness of approximately 1.8 μm was obtained. Maximum etch rates of approximately 75 nm/min and 44 nm/min were achieved in the process using 6 mTorr and 10 mTorr, respectively. An etch selectivity of the mirrors over photoresist mask of approximately 0.33 in average was achieved. An SEM graph in Fig. 6.16-right showed an etch profile of the mirror, that was etched for 5 min, at 160 W RF power and pressure of 6 mTorr. The image was taken after the removal of the etch mask.

- *Negative photoresist as etch mask.* After patterning through the optical lithography, the thickness of AZnLoF2070 5:1 of 3.5 μm was obtained. Maximum etch rates of approximately 78 nm/min and 45 nm/min were achieved in the process using 6 mTorr and 10 mTorr, respectively. These etch rates are relatively higher than the ones obtained in process using the positive resist mask. The profile shown in Fig. 6.16-left exposed low quality of surface structure especially around the edges. Resist negative sidewall might cause this phenomena, since it had undercut profile that might be etched away during the process, and led to the damage surrounding the structure edges.
  However, if 250 W RF power was used at 6 mTorr, the etch profile in Fig. 6.17 showed much better quality, compared to the one shown in Fig. 6.16-left. Figure 6.17 also shows an WLI image of the structure after etching for 10 min. An etch rate of 85 nm/min with selectivity S$\cong$0.3 for the mirror over the photoresist mask was

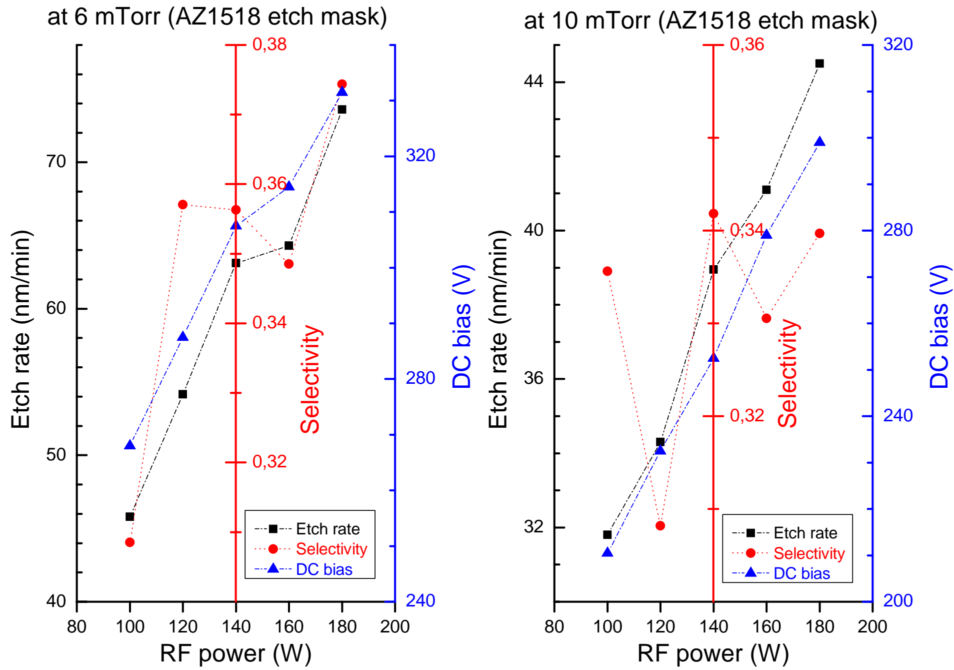

Figure 6.14: *The etch behaviour of TiO_2/SiO_2 in ICP-RIE, using positive AZ1518 photoresist as etch mask, at process pressure of 6 mTorr (left) and 10 mTorr (right).*

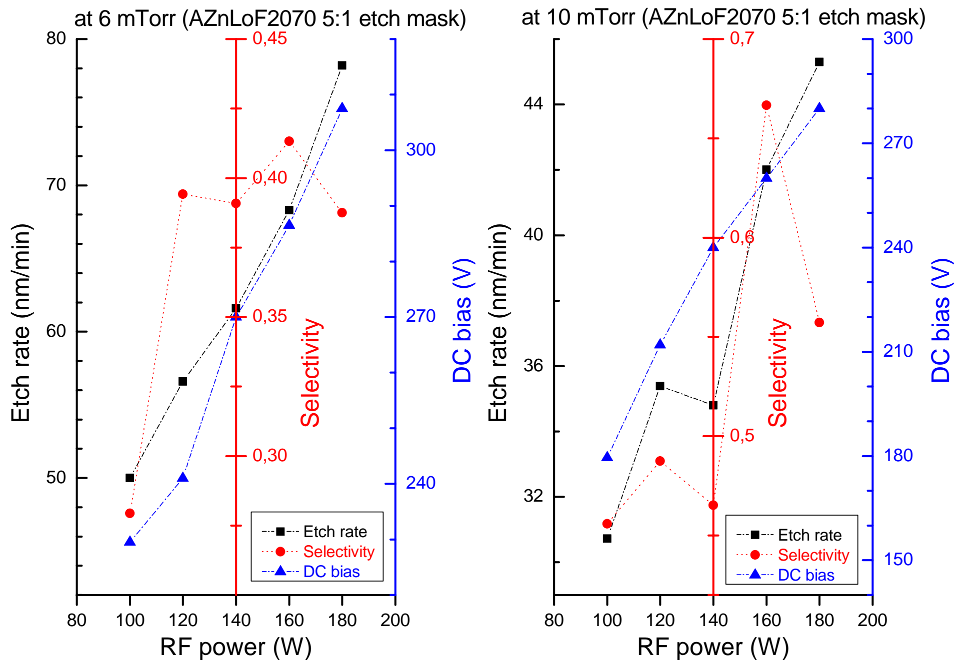

Figure 6.15: *The etch behaviour of TiO_2/SiO_2 in ICP-RIE, using negative photoresist, AZnLoF2070 5:1, as etch mask, at process pressure of 6 mTorr (left) and 10 mTorr (right).*

achieved, in an etch conditions of 500 W ICP/250 W RF power with temperature of 20°C, at a pressure of 6 mTorr.

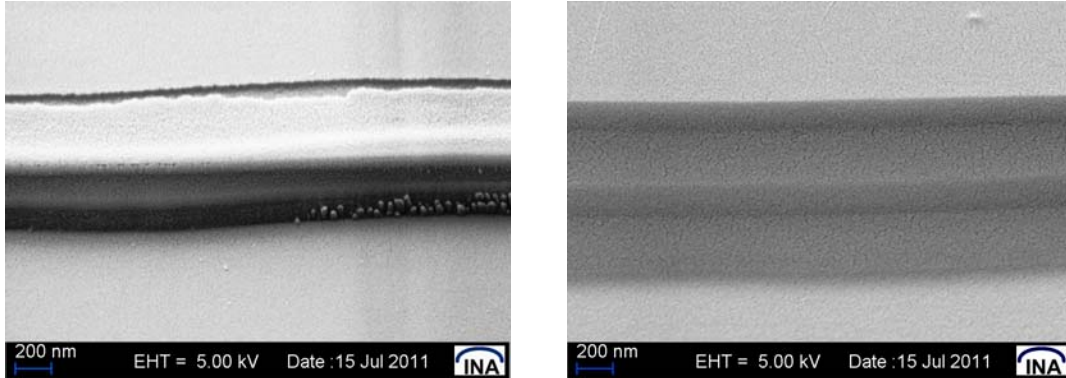

Figure 6.16: *SEM graphs of the etched profile of the mirrors, which were etched using the AZnLoF2070 5:1 mask (left), and using the AZ1518 mask (right). Etch condition: 500 W ICP/160 W RF power, Ar/SF$_6$=10/10 sccm, pressure of 6 mTorr, at 20°C; the etch time was 5 min. The pictures were taken after removing of the etch mask.*

The results show that as the RF power increased, the etch rates increased. As expected at the process pressure of 6 mTorr, relatively higher etch rates were obtained and the mirrors were etched more selectively, compared to the ones at the pressure of 10 mTorr. If more than 160 W of RF power was used in the etching process, NMP solvent which was heated at 70 up to 80°C was necessary to remove the resist mask. Helium can be added to the etching process wherein the photoresist mask being used, to prevent the heating of the resist mask during the process.

6.2 UV-NIL Polymers as the Cavity Layer

The PAK-01, mr-UVCur06 and mr-UVCur21 polymers were investigated to be utilized as the cavity layers for the TiO_2/SiO_2 DBRs-based filter. Compatibility of the mr-UVCur21 polymer to the DBRs had been examined, and the filter arrays with different cavity heights made of this polymer was fabricated. Array of these cavities with different heights was accomplished by the UV-Nanoimprint process [110]. In this section the PAK-01's adhesion problem and an investigation on the mr-UVCur06 are presented.

6.2.1 PAK-01 Polymer

The preceding chapter presented the compatibility of the PAK-01 polymer, which was diluted with an ether (Ethylen-glycol-monomethylether), to the DBRs deposited by the PECVD process. Compatibility of this diluted polymer to TiO_2/SiO_2 DBRs sputtered by IBSD technique also evaluated in this work, and it is presented in this subsection.

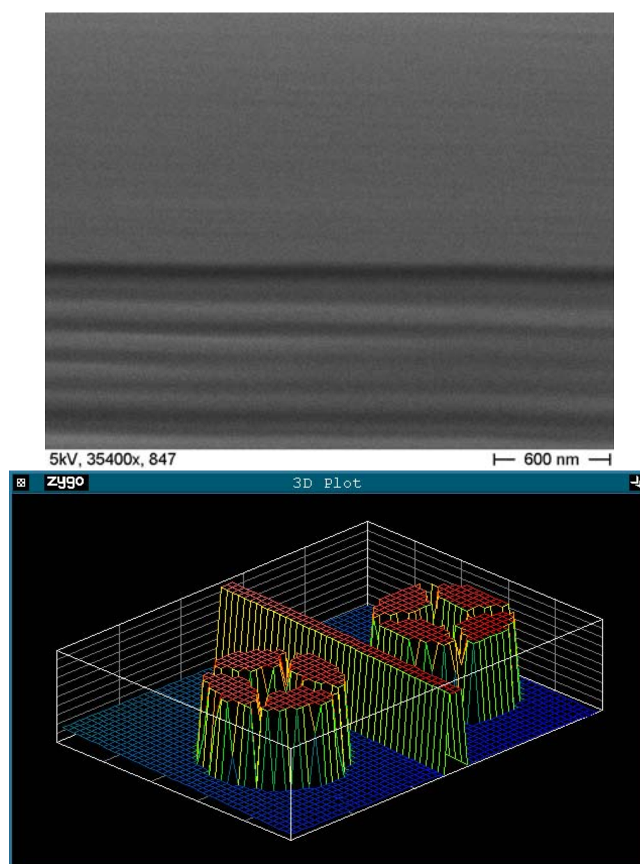

Figure 6.17: *An SEM image shows the sidewall of the mirror after etching for 10 min under AZnLoF2070 5:1 mask. A WLI image (right) depicts the filter structure with four suspensions; Ra (average roughness) of the structure measured by the WLI was approximately $\leq$10 nm.*

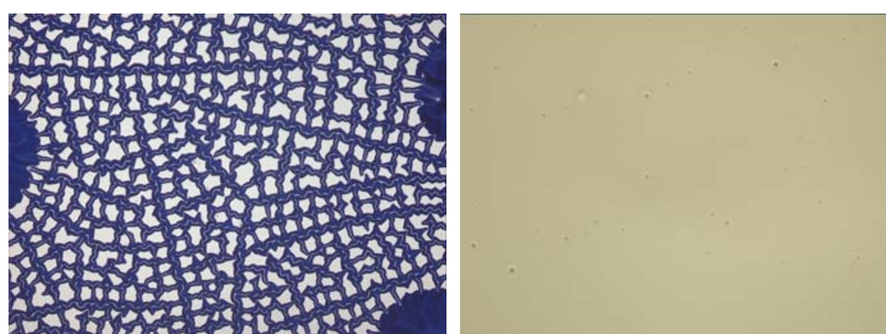

(a) Filter surface with PAK-01 (diluted 4:1) polymer as cavity layer

(b) Filter surface with mr-UVCur06 polymer as cavity layer

Figure 6.18: *Surface profile of the filters; images were taken by Leica microscope on the sample, after sputtering of the DBRs on the diluted PAK-01 (a), and on the mr-UVCur06 (b).*

the polymer will be coated on the top of bottom DBRs, where the TiO_2 layer is located. TiO_2 has hydrophilic surface and an adhesion promoter TI-Prime was used to improve the adhesion of the polymer to bottom DBRs. The TI-Prime was applied through spin coating on the bottom DBRs, and subsequently the polymer was spun at 4300 rpm to fit the central wavelength of 550 nm. However, the result, that was observed after sputtering of the top DBRs on the polymer, exhibited unhomogeneous surface profile, as can be seen in Fig. 6.18-left. One possibility that might cause this effect is the incompatibility of the diluter ether to the PAK-01 polymer. This led to weak chemicaal bond of the solution and it was easy to break down due to higher ion bombardments in the IBSD process. Low pressure of less than 0.07 mTorr is used in the IBSD process, meanwhile the deposition in PECVD utilized high pressure, between 0.65 to 1 Torr for depositing the Si_3N_4/SiO_2, hence, this phenomenon was undetected.
For further experiment, which is not covered in this work, the 1-methoxy-2-propanol ($C_4H_{10}O_2$) solvent will be used for the diluting process. This diluter's compatibility to PAK-01 polymer have been investigated by Toyo-Gosei. Experiments regarding this polymer are required to investigate its compatibility to SCIL (Substrate Conformal Imprint Lithography) process as one of nanoimprint technology method, which will be used for the fabrication of different cavity thicknesses of the filter arrays.

6.2.2 mr-UVCur21 and mr-UVCur06 Polymers

Filters which were processed with mr-UVCur21 showed good surface profile observed by the Leica optical microscope. An adhesion promoter mr-APS1 was used to improve good adhesion between the polymer and the DBRs. Figure 6.19-a shows a surface of sample where the coating of mrUVCur21 was applied without the promoter mrAPS1, the filter was unstructured. Al layer covered the light-blue area, since for this sample a negative photoresist was used for patterning the Al film, hence the filter structure was uncovered with Al film. It showed clearly that the surface of the filter looked inhomogeneous, since the polymer layer underneath reflected different colors. Inhomogeinity layer contributed to pinholes and surface damage which were observed after the dry etching process. Comparing this sample to another one, Fig. 6.19-b, where the adhesion promoter mr-APS1 was used for coating of the mr-UVCur21. The filter surface looked relatively homogeneous even after the etching process performed. Detail step of the spin coating of mr-UVCur21 polymer is given in the appendix.
A homogeneous filter surface was observed under the Leica microscope, as the top DBRs sputtered on the crosslinked mr-UVCur06 polymer layer (Fig. 6.18-right). The coating process was performed as mentioned in the preceding chapter, that is the sample was baked on a hotplate at 150°C for approximately 30 min, and subsequently the adhesion promoter mr-APS1 was spun. The speed of 5000 rpm for 60s was selected to obtain thickness of 20 nm, according to the manufacturer [111]. After that the sample was baked at 150°C for 30s up to 40s. The polymer was spun and baked at 80°C for 1 min and exposed under UV light for 5 min with nitrogen ambient. Image of the filter array that was structured in the CCP and the photoresist mask was still on the mirrors is shown in the following (Fig. 6.20), homogeneous surface profile was observed.

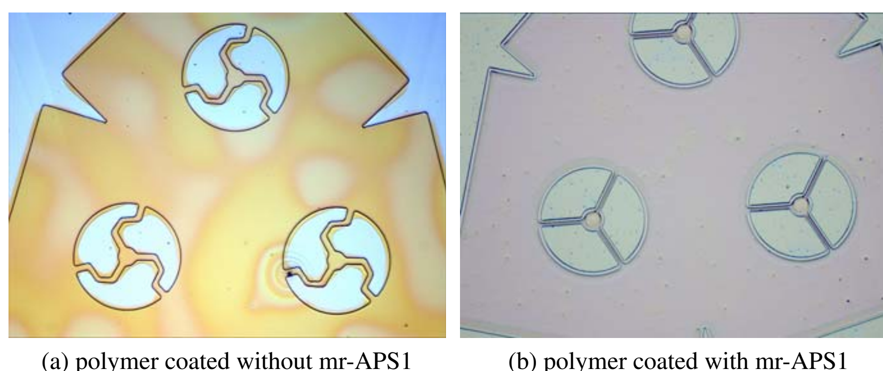

(a) polymer coated without mr-APS1 (b) polymer coated with mr-APS1

Figure 6.19: *Images were taken by Leica microscope of the sample filter before dry etching process, where mr-UVCur21 polymer coated without the mr-APS1 (a), and the sample filter after dry etching, where the polymer used the adhesion promoter mr-APS1 in the coating process (b).*

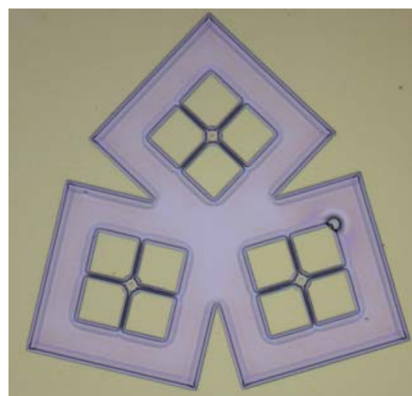

Figure 6.20: *Image of filter array (mr-UVCur06 cavity layer) was taken by Leica microscope, after lateral structuring of the top DBRs in the CCP-RIE, with AZ1518 photoresist etch mask.*

6.3 The Contact Electrodes: ITO and Al Layers

For this type of filters, ITO and Al conductive layers as contact electrodes were utilized. ITO layer of nearly 80 nm in thickness as the bottom electrodes were sputtered on the glass substrate, and Al layer as the top electrodes were evaporated on the top DBRs. After the sputtering process, the ITO bottom electrode was treated by the RTA. Structuring of the Al top electrodes were performed through a lift-off process. This step was performed by the lithography of a negative photoresist, AZnLoF2070 diluted 5:1, followed by the evaporation of Al film of 100 nm in thickness. The sample subsequently was soaked into NMP solvent for 5 to 10 min to lift-off the unwanted Al film. In order to be able to lift-off small structures of about less than 10 μm, the sample was soaked into the NMP solvent heated at 75°C for at least 15 min. Patterning the Al electrodes can also be achieved through wet etching process. This wet etching process has to be controlled, to avoid overetching of the Al film which may lead to etch away of the electrode structure and attack the first layer of the DBRs.

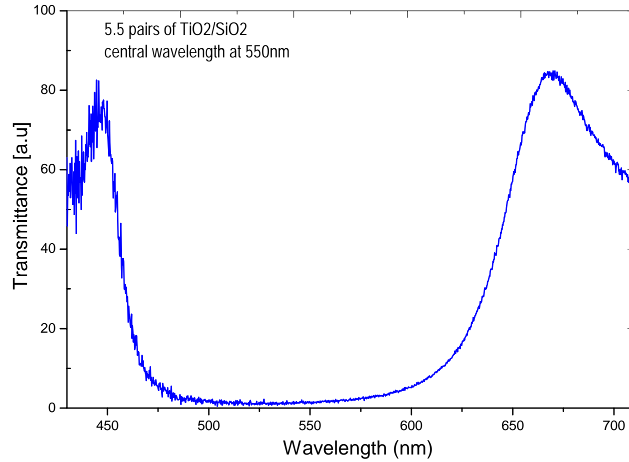

Figure 6.21: *The optical properties of 5.5 pairs of TiO_2/SiO_2 bottom DBRs, with central wavelength 550 nm.*

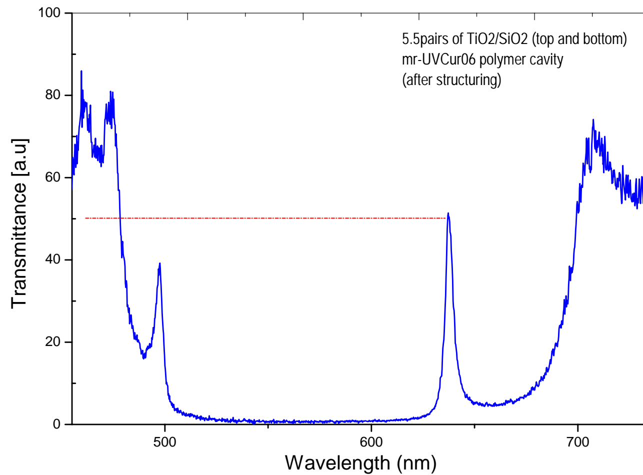

Figure 6.22: *The optical properties of TiO_2/SiO_2 DBRs-based filter, with mr-UVCur06 as the cavity material, measured after removing of the etch mask.*

6.4 Results and Discussion

The stopband of bottom DBRs measured by microscope-base spectrometer is shown in Fig. 6.21, the 5.5 pairs of TiO_2/SiO_2 was deposited on the glass substrate, which was sputtered with ITO, with 550 nm of central wavelength. With only few numbers of layers, a bandwidth of more than 150 nm could be obtained. The mr-UVCur21 and mr-UVCur06 polymers could be utilized as filter cavity layers. Their adhesion between TiO_2 layers could be improved by appyling the adhesion promoter.

A filter transmission peak with a FWHM of approximately 4 nm was observed after accomplishment of structuring of the top DBRs, it is shown in Fig. 6.22. The measurement was taken after removing of the photoresist mask. A stopband of 175 nm was achieved. The mr-UVCur06 polymer was spun at 2700 rpm to obtain the thickness of 275 nm. The filter consisted of 5.5 pairs of DBRs designed for 550 nm central wavelength, however it shifted to 580 nm (as the top DBRs transmittance was measured). Hence, the observed transmission peak was shifted as well.

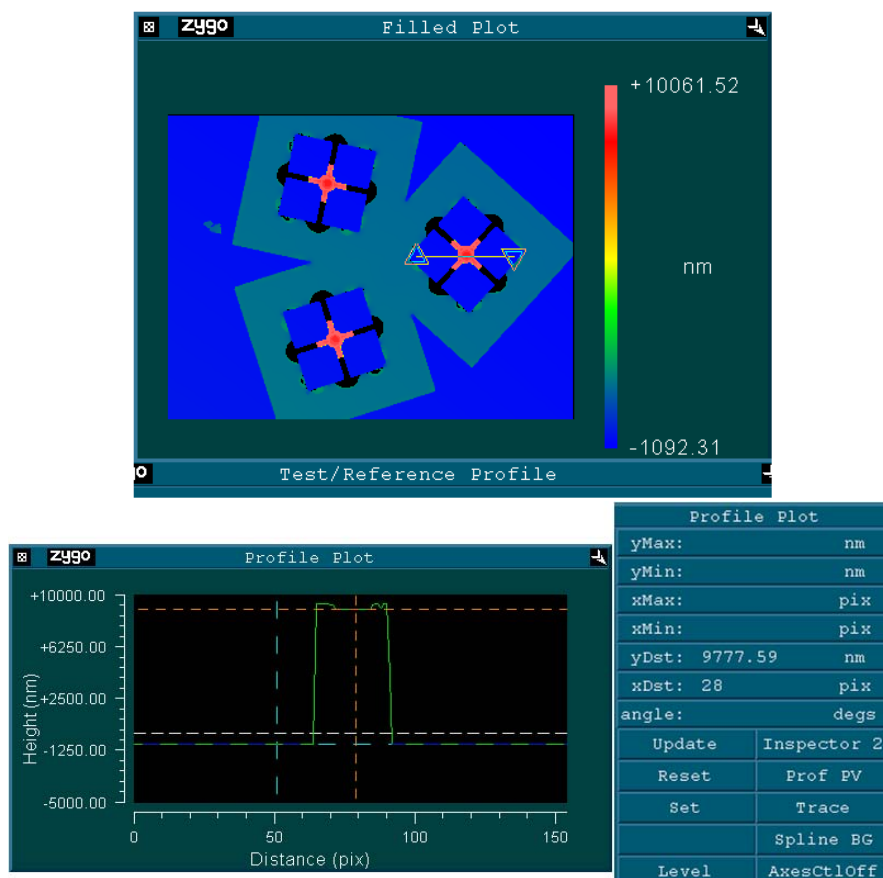

Figure 6.23: *WLI image of released filter arrays, the displacement of membrane was nearly 10 μm after the underetching process. The measured profile showed that the height of membrane in the vertical (y) direction was 9777.59 nm.*

Underetching of the polymer sacrificial layer was succesfully performed, refering to the aforementioned underetch rate (Chapter 5). The polymer being removed was mr-UVCur21 which spun at 3600 rpm, for 550 nm central wavelength. The following images obtainde from the WLI measurement, show the filter membrane with 30 μm in diameter, and four straight suspensions released after 18min underetched in the oxygen plasma (Fig. 6.23). The membrane structure bent 9.8 μm.

The filter structures after the underetching process in the oxygen plasma were also observed by an SEM, and the following micrographs (Fig. 6.24) were taken. The two type filter structures show difference height in the displacement, as predicted by the model simulation. The structure with a membrane diameter of 30 μm, and with the suspensions width of 10 μm is shown in the top side (Fig. 6.24-top), it exhibited 10 μm of displacement height. Another structure, whose curl bent suspensions and smaller membrane, of 25 μm, showed less deformation (Fig. 6.24-bottom), that is of approximately a half of the

displacement of the filter whose straight suspensions.
The underetching process was accomplished, and the filter membranes were completely released. However, the optical properties showed low quality of the filter linewidth, less than 20% of transmission peak was observed as shown in Fig. 6.25. This was probably due to the displacement of filter membranes that reached of approximately 10 μm, hence, this cavity height laid beyond the filter wavelength design. The tuning performance was finally not achieved. One of the reasons that caused this shortcoming is a high displacement of the membrane led to extremely narrow FSR. Theoretically speaking, only around 15 nm FSR was achieved when the magnitude of membrane displacement reached 10 μm, with respect to the central wavelength of 550 nm. A high displacement resulted in large separation between the two mirrors, hence, the capacitance which yielded in the air-gap filter structure was very small. Therefore, the voltage requirement, that is inversely proportional to the capacitance, for the actuation purpose should be sufficiently high.

Conclusion

Lateral structuring of the TiO_2/SiO_2 DBRs in the RIE process have been performed and optimized, using different etch masks, and the quality of the etched profiles was observed by means of an SEM. Etch selectivity S>9 that calculated from the etch rate of the mirrors over the ITO mask, was obtained under an etch condition of 500 W ICP/250 W RF with temperature of 20°C up to 40°C at a process pressure of 6 mTorr. The optimum etch rates of the TiO_2/SiO_2 DBRs, i.e. 80 to 90 nm/min were obtained under this etch condition. The etching process resulted in excellent structure profiles, i.e. steep sidewalls and smooth surface. A high etch selectivity S=16 was obtained at a process pressure of 10 mTorr, however, the etch rate decreased to approximately 65 nm/min.
The photoresists as etch masks were also examined to investigate the profile of the etched mirrors. Those experiments gave benefit if the Al film replaced the ITO as the top electrodes, since the photoresist mask was used formerly for patterning the Al film in wet etching process, then it can be utilized subsequently as the mask for structuring the mirrors in the RIE process. The AZ1518 photoresist mask showed promising results, a good quality of the etched profile was observed in an etch condition of 500 W ICP/160 W RF power, with a mixture of Ar/SF_6 gases of 10/10 sccm, a process pressure of 6 mTorr, at 20°C. At applied power of 500 W ICP/250 W RF the etching process using a negative photoresist mask, AZnLoF2070, exhibited a smooth surface profile, and relatively high etch rate of 85 nm/min was obtained.

Compatibility of the mr-UVCur21 and mr-UVCur06 polymers to the TiO_2/SiO_2 DBRs have been evaluated. Homogeinity of the mirror surface after the sputtering process was observed. The underetching step was accomplished completely to release the filter membranes.
The material stress in the mirror materials led to high displacement of the filter membranes, hence, it contributed to small capacitances between the mirrors. The charge in the air-gap filter structure was difficult to control, since the voltage which was required for the actuation purpose should be sufficiently high. The filter membrane that deflected of approximately more than 5 μm led to the loss in the transmission peak, hence, the

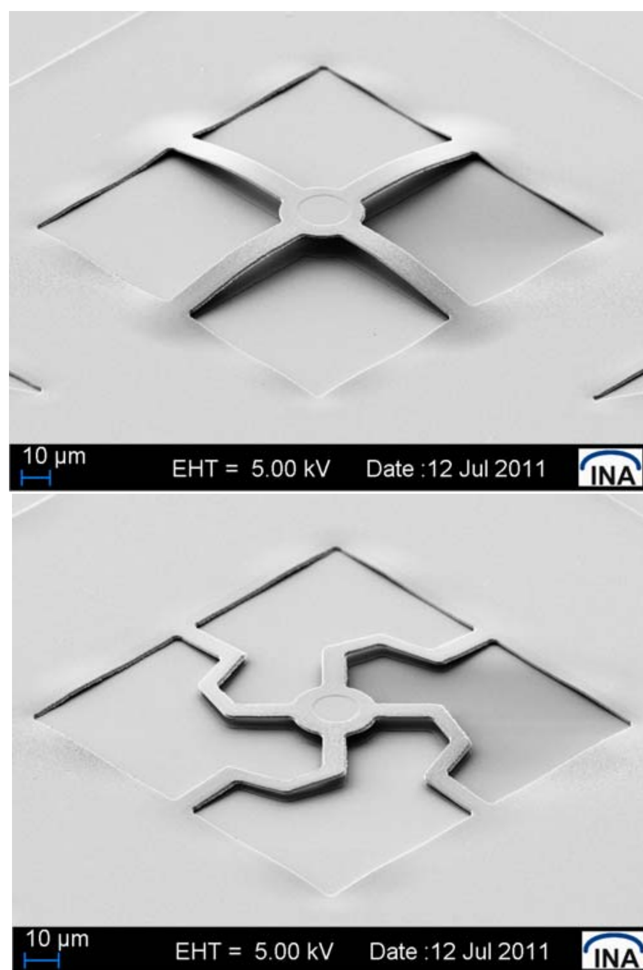

Figure 6.24: *The filter membranes that were released after the underetching process for 18 min: the filter with four-straight suspensions (top), and four-curl bent suspensions (bottom) which displaced less (approximately a half of the displacement of the filter whose straight suspensions).*

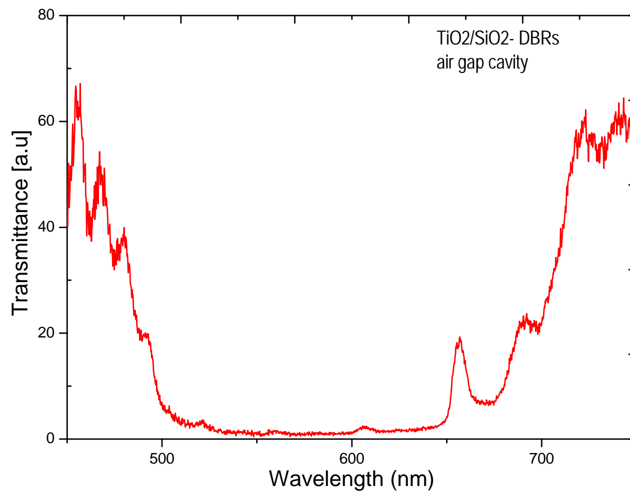

Figure 6.25: *Transmission peak of the filter, measured by a micropcope spectrometer after underetching process.*

transmission peak decreased. To overcome this problem, a study in controlling the stress induced by the ion beam sputtering method is necessary. Reducing the residual stress will prevent high displacements of the filter membranes, and it can improve the properties of the tunable TiO_2/SiO_2 DBRs-based filters. Moreover, new filter structures designs that consider utilizing the small membrane diameters and thinning of the suspensions will lead to less membrane displacements and less actuation voltages, and in turn it can solve these shortcomings.

Chapter 7

Summary and Outlook

WITHIN this work two different types of DBRs-based Fabry-Pérot filters were investigated. A tunable filter consisting of Si_3N_4/SiO_2 with air gap cavity, and a high index contrast TiO_2/SiO_2-DBRs based filters were fabricated by surface micromachining methods. The filter arrays are designed for the implementation in a nanospectrometer. In this report their designs for the fabrication of a high-precision colour sensor in the visible spectral range are presented. Experiments and a simplified numerical model were conducted to obtain compatible fabrication processes regarding the utilized materials, and the optimal filter structures design.

Several filter designs were introduced, therefore, to obtain the optimal structure design, a simplified numerical model was utilized to investigate the displacement (or deflection) of the membrane regarding of various filter geometric structures. The model used FEMLAB/Comsol Multiphysic software to evaluate the displacement profile of the filter membrane. The evaluation showed that the geometric shape and size of the membrane together with their suspensions are crucial, since they both influence the displacement magnitude. Longer and narrower suspensions both led to higher displacements of the membrane. This effect was found also by enlarging on the membrane diameter. The filters with curl-bent suspensions bent more than the ones with straight or bent suspensions. These phenomena were also found in the experimental results.

The tunable filters with Si_3N_4/SiO_2-DBRs and air gap cavities have been successfully fabricated. Low cost deposition method, the PECVD, was used to produced the dielectric mirrors. An investigation on the acrylate based polymers, i.e. the mr-UVCur06, mr-UVCur21 and PAK-01, was accomplished and it was established that they are compatible to the mirrors deposition process. These polymers worked as sacrificial layers and supporting post structures in the filter design. Removal of the crosslinked polymer sacrificial layer was accomplished in the oxygen plasma, hence the filter's air gap cavity was obtained. Lateral structuring of the mirrors in the CCP-RIE resulted in excellent etch profiles, wherein steep sidewalls and smooth surface of the structures were observed. AZ1518 photoresist as etch masks were utilized in the etching process, the etch rate of 30 nm/min and etch selectivity of approximately 3 for the mirrors over the etch mask

were achieved. The ICP-RIE can also be utilized to structure the mirrors with low applied power. An etch rate of 54 nm/min was achieved using a photoresist etch mask, and removing of the photoresist mask was accomplished subsequently in the ICP using O_2 gas.

Optical properties measurement yielded from one filter element showed a filter linewidth of approximately 4 nm, and with applied voltage up to 30 V, a tuning range of approximately 75 nm were obtained within 125 nm of filter stopband. Arrays of the tunable filters were also accomplished. They achieved a tuning range of approximately 70 nm with applied voltage between 0 V and 20 V. The filters mechanical properties showed that the displacement of the membrane depended on the filter geometric structures. The membrane with a diameter of 25 μm and suspensions width of 8 μm, displaced less than the one with a diameter of 10 μm and suspensions width of 6 μm (Chapter 5 page61). The structure with curl-bent suspensions had less displacement than the one with bent or straight suspensions (Chapter 5 page65).

TiO_2/SiO_2-DBRs based filters are potential filter devices with a broad stopband range, due to their high refractive index contrast, wherein only few layers of mirrors are required for the filters production. Optimization on the lateral structuring of the TiO_2/SiO_2 DBRs was presented and accomplished in this work. In the CCP-RIE, the etching process under photoresist etch mask yielded an etch rate of 20 nm/min, where relatively low selectivity of 0.6 was achieved. Using the ICP-RIE, the etch rate of 80 up to 90 nm/min was achieved under ITO etch mask, with selectivity $S>9$. Excellent etched profiles were achieved in the etching process using 500 W ICP/300 W RF power and a mixture of Ar/SF_6 gas flow rates of 20/10 sccm. Higher etch rates were obtained by applying a low pressure and increasing the temperature of the process.
Photoresist was found to be a good candidate as etch mask for the ICP-RIE process. Approximately 65 nm/min of etch rate was achieved at 160 W RF/500 W ICP power using photoresist AZ1518 mask, and using AZnLoF2070 mask, as 250 W RF/500 W ICP power was applied in the ICP, wherein etch rate of approximately 85 nm/min was obtained. Good quality of the etched profiles were achieved from both processes. Applying photoresist as etch masks gives benefit in the fabrication, since the patterning of photoresist can be accomplished by a customary optical lithography, without any adhesive or successive patterning steps such as lift-off process or wet etching that are required for applying hard etch masks.

Compatibility of the mr-UVCur21 and mr-UVCur06 polymers to the TiO_2/SiO_2 DBRs was evaluated, and the underetching process of the polymers was successfully performed. High stress in the thin film materials led to the loss in peak transmission since the membrane deflected of more than 5 μm. However, the fabricated filters that were compared to the simulation results (Chapter 4) showed good agreements in terms of the geometric designs which affected the membrane displacements, the filter membranes with curl-bent suspensions contributed less displacements compared to the displacements resulted from the ones with straight or bent suspensions.

The filter geometric structures and the residual stress in the dielectric layers influenced strongly the displacement of the filter membranes, which in turn yielded the change in filters transmission linewidths. To minimize these effects, the structures that lead to the least possible displacements are required for the new filter arrays design, and controlling the stress induced during the fabrication of the thin films are indispensable.
Further optimization on the tunable filter arrays is required to enhance the quality of the device for the application of a sensor or in a nanospectrometer. Implementation of the serial or cascade design of the filters according to the detector arrays will attain a broad tuning range which gives advantages for different field of applications.

Bibliography

[1] I. Young, V. Iordanov, A. Kroon, H. Dietrich, R. Moerman, L. van den Doel, G. van Dedem, A. Bossche, B. Gray, L. Sarro, P. Verbeek, and L. van Vliet, "Monitoring enzymatic reactions with in situ sensors," in *Microarrays and Combinatorial Technologies for Biomedical Applications: Design, Fabrication, and Analysis* (D. V. N. R. Raghavachari, ed.), vol. 4966, pp. 76 – 82, SPIE, SPIE, July 2003.

[2] V. Iordanov, G. Lubking, R. Ishihara, R. Wolffenbuttel, P. Sarro, and M. Vellekoop, "Silicon thin-film uv filter for nadh fluorescence analysis," *Sensors and Actuators A: Physical*, vol. 97-98, no. 0, pp. 161–166, 2002. selected papers from Eurosenors XV.

[3] A. Nilsson and L. G. M. Pettersson, "Chemical bonding on surfaces probed by x-ray emission spectroscopy and density functional theory," *Surface Science Reports*, vol. 55, pp. 49–167, 2004.

[4] P. Zarco-Tejada, O. Pérez-Priego, G. Sepulcre-Cantó, J. Miller, and E. Fereres, "Chlorophyll fluorescence detection with a high-spectral resolution spectrometer through in-filling of the o2-a band as function of water stress in olive trees," *2nd International Workshop on Remote Sensing of Vegetation Fluorescence*, November 2004.

[5] P. Lindblom, N. Meinander, and T. Olsson, "Spectroscopy with the mega spectrometer, a very high resolution grating spectrometer," *Review of Scientific Instruments*, vol. 61, pp. 2546–2548, 1990.

[6] R. Crocombe, "Miniature optical spectrometers: There's plenty of room at the bottom part i, background and mid-infrared spectrometers." http://spectroscopyonline.findanalytichem.com/spectroscopy/, January 2008.

[7] A. Tarraf, *Low-Cost Micromechanically Tunable Optical Devices - Strained Resonator Engineering, Technological Implementation and Characterization*. PhD thesis, University of Kassel, 2005.

[8] M. Bartels, S. Wittzack, F. Köhler, X. Wang, A. Albrecht, S. Schudy, M. Engenhorst, H. H. Mai, O. Setyawati, T. Woit, C. Woidt, and H. Hillmer, "High vertical resolution 3d nanoimprint technology for nanophotonic applications," in *IEEE/LEOS International Conference on Optical MEMS and Nanophotonics 2009*, pp. 87–88, IEEE, 2009.

[9] S. Wittzack, F. Köhler, X. Wang, O. Setyawati, T. Woit, A. Albrecht, M. Engenhorst, S. Schudy, C. Woidt., M. Bartels, and H. Hillmer, "Hochpräzise nanoimprint-templates für 3d-strukturen," *Galvanotechnik*, vol. Band 100, Heft 10, pp. 2376–2382, 2009.

[10] S. Y. Chou, P. R. Krauss, and P. J. Renstrom, "Nanoimprint lithography," *Journal of Vacuum Science Technology B: Microelectronics and Nanometer Structures*, vol. 14, pp. 4129 –4133, nov 1996.

[11] M. Vogler, S. Wiedenberg, M. Mühlberger, I. Bergmair, T. Glinsner, H. Schmidt, E.-B. Kley, and G. Grützner, "Development of a novel, low-viscosity uv-curable polymer system for uv-nanoimprint lithography," *Microelectronic Engineering*, vol. 84, no. 5-8, pp. 984–988, 2007. Proceedings of the 32nd International Conference on Micro- and Nano-Engineering.

[12] R. F. Wolffenbuttel, "State-of-the-art in integrated optical microspectrometers," *IEEE Transactions On Instrumentation And Measurement*, vol. 53, no. 1, pp. 197–202, 2004.

[13] J. Coates, "New microspectrometers: Building on the principle that simple is beautiful," *Spectroscopy (Instrumentation)*, vol. 15, pp. 21–27, December 2000.

[14] R. A. Crocombe, D. C. Flanders, and W. Atia, "Micro-optical instrumentation for process spectroscopy," in *Proceedings of the SPIE: Lab-on-a-Chip: Platforms, Devices, and Applications* (D. Smith, Linda A.; Sobek, ed.), vol. 5591, pp. 11–25, SPIE, 2004.

[15] R. Crocombe, "Miniature optical spectrometers, part iii: Conventional and laboratory near-infrared spectrometers." http://spectroscopyonline.findanalytichem.com/spectroscopy/, May 2008.

[16] V. Piotter, W. Bauer, T. Hanemann, M. Heckele, and C. Mueller, "Replication technologies for harm devices: Status and perspectives," tech. rep., Microsys Technol. Springer-Verlag, 2008.

[17] L. P. Schuler, J. S. Milne, J. M. Dell, and L. Faraone, "Mems-based microspectrometer technologies for nir and mir wavelengths," *Journal of Physics D: Applied Physics*, vol. 42, pp. 1–13, June 2009.

[18] R. Crocombe, "Miniature optical spectrometers: The art of the possible, part iv: New near-infrared technologies and spectrometers." http://spectroscopyonline.findanalytichem.com/spectroscopy/, September 2009.

[19] A. R. Korb, P. Dybwad, W. Wadsworth, and J. W. Salisbury, "Portable fourier transform infrared spectroradiometer for field measurements of radiance and emissivity," *Applied Optics*, vol. 35, pp. 1679–1692, April 1996.

[20] K. Yu, D. Lee, U. Krishnamoorthy, N. Park, and O. Solgaard, “Micromachined fourier transform spectrometer on silicon optical bench platform,” *Sensors and Actuators A*, vol. 130-131, pp. 523–530, January 2006.

[21] N. Neumann, M. Ebermann, S. Kurth, and K. Hiller, “Tunable infrared detector with integrated micromachined fabry-perot filter,” *J. Micro/Nanolith. MEMS MOEMS*, vol. 7, April 2008.

[22] Z. Xia, A. A. Eftektar, M. Soltani, B. Momeni, Q. Li, M. Chamanzar, S. Yegnanarayanan, and A. Adibi, “High resolution on-chip spectroscopy based on miniaturized microdonut resonators,” *Optics Express*, vol. 19, pp. 12356–12364, June 2011.

[23] R. F. Wolffenbuttel, “Mems-based optical mini- and microspectrometers for the visible and infrared spectral range,” *Journal Of Micromechanics And Microengineering*, vol. 15, pp. S145–S152, 2005.

[24] T. Kwa and R. Wolffenbuttel, “Integrated grating/detector array fabricated in silicon using micromachining techniques,” *Sensors and Actuators A: Physical*, vol. 31, no. 1-3, pp. 259–266, 1992. Proceedings of Eurosensors V.

[25] T. Kwa, P. Sarro, and R. Wolffenbuttel, “Backside-illuminated silicon photodiode array for an integrated spectrometer,” *IEEE Transactions on Electron Devices*, vol. 44, pp. 761–765, may 1997.

[26] S. Kong, D. Wijngaards, and R. Wolffenbuttel, “Infrared micro-spectrometer based on a diffraction grating,” *Sensors and Actuators A*, vol. 92, pp. 88–95, January 2001.

[27] K. Chaganti, I. Salakhutdinov, I. Avrutsky, and G. W. Auner, “A simple miniature optical spectrometer with a planar waveguide grating coupler in combination with a plano-convex lens,” *Optics Express*, vol. 14, no. 9, pp. 4064–4072, 2006.

[28] G. Lammel, S. Schweizer, and P. Renaud, “Microspectrometer based on a tunable optical filter of porous silicon,” *Sensors and Actuators A: Physical*, vol. 92, no. 1-3, pp. 52–59, 2001.

[29] J. H. Correia, M. Bartek, and R. F. Wolffenbuttel, “Bulk micromachined tunable fabry perot microinterferometer for the visible spectral range,” *Sensors and Actuators A*, vol. 76, pp. 191–196, 1999.

[30] N. Raley, D. Ciarlo, J. Koo, B. Beiriger, J. Trujillo, C. Yu, G. Loomis, and R. Chow, “A fabry-perot microinterferometer for visible wavelengths,” in *Solid-State Sensor and Actuator Workshop, 1992. 5th Technical Digest., IEEE*, pp. 170 – 173, June 1992.

[31] T. Kusserow, *Periodic InP-Air Structures in Optical Devices*. PhD thesis, University of Kassel, 2010.

[32] D. S. Goldman, P. L. White, and N. C. Anheier, "Miniaturized spectrometer employing planar waveguides and grating couplers for chemical analysis," *Applied Optics*, vol. 29, pp. 4583–4589, November 1990.

[33] J. H. Correia, G. de Graaf, S. H. Kong, M. Bartek, and R. F. Wolffenbuttel, "Single-chip cmos optical microspectrometer," *Sensors and Actuators A: Physical*, vol. 82, no. 1-3, pp. 191–197, 2000.

[34] S. W. Wang, C. Xia, X. Chen, , and W. Lu, "Concept of a high-resolution miniature spectrometer using an integrated filter array," *Optics Letters*, vol. 32, no. 6, pp. 632–634, 2007.

[35] S. W. Wang, M. Li, C. Xia, H. Wang, X. Chen, and W. Lu, "128 channels of integrated filter array rapidly fabricated by using the combinatorial deposition technique," *Applied Physics B*, vol. 88, pp. 281–284, 2007.

[36] H. Hillmer, "Verfahren und anordnung zur herstellung von nanoimprintstempeln sowie mikromechanisch abstimmbares filter/detektor-arrays." Patent-Nr. : DE102007047598A1, 2007.

[37] J. F. Mulligan, "Who were fabry and perot?," *Am. Journal Physics*, vol. 66, pp. 797–802, September 1998.

[38] R. Crocombe, "Miniature optical spectrometers: Follow the money part ii: The telecommunications boom." http://spectroscopyonline.findanalytichem.com/spectroscopy/, February 2008.

[39] J. Vaughan, *The Fabry-Perot Interferometer: History, Theory, Practice and Applications*. Adam Higler imprint by IOP Publishing Ltd., 1989.

[40] S. Larouche and L. Martinu, "Openfilters: open-source software for the design, optimization, and synthesis of optical filters," *Applied Optics*, vol. 47, pp. C219–C230, May 2008.

[41] P. Hariharan, *Optical Interferometry*. Academic Press:an imprint of Elsevier Science, 2003.

[42] H. A. Macleod, *Thin-Film Optical Filters*. IOP (Institute of Physics) Publishing, 1986.

[43] S. D. Senturia, *Microsystem Design*. Kluwer Academic Publishers, 2002.

[44] F. Roemer, C. Prott, S. Irmer, J. Daleiden, A. Tarraf, H. Hillmer, and M. Strassner, "Tuning efficiency and linewidth of electrostatically actuated multiple air-gap filters," *Applied Physics Letters*, vol. 82, no. 2, pp. 176–178, 2003.

[45] C. Prott, F. Roemer, E. Ataro, J. Daleiden, S. Irmer, A. Tarraf, and H. Hillmer, "Modeling of ultrawidely tunable vertical cavity air-gap filters and vcsels," *IEEE Journal Of Selected Topics In Quantum Electronics*, vol. 9, pp. 918–928, May/June 2003.

[46] J. Peerlings, A. Dehe, A. Vogt, M. Tilsch, C. Hebeler, F. Langenhan, P. Meissner, and H. Hartnagel, "Long resonator micromachined tunable gaas-alas fabry-perot filter," *Photonics Technology Letters, IEEE*, vol. 9, pp. 1235–1237, sept. 1997.

[47] K. Aratani, P. French, P. Sarro, D. Poenar, R. Wolffenbuttel, and S. Middelhoek, "Surface micromachined tuneable interferometer array," *Sensors and Actuators A*, vol. 43, pp. 17–23, 1994.

[48] A. T. T. D. Tran, Y. H. Lo, Z. H. Zhu, D. Haronian, and E. Mozdy, "Surface micromachined fabry-perot tunable filter," *IEEE Photonics Technology Letters*, vol. 8, no. 3, pp. 393–395, 1996.

[49] C. Mateus, C.-H. Chang, L. Chrostowski, S. Yang, D. Sun, R. Pathak, and C. Chang-Hasnain, "Widely tunable torsional optical filter," *IEEE Photonics Technology Letters*, vol. 14, pp. 819–821, jun 2002.

[50] A. Tarraf, J. Daleiden, F. Romer, C. Prott, V. Rangelov, S. Irmer, E. Ataro, and H. Hillmer, "a novel low-cost tunable dielectric air-gap filter," in *Optical MEMs, 2002. Conference Digest. 2002 IEEE/LEOS International Conference on*, pp. 175 – 176, 2002.

[51] D. Cristea, M. Kusko, C. Tibeica, R. Muller, E. Manea, and D. Syvridis, "Design and experiments for tunable optical sensor fabrication using (1 1 1)-oriented silicon micromachining," *Sensors and Actuators A*, vol. 113, pp. 312–318, 2004.

[52] D. J. Bell, T. J. Lu, N. A. Fleck, and S. M. Spearing, "Mems actuators and sensors: Observations on their performance and selection for purpose," *J. Micromech. Microeng.*, vol. 15, pp. S153–S164, 2005.

[53] J. Daleiden and H. Hillmer, "Multiple air-gap filters and constricted mesa lasers-material processing meets the front of optical device technology," *Applied Physics B*, vol. 76, pp. 821–832, 2003.

[54] F. Grasdepot, H. Alause, W. Knap, J. Malzac, and J. Suski, "Domestic gas sensor with micromachined optical tunable filter," *Sensors and Actuators B*, vol. 35-36, pp. 377–380, 1996.

[55] H. Hillmer, J. Daleiden, C. Prott, S.Irmer, F. Römer, E. Ataro, A. Tarraf, H. Rühling, M. Maniak, and M. Strassner, "Bionics: Precise colour tuning by interference in nature and technology - applications in surface micromachined 1.55 microns vertical air cavity filters," in *SPIE Proc. series Vol. 4983*, vol. 4983, pp. 203–214, 2003.

[56] S. Irmer, *Air-Gap Based Vertical Cavity Micro-Opto-Electro-Mechanical Fabry-Perot Filters*. PhD thesis, University of Kassel, 2005.

[57] S. Irmer, K. Alex, J. Daleiden, I. Kommallein, M. Oliveira, F. Roemer, A. Tarraf, and H. Hillmer, "Surface micromachined optical low-cost all-air-gap filters based

on stress-optimized si3n4 layers," *J. Micromech. Microeng.*, vol. 15, pp. 867–872, 2005.

[58] J. Milne, J. Dell, A. Keating, and L. Faraone, "Widely tunable mems-based fabry perot filter," *Journal of Microelectromechanical Systems*, vol. 18, pp. 905–913, aug. 2009.

[59] E. Pichonat-Gallois, V. Petrini, and M. de Labachelerie, "Design and fabrication of thermal actuators used for a micro-optical bench: Application to a tunable fabry-perot filter," *Sensors and Actuators A*, vol. 114, pp. 260–266, 2004.

[60] M. Strassner, J. Daleiden, N. Chitica, D. Keiper, B. Sta°lnacke, S. Greek, and K. Hjort, "Iii-v semiconductor material for tunable fabry-perot filters for coarse and dense wdm systems," *Sensors and Actuators*, vol. 85, pp. 249–255, 2000.

[61] P. Tayebati, P. D. Wang, D. Vakhshoori, and R. N. Sacks, "Widely tunable fabry-perot filter using ga(al)as - alo deformable mirrors," *IEEE Photonics Technology Letters*, vol. 10, pp. 394–396, March 1998.

[62] P. Tayebati, P. Wang, M. Azimi, L. Maflah, and D. Vakhshoori, "Microelectromechanical tunable filter with stable half symmetric cavity," *Electronics Letters*, vol. 34, pp. 1967–1968, October 1998.

[63] K. Tohda and M. Gratzl, "Micro-miniature autonomous optical sensor array for monitoring ions and metabolites 1: Design, fabrication, and data analysis," *Analytical Sciences*, vol. 22, pp. 383–388, March 2006.

[64] E. Ataro, C. Prott, C. Prott, and H. Hillmer, "Tailored scaling: A possibility to improve the performance of ultra-wide continuously tunable photonic devices," *Applied Physics B*, vol. 79, no. 1, pp. 87–93, 2004.

[65] A. Tarraf, J. Daleiden, S. Irmer, D. Prasai, and H. Hillmer, "Stress investigation of pecvd dielectric layers for advanced optical mems," *J. Micromech. Microeng.*, vol. 14, pp. 317–323, 2004.

[66] Toyo-Gosei, "Nanotechnology division overview." Toyo Gosei Co.Ltd. http://www.toyogosei.co.jp/eng/business/rd.html, 2010.

[67] H. J. Lee, S. Hyun, H. J. Lee, D. G. Choi, D. I. Lee, and E. S. Lee, "Adhesion promoter and anti-sticking layer effects on adhesion properties using symmetric afm probe," *Advanced Materials Research*, vol. 26-28, pp. 1113–1116, 2007.

[68] T. Hirasawa, J. Taniguchi, M. Ohtaguchi, and N. Sakai, "Photo-curable resins and evaluation methods for uv-nanoimprint lithography," *Electronics and Communications in Japan*, vol. 92, no. 11, pp. 174–178, 2009.

[69] M. Fukuhara, H. Ono, T. Hirasawa, M. Otaguchi, N. Sakai, J. Mizuno, and S. Shoji, "Uv nanoimprint lithography and its application for nanodevices," *Journal Of Photopolymer Science And Technology*, vol. 20, no. 4, pp. 549–554, 2007.

[70] A. Matsutani, F. Koyama, and K. Iga, "Microfabrication of dielectric multilayer reflector by reactive ion etching and characterization of induced wafer damage," *Japanese Journal of Applied Physics*, vol. 30, pp. 428–429, 1991.

[71] G. Dang, H. Cho, K. P. Ip, S. J. Pearton, S. N. G. Chu, J. Lopata, W. Hobson, L. M. F. Chirovsky, and F. Rena, "Comparison of dry and wet etch processes for patterning sio2/tio2 distributed bragg reflectors for vertical-cavity surface-emitting lasers," *Journal of The Electrochemical Society*, vol. 148, no. 2, pp. G25–G28, 2001.

[72] O. Powell, D. Sweatman, and H. B. Harrison, "The use of titanium and titanium dioxide as masks for deep silicon etching," *Smart Mater. Struct.*, vol. 15, pp. S81–S86, 2006.

[73] S. Norasetthekul, P. Park, K. Baik, K. Lee, J. Shin, B. Jeong, V. Shishodia, E. Lambers, D. Norton, and S. Pearton, "Dry etch chemistries for tio2 thin films," *Applied Surface Science*, vol. 185, pp. 27–33, 2001.

[74] L. Rolland, M. Peignon, C. Cardinaud, and G. Turban, "Sio2/si selectivity in high density chf3/ch4 plasmas : Role of the fluorocarbon layer," *Microelectronic Engineering*, vol. 53, pp. 375–379, 2000.

[75] H. Hillmer, "Technology of electronic and optoelectronic devices." Script-lecture, 2007.

[76] D. L. Fuller, "Plasma etching." Manuscript -Rochester Institute Of Technology Microelectronic Engineering http://www.microe.rit.edu, April 2010.

[77] K. Williams and R. Muller, "Etch rates for micromachining processing," *Microelectromechanical Systems, Journal of*, vol. 5, pp. 256–269, dec 1996.

[78] M. Köhler, *Etching in Microsystem Technology*. WILEY-VCH Verlag GmbH, 1999.

[79] L. Lallement, A. Rhallabi, C. Cardinaud, M. C. Peignon-Fernandez, and L. L. Alves, "Global model and diagnostic of a low-pressure sf6/ar inductively coupled plasma," *Plasma Sources Science And Technology*, vol. 18 025001, pp. 1–10, 2009.

[80] Clarycon, "Plasma etch mechanism." CLARYCON Plasma technology for advance devices http://www.clarycon.com/, 2003.

[81] B. E. Volland, *Profile Simulations of Gas Chopping Etching Processes: Model Development and Comparison With Experiments*. PhD thesis, University of Kassel, 2004.

[82] M. Quirk and J. Serda, *Semiconductor Manufacturing Technology*. Prentice Hall, 2000.

[83] S. Hicks, S. Murad, I. Sturrock, and C. Wilkinson, "Improving the resistance of pecvd silicon nitride to dry etching using an oxygen plasma," *Microelectronic Engineering*, vol. 35, pp. 41–44, 1997.

[84] A. El amrani, R. Tadjine, and F. Y. Moussa, "Microstructures formation by fluorocarbon barrel plasma etching," *International Journal of Plasma Science and Engineering*, vol. 2008, Article ID 371812, pp. 1–5, 2008.

[85] F. Fracassi and R. d'Agostino, "Chemistry of titanium dry etching in fluorinated and chlorinated gases," *Pure and Applied Chem.*, vol. 64, no. 5, pp. 703–707, 1992.

[86] J. Ji, F. E. H. Tay, J. Miao, and J. Sun, "Characterization of silicon isotropic etch by inductively coupled plasma etcher for microneedle array fabrication," in *Journal of Physics: Conference Series 34*, vol. 34, pp. 1137–1142, International MEMS Conference 2006, Institute of Physics Publishing, 2006.

[87] N. Jin, G. Quancheng, S. Guosheng, and L. Zhongli, "The icp etching technology of 3c-sic films," in *Journal of Physics: Conference Series 34*, pp. 511–515, International MEMS Conference 2006, Institute of Physics Publishing, 2006.

[88] M. Sarfaty, C. Baum, M. Harper, N. Hershkowitz, and J. L. Shohet, "Real-time determination of plasma etch-rate selectivity," *Plasma Sources Sci. Technol.*, vol. 7, pp. 581–589, 1998.

[89] H. Mai, O. Setyawati, V. Daneker, C. Woidt, T. Woit, K. Schultz, S. Schudy, M. Engenhorst, X. Wang, S. Wittzack, F. Köhler, A. Albrecht, M. Bartels, and H. Hillmer, "Verification and calibration of spectral properties of high-resolution nano sensor arrays using microscope spectrometers," in *Technical Digest MOC´10, 16th Microoptics Conference*, pp. MC3 p.22–23, National Chiao Tung University and Microptics Group, Oct-Nov2010 2010.

[90] Zygo, "Newview 5000 - precise, rapid, noncontact 3d surface profiling." Zygo Corporation http://www.lambdaphoto.co.uk/pdfs/nv5000br.pdf, 2001.

[91] R. Blunt, "Wli a production worhty technique for measuring surface roughness on semiconductor wafers," in *CS MANTECH Conference*, 2006.

[92] C. O'Mahony, M. Hill, M. Brunet, R. Duane, and A. Mathewson, "Characterization of micromechanical structures using white-light interferometry," *Meas. Sci. Technol.*, vol. 14, pp. 1807–1814, 2003.

[93] M. Engenhorst, "Mikromechanisch aktuierbare nanophotonische filterarrays, plasmaunterstützte strukturierungstechnologien und charakterisierung-sicherung," Master's thesis, Universität Kassel, 2010.

[94] E. Onate, *Structural Analysis with the Finite Element Method: Linear statics, Vol.1. Basis and solids*. Springer, 2009.

[95] V. Vasu, "Computational analysis on various device designs of tunable optical filters using the finite element method," Master's thesis, University of Kassel, May 2004.

[96] C. Ruttanapun, S. Siridejachai, S. Vannarat, and A. Tuantranont, "Finite element modeling of micromirror," in *9th Annual National Symposium on Computational Science and Engineering (ANSCSE-9)*, pp. 233–239, 2005.

[97] O. Anderson, C. R. Ottermann, R. Kuschnereit, P.Hess, and K. Bange, "Density and young's modulus of thin tio2 films," *Fresenius Journal Anal. Chem.*, vol. 358, pp. 315–318, 1997.

[98] A. Miyamura, K. Kaneda, Y. Sato, and Y. Shigesato, "Effects of internal stress on photocatalytic properties of tio2 films," *Thin Solid Films*, vol. 516, pp. 4603–4608, 2008.

[99] W. Fang and J. A. Wickert, "Determining mean and gradient residual stresses in thin films using micromachined cantilevers," *J. Micromech. Microeng.*, vol. 6, pp. 301–309, 1996.

[100] Comsol-Multiphysics, "Prestressed micromirror," 2008.

[101] C. Schilde, "Untersuchung und optimierung der mechanischen spannung in multischichtsystemen zur herstellung mikromechanisch aktuierbarer optischer filterarrays," Master's thesis, University of Kassel, 2010.

[102] C. Woidt, "Plasmaunterstützte deposition von dielektrischen multischichtstrukturen für fabry-pérot-filterarrays," Master's thesis, Universität Kassel, 2010.

[103] E. Ataro, *Micro-electromechanical Structural Design and Optimization of Vertical Cavity Photonic Devices with Wide Continuous Tuning*. PhD thesis, University of Kassel, 2005.

[104] T. Lill, S. Deshmukh, U. Mitra, K. Collins, T. StDennis, and O. Joubert, "Plasma etching: From fundamental understanding to productive solutions." http://clarycon.com/claryconwhitepap.html.

[105] K. Williams, K. Gupta, and M. Wasilik, "Etch rates for micromachining processing-part ii," *Microelectromechanical Systems, Journal of*, vol. 12, pp. 761–778, dec. 2003.

[106] R. Gunn, C. Welch, D. Stephens, and L. Deng, "Comparison of etch processes for etching sio2 dielectric films," tech. rep., Oxford Instruments Plasma Technology, 2009.

[107] S.-T. Jung, H.-S. Song, D.-S. Kim, and H.-S. Kim, "Inductively coupled plasma etching of sio2 layers for planar lightwave circuits," *Thin Solid Films*, vol. 341, pp. 188–191, 1999.

[108] O. Setyawati, M. Engenhorst, S. Wittzack, F. Köhler, C. Woidt, T. Woit, V. Daneker, M. Bartels, and H. Hillmer, "Dry etching of tio2/sio2 dbr mirrors for tunable optical sensor arrays," in *SPIE Proceedings Photonic West MOEMS-MEMS 2010, ISBN: 9780819479877*, vol. 7591 (Advanced Fabrication Technologies for Micro/Nano Optics and Photonics III), pp. 75910R–(1 – 8), Society of Photo-Optical INstrumentation Engineers (SPIE), SPIE, February 2010.

[109] S. A. Bashar, *Study of Indium Tin Oxide (ITO) for Novel Optoelectronic Devices*. PhD thesis, King's College London, University of London, 1998.

[110] M. Bartels, X. Wang, T. Kusserow, F. Koehler, S. Wittzack, and H. Hillmer, "3d nanoimprint templates with ultra high vertical precision," in *ICMAT 2009 and IUMRS-ICA 2009*, vol. Symposium K, pp. A01859–03214, 2009.

[111] microresist-technology GmbH, "Uv haertende polymere fuer die uv gestuetzte nanoimprint lithographie." http://www.microresist.de/produkte/, 2009.

[112] S. Timoshenko and S. Woinowsky-Krieger, *Theory Of Plates And Shells*. McGraw-Hill, Inc., 1959.

[113] Micro-Chemicals-GmbH, "Lithography: Theory and application of photoresists, developers, solvents and etchants," 2008/2009.

List of Figures

2.1 *A grating-based integrated spectrometer with photodiode array fabricated in silicon [24] .* 6

2.2 *The scheme of an IR grating-based microspectrometer with two wafer approach [26].* 6

2.3 *A monolithic 'slab-waveguide' spectrometer manufactured by LIGA process, courtesy of* Boehringer Ingelheim microParts [18] *(later* INSION*).* 8

2.4 *Illustration of the grating-based spectrometer produced by* Carl-Zeiss. *The increase in the number of grating slits influences the resolution.* 8

2.5 *The filter array-type spectrometer where 4x4 FP-etalon were integrated into a single-chip CMOS. Different thicknesses of* SiO_2 *layer (as the filter cavities) tune the passed wavelengths [33].* 10

2.6 *The deposition process to fabricate the filter arrays with different cavities.* SiO_2 *film was used as cavity material and deposited by 9 steps [34].* 10

3.1 *Multiple reflection of plane waves between two plane P1 and P2 parallel surfaces. The amplitude coefficients of the reflected set of beams denote as a, b, c and the transmitted beams as* α, β, γ *[39].* 14

3.2 *Open-Filter's simulation results of the transmission linewidths. By increasing the length of cavity, the FSR will decrease.* 17

3.3 *Transmission of two type DBRs-based filters, simulated by OpenFilter, with the central wavelengths at 650 nm.* TiO_2/SiO_2 *DBRs-based filter exhibits broader bandwidth with fewer pairs of DBRs, due to the higher index contrast compared to* Si_3N_4/SiO_2 *DBRs-based filter.* 17

3.4 *Graph of the normalized gap as a function of normalized voltage to show the stable and unstable displacements for the electrostatic actuator [43].* 20

3.5 *Schematic sideview of the filter during electrostatic actuation, the top DBRs are moved towards the bottom ones. The actuation changes the cavity layer of the filter by applying bias voltage, and a different wavelength passes through (top). Illustration for expressing a tuning efficiency* η_t *of 0.6, simulated by OpenFilter (bottom).* 20

3.6 *Scheme of typical anisotropic and isotropic etch.* 24

3.7 *Scheme for determination of the material thicknesses to calculate the etch rate and etch selectivity.* 24

3.8 *Several processes in plasma etch (redraw after [80]). (1) Chemical etch; (2) Ion enhanced etch; (3) Physical etch; (4) Trenching; (5) Sidewall pasivation; (6) Mask erosion.* 25
3.9 *Scheme of a typical paralel-plate CCP-RIE reactor (redraw after [78, 82]).* 27
3.10 *Scheme of an ICP-RIE plant [81].* 27
3.11 *Microscope-spectrometer: system set-up for optical properties measurement (redraw after [89]).* 29
3.12 *A scheme of the WLI Zygo NewView 5000 [90].* 29

4.1 *Overview of the filter fabrication process.* 32
4.2 *Simulation of the filters with different pairs of Si_3N_4/SiO_2 DBRs (top). Measurement results of the 23.5 and 9.5 pairs of DBRs-based filters, where the mr-UVCur06 was used as the cavity layer material (bottom).* 33
4.3 *Measured transmission bandwidths of 5.5 pairs of TiO_2/SiO_2 DBRs and 9.5 pairs of Si_3N_4/SiO_2 DBRs. Since TiO_2/SiO_2 has higher index contrast, only few number of pairs of DBRs are required to obtain broader bandwidth, and higher reflectivity.* 34
4.4 *A micrograph of one filter element (left) and its cross section (right). The filter was formed by top and bottom DBRs with air gap as the resonance cavity.* 34
4.5 *Microscope images of the filter arrays, where each filter membrane has three bent suspensions, and the post structures connected together. These three filters can be actuated simultaneously (left). Separated actuation (right) for each filter can be made also for these designs.* 35
4.6 *An Illustration of filter arrays with three stopbands arranged in series, hence, a broad tuning range can be achieved.* 35
4.7 *Three mesa filter structures with three suspensions which have different geometric shapes: straight (left), bent (middle) and curl-bent (right) suspensions.* 37
4.8 *The displacement at z-axis by applying the stress; the graph was depicted by cross-section post-processing step performed in FEMLAB. The x-axis represented the diameter of the filter membrane. The legend shows the increment of stress [Pa] induced in the Si_3N_4/SiO_2 layers.* 39
4.9 *Graph mirror displacement as a function of Si_3N_4/SiO_2 membrane diameter, with stress of 0.1 GPa, for the structures with two suspensions: straight, bent and curl-bent.* 40
4.10 *Graph of mirror displacements as a function of Si_3N_4/SiO_2 membrane diameter with stress of -0.1 GPa, for the structures with three and four straight suspensions. The longer the suspensions or the bigger the membrane area, the membrane bends more.* 40
4.11 *Graph of mirror displacement as a function of membrane diameter, for the structures with three bent and curl-bent suspensions (top). Displacement profiles of the structures with three suspensions, where the x-axis represents the cross section of the membrane (bottom). The membranes are made of multilayers of Si_3N_4/SiO_2, and both have diameter of 30 μm. The filter with bent suspensions led to higher membrane displacement than the one with curl-bent suspensions.* . . 42

4.12 *Displacement profiles of the filter membranes, made of TiO_2/SiO_2, with four suspensions. The x-axis represents the cross section of the membrane. The type of suspensions differs the displacement magnitude; the filter (membrane d=30 μm) with straight suspensions bent more than the one (membrane d=25 μm) with curl-bent suspensions.* 43
4.13 *Post-processing image of the structure with four curl-bent suspensions, the line shown on the membrane represents the cross section in x-axis plotted in Fig.* 4.12*, that is the membrane diameter.* 43
4.14 *Comparing the displacement of the mirrors (Si_3N_4/SiO_2 and TiO_2/SiO_2) as a function of membrane diameter. The applied stress of -1 GPa is given for the structures with three and four suspensions.* 44

5.1 *Etch rates and selectivities of Si_3N_4/SiO_2 as a function of SF_6 flow rate (left). Etch experiments were performed in the CCP-RIE (redraw after [102]).* 46
5.2 *Etch rates and selectivities of Si_3N_4/SiO_2 as a function of the etch time, with and without applying the SF_6 gas. Etch experiments were performed in the CCP-RIE.* 47
5.3 *SEM graphs show the etch profile of the 9.5 pairs top DBRs (approximately 1.85 μm in thickness) after lateral structuring in the CCP-RIE, the mask was removed (left), the close up of the structure sidewall (right). Etch condition: $Ar/CHF_3/SF_6$: 5.1/3/2 sccm, 50W of RF power, 18.75 mTorr at 12.5°C; etch time was 68 min.* 47
5.4 *SEM graphs of etch profile mirror, with Al mask. Etching without the CHF_3 flow rate, in an etch condition of SF_6/Ar=10/15 sccm, 500W ICP/300W RF, 10 mTorr and 20°C for 10 min. Al mask exhibited grassy surface (left). The structure result after process in an etch condition of $CHF_3/Ar/SF_6$=10/40/5 sccm, 750W ICP/175W RF power, 10 mTorr and 20°C for 10 min (right).* 48
5.5 *SEM graphs of etch profile mirror, with the photoresist etch mask still on the mirror (left), after process with oxigen the photoresist was removed (right). Etch condition in the ICP: $CHF_3/Ar/SF_6$=10/40/5 sccm, 100W ICP/175W RF, 10 mTorr, 20°C, 10min.* 49
5.6 *Etch rates and selectivities as a function of the varied process pressure. Increasing the pressure decreased both etch rates and selectivities. Etch experiments were performed with AZ1518 photoresist masks in the ICP using RIE-mode.* . . 50
5.7 *Etch rates and selectivities as a function of process pressure. Increasing SF_6 flow rate increased the etch rates. Etch experiments were performed with AZnLoF2070 5:1 photoresist mask in the ICP using RIE-mode.* 50
5.8 *SEM graphs of the etched mirrors. The AZ1518 mask was used (1a and 1b) in the process, resulted in an etch rate of 30 nm/min and selectivity of 1.9; the etch time was 25 min. The AZ1505 mask was used (2a and 2b) in the process, resulted in an etch rate of 40 nm/min and selectivity of 2; the etch time was 15 min. The etch condition was $Ar/CHF_3/SF_6$ of 5.1/3/2 sccm at 19 mTorr, 20°C, and 250 W of RF power.* 51
5.9 *Spectral transmission of the filters, with mr-UVCur06 and mr-UVCur21 as the cavity layers. Measurement were taken before underetching process.* 53

5.10 *Spin curve of PAK-01 polymers; represents undiluted PAK-01 [courtesy of Toyo-Gosei] and diluted PAK-01 (4:1 with ether). The measurement was taken after softbake and subsequent exposure. Higher spin speeds lead to thinner polymer layers.* 54
5.11 *Coating process of PAK-01 polymer, the surface looked homogeneous with adhesion promoter TI-Prime (left), and with mr-APS1 (right) where the inhomogeneity of the surface showed different colors.* 54
5.12 *Spectral transmission of the filter with 9.5 pairs of Si_3N_4/SiO_2 DBRs and PAK-01 diluted 4:1 as the cavity layer (spin speed at 3950 rpm).* 55
5.13 *SEM micrographs of the star-structure for varied underetching time. (a) The polymer was treated without nitrogen during the exposure, the structure was not completely released for 170 min. (b) Nitrogen was applied during the UV-exposure, the structure was released in only 15 min underetching time.* 55
5.14 *An image (taken by Leica microscope) of the cantilever structure for estimating the underetch rate. The image shows the result after underetching of PAK-01 diluted 4:1 for 10 min, cantilever with width of 10 μm was completely released.* . . 57
5.15 *Images were taken by Leica microscope of the star structure (diameter 50 μm, the cantilever 65 μmx10 μm) was taken from two samples (9.5 pairs of top and bottom DBRs with PAK-01 4:1 as cavity), after underetching for 10 min (a), and underetching for 20 min (b).* 57
5.16 *SEM graphs of the filter membrane that was released after the underetch process for 15 min. The sample has ITO top electrodes which was deposited after the underetch process.* 58
5.17 *Simulation OpenFilter on different thicknesses of ITO as electrodes for the filter, which uses Si_3N_4/SiO_2 DBRs and mr-UVCur06 cavity material. Thicker film of ITO reduced the optical tranparency. Film thickness of 20, 50 and 90 nm are simulated using ITO material data with refractive index* n = *1.88. Close-up image of filter linewidth is shown (bottom). 83 nm is an optimized thickness of ITO that fits to a quarter-wavelength, with refractive index of approximately 2.* . . 59
5.18 *Spectral transmission of one filter element, during the electrostatic actuation. Filter tuning range was approximately 75 nm, with FWHM of less than 4 nm.* . . . 61
5.19 *Mechanical properties of the filters: membrane displacement as a function of tuning voltage (redraw after [93]). Measurements were taken for the membrane with diameter of 25 μm (left), and membrane with diameter of 10 μm (right).* . . . 61
5.20 *The tuning spectral range of the filter arrays, consisted of three filters a, b and c. The filter structure is shown in (inset).* 62
5.21 *Spectral transmission of one of the filter array during the electrostatic actuation. The tuning range was approximately 70 nm.* 63
5.22 *Spectral transmission of the filter-*b *and filter-*c *in one array structure (the structure in Fig.*5.20*-inset) during the electrostatic actuation. The transmission peak at 0 V was shifted due to the electrostatic charge.* 63
5.23 *Filter linewidth of a sample (9.5 pairs of DBRs and mr-UVCur06 cavity) after lateral structuring of the top DBRs, before the underetching process.* 64

5.24 *Spectral transmission of one of the filter arrays as a function of actuation voltage, with tuning range of approximately 55 nm for the actuation between 0 V to 22 V. The membrane had a diameter of 30 μm and three bent suspensions with width of 10 μm.* 64
5.25 *Mechanical properties of the filter arrays: Membrane displacement of approximately 120 nm was observed for the actuation voltage between 0 V to 20 V, where the third-step measured data was captured (top), the first-step measured data showed a hysteresis curve and the filter geometry that was characterized (bottom). The measurement was performed using the WLI [measured by M. Mondragon-Marquez], and analyzing the displacement of filters could be accomplished simultaneously* 65

6.1 *SEM graphs show the mirror after the etching process, using Al mask (left), and Cr mask (right).* 68
6.2 *Etch rates and selectivities as a function of varied SF_6, at fixed 20 sccm of Ar gas. ITO etch masks were used. Circles represent the selectivity, rectangles represent the etch rate.* 70
6.3 *Etch rates and selectivities as a function of varied Ar, at fixed 10 sccm of SF_6 gas. ITO etch masks were used. Circles represent the selectivity, rectangles represent the etch rate.* 70
6.4 *SEM micrographs of the etched mirror at etch condition of 500 W ICP/300 W RF, 20°C, a pressure of 10 mTorr.* 71
6.5 *SEM micrographs of the etched mirror with the etch condition: Ar/SF_6: 20/10 sccm, 20°C, a pressure of 10 mTorr.* 71
6.6 *Etch rates and selectivities as a function of RF power, at fixed 500 W ICP power. Etch condition: Ar/SF_6=20/10 sccm, 20°C, 10 mTorr. ITO etch masks were used. Circles represent the selectivity, rectangles represent the etch rate, and triangles represent the dc bias.* 72
6.7 *Etch rates and selectivities as a function of ICP power at a fixed 300 W RF power. Etch condition: Ar/SF_6=20/10 sccm, 20°C, 10 mTorr. ITO etch masks were used. Circles represent the selectivity, rectangles represent the etch rate, and triangles represent the dc bias.* 72
6.8 *Etch rates and selectivities as a function of the process pressure. Etch conditions: 500 W ICP/300 W RF, Ar/SF_6:20/10 sccm. ITO etch masks were used. Circles represent the selectivity, rectangles represent the etch rate.* 74
6.9 *Etch rates and selectivities as a function of the temperature. Etch conditions: 500 W ICP/300 W RF, Ar/SF_6:20/10 sccm. ITO etch masks were used. Circles represent the selectivity, rectangles represent the etch rate.* 74
6.10 *SEM micrographs show the etched mirrors. Etch conditions: Ar/SF_6: 20/10 sccm, 500 W ICP/300 W RF, 6 mTorr (a) at -30°C, an etch rate of approximately 70 nm/min was obtained; residue was observed on the sidewall, this effect can be eliminated by applying higher temperature; (b) at 20°C, an etch rate of 80 nm/min was obtained, and (c) at 40°C, an etch rate of approximately 90 nm/min was obtained. ITO etch masks were used.* 75

6.11 *Etch rates of TiO_2 film in the CCP-RIE, as a function of varied SF_6 flow rate. Etch condition: Ar flow rate of 4 sccm, 50 W RF power, 18.75 mTorr.* 76
6.12 *Etch rates of SiO_2 film in the CCP-RIE, as a function of varied SF_6 flow rate. Etch condition: Ar flow rate of 4 sccm, 50 W RF power, 18.75 mTorr.* 76
6.13 *SEM micrographs of TiO_2/SiO_2 DBRs after etching in the CCP-RIE for 40 min; the filter membrane with four suspensions (left). Step-like structure of etched edges was observed, due to the rounding sidewall of the photoresist mask (right).* 76
6.14 *The etch behaviour of TiO_2/SiO_2 in ICP-RIE, using positive AZ1518 photoresist as etch mask, at process pressure of 6 mTorr (left) and 10 mTorr (right).* 78
6.15 *The etch behaviour of TiO_2/SiO_2 in ICP-RIE, using negative photoresist, AZnLoF2070 5:1, as etch mask, at process pressure of 6 mTorr (left) and 10 mTorr (right).* . . 78
6.16 *SEM graphs of the etched profile of the mirrors, which were etched using the AZnLoF2070 5:1 mask (left), and using the AZ1518 mask (right). Etch condition: 500 W ICP/160 W RF power, Ar/SF_6=10/10 sccm, pressure of 6 mTorr, at 20°C; the etch time was 5 min. The pictures were taken after removing of the etch mask.* 79
6.17 *An SEM image shows the sidewall of the mirror after etching for 10 min under AZnLoF2070 5:1 mask. A WLI image (right) depicts the filter structure with four suspensions; Ra (average roughness) of the structure measured by the WLI was approximately ≤10 nm.* 80
6.18 *Surface profile of the filters; images were taken by Leica microscope on the sample, after sputtering of the DBRs on the diluted PAK-01 (a), and on the mr-UVCur06 (b).* 80
6.19 *Images were taken by Leica microscope of the sample filter before dry etching process, where mr-UVCur21 polymer coated without the mr-APS1 (a), and the sample filter after dry etching, where the polymer used the adhesion promoter mr-APS1 in the coating process (b).* 82
6.20 *Image of filter array (mr-UVCur06 cavity layer) was taken by Leica microscope, after lateral structuring of the top DBRs in the CCP-RIE, with AZ1518 photoresist etch mask.* 82
6.21 *The optical properties of 5.5 pairs of TiO_2/SiO_2 bottom DBRs, with central wavelength 550 nm.* 83
6.22 *The optical properties of TiO_2/SiO_2 DBRs-based filter, with mr-UVCur06 as the cavity material, measured after removing of the etch mask.* 83
6.23 *WLI image of released filter arrays, the displacement of membrane was nearly 10 μm after the underetching process. The measured profile showed that the height of membrane in the vertical (y) direction was 9777.59 nm.* 84
6.24 *The filter membranes that were released after the underetching process for 18 min: the filter with four-straight suspensions (top), and four-curl bent suspensions (bottom) which displaced less (approximately a half of the displacement of the filter whose straight suspensions).* 86
6.25 *Transmission peak of the filter, measured by a micropcope spectrometer after underetching process.* 87

B.1 *Three photomasks MZT TOSA 2009: Mesa MZT TOSA 2009(a), Light protection MZT TOSA 2009 (b) and Protection layer MZT TOSA 2009 (c).* 125
B.2 *Two photomasks MAZET 2010: Mesa MAZET mask for patterning the mesa (a), and top electrode mask for patterning the top electrodes (b). Zoom-in image of the filter arrays-a in Block A (field-1F) (c).* 126
B.3 *Polymer film thickness as a function of spin speed, at 60s spin time, after coating and softbake: mr-UVCur06 (left) and mr-UVCur21 (right); the mr-UVCur21-300nm was used in this work [courtesy of micro-resist-tech. GmbH [111]].* 126

List of Tables

3.1 Technical data of mr-UVCur06 and mr-UVCur21 [courtesy of *micro-resist-technology GmbH*], and PAK-01 [courtesy of *Toyo-Gosei Co.,Ltd*] 23

4.1 Parameters of the DBRs used in the model I: Si_3N_4, SiO_2 and the bulk equivalent material (of 9.5 pairs of Si_3N_4/SiO_2). 38
4.2 Parameters of the DBRs used in the model II: TiO_2, SiO_2, and the bulk equivalent material (of 5.5 pairs of TiO_2/SiO_2 DBRs). 38

5.1 Etch experiments for structuring of Si_3N_4, SiO_2, and the DBRs. 46
5.2 Etching process in the ICP for structuring of the Si_3N_4/SiO_2 DBRs. 48
5.3 Etch experiments for structuring of the Si_3N_4/SiO_2 DBRs. 52

6.1 Etch experiments for structuring of the TiO_2/SiO_2 DBRs in ICP-RIE: variation of gas flow rate. 69
6.2 Etch experiments for structuring of the TiO_2/SiO_2 DBRs in ICP-RIE: variation applied power. 71
6.3 Etch experiments for structuring of the TiO_2/SiO_2 DBRs in ICP-RIE: variation pressure and temperature. 73
6.4 Etch experiments for structuring of TiO_2, SiO_2, and the DBRs in the CCP-RIE. . 75
6.5 Etch experiments for structuring of the TiO_2/SiO_2 DBRs in ICP-RIE: photoresist masks. 77

B.1 Optical lithography of the photoresist I 119
B.2 Optical lithography of the photoresist II 120
B.3 Deposition by PECVD 120
B.4 Deposition by IBSD 121
B.5 Spin coating process of the mr-UVCur06 polymer 122
B.6 Spin coating process of the mr-UVCur21 and PAK-01 polymers 122
B.7 Tabular form of the exponential model regarding the PAK-01 polymer thickness curve 123
B.8 Tabular form of the exponential model regarding the PAK-01 (diluted 4:1) polymer thickness curve 123
B.9 Product information of the PAK-01 diluter (ethylen-glycol-monomethylether) 124

Acknowledgements

I would like to thank Prof. Dr. Hartmut Hillmer for the opportunity to finish this research work at INA. His support, guidance and encouragement from the beginning to the final level, motivated and enabled me to develop an understanding of the subject. I also thank Prof. Dr.-Ing. Josef Börcsök for evaluating and co-supervising my thesis, and the other examiners Prof. Dr.-Ing. Axel Bangert and Prof. Dr.-Ing. Peter Lehmann.

I am indebted to many of my colleagues, for their precious help in completing the work and encouraging me through valuable discussion: Mr. Zamora, Mr. Viereck, Mr. Messow, Mrs. Schultz and all members of the Nanospectrometer Group. Mr. Woidt and Mr. Engenhorst for their outstanding assistance in supplying the fast-and-invaluable information related to the research subject.

I wish to warmly thank everyone at INA, especially to Mr. Gutermuth, Mr. Kusserow, Mr. Daneker, Mr. Bartels, Mr. Jäkel, Mr. Wittzack, Mr. Köhler, Mrs. Kommallein, Mrs. Wensch, Mr. Briggs, Mr. Schnabel and Mrs. Rippien for their supportive working environment.
I would like to show my gratitude to Mr. Köcher and Mr. Sandhagen from the Opsolution Nanophotonics GmbH, and to acknowledge the financial support of the BMBF project "Tunable Optical Sensor-Arrays"(2008 to 2011).
Last but not least, I am very grateful to my family and my friends for their endless support over the years and during the completion of the report.

Appendix A

Plate theory, elastic energy and virtual work principle

The model in this simulation (Chapter 4) uses 3D structural analysis. To obtain solutions for this numerical model, the concept of plate theory will be introduced. **Plate theory** appears to handle plate-liked structures to obtain an approach for reducing 3D elastic theory problems to 2D [112][Mindlin]. Plate-liked structure means that the thickness of the structure is extremely thin compared to the other dimensions.
There are three theories related to the deflection of the plate, i.e. the thin plate that has small deflection, the thin plate with large deflection and the thick plate. If the plate remains neutral, that is no deformation in the middle of the plane plate during bending, or the effect of the shear force can be disregarded, hence, the plate is categorized as the first one. Thin plate with large deflection considers not only immovable edges (or clamped beams) but also edges which are free-to-move in the plane of the plate (or membranes) [112]. In this case, the structure will be handled as nonlinear elastic elements, where the stiffness increases as the given load is increased. Some approximations based on energy considerations emerge to evaluate this subject [43].

First we recall the **elastic energy** that was described as scalar efforts and displacements of a lumped element. The energy that is stored at displacement value q_1 can be defined as:

$$W(q_1) = \int_0^{q_1} e(q)dq \tag{A.1}$$

where *q* is a scalar displacement and *e* is a scalar effort.
In a distributed system, the energy density $\widetilde{W}$(x,y,z) determines the total energy *W* that stored in small elements $\Delta x \Delta y \Delta z$ as:

$$W_{\Delta x,\Delta y,\Delta z} = \widetilde{W}(x,y,z)\Delta x \Delta y \Delta z \tag{A.2}$$

This energy density concept is generally utilized by the systems that store potential energy. In a lumped element, stored energy is determined by integral of an effort over a displacement. Since stress has a dimension of N/m^2 and strain is dimensionless, and the stress-strain product leads to energy per unit volume, which is equal to the dimension of

the energy density. And in the elastic domain, stress and strain are a generalized effort and displacement, respectively, hence, strain energy density can be defined as:

$$\widetilde{W}(x,y,z) = \int_0^{\epsilon(x,y,z)} \sigma(\epsilon) d\epsilon \tag{A.3}$$

$\sigma(\epsilon)$ is a function that relates stress to strain, and ϵ*(x,y,z)* is a value of the strain at *(x,y,z)*. Total strain energy for the volume of a deformed body structure then can be obtained by solving the following integral [43]:

$$W = \frac{1}{2} \int\int\int (\sigma_x \epsilon_x + \sigma_y \epsilon_y + \sigma_z \epsilon_z + \tau_{yz}\gamma_{yz} + \tau_{zx}\gamma_{zx} + \tau_{xy}\gamma_{xy}) dxdydz \tag{A.4}$$

In the structural analysis FEM theory uses **virtual work principle** approach to solve the **displacement** formulation. This approach will be elaborated here. The virtual work principle states that if a structure is subjected to external forces and due to those forces it deforms and displaces, thus, in equilibrium the total work performed by the forces must equal the stored energy in the deformed and displaced state. In this principle, kinetic energy is not considered since solely quasi-static deformations and displacements that are counted. Therefore, the functions concerning the solution for the deformation or displacement of the structure can be varied, where the quantity *U* in the following should be minimum [43]:

$$U = stored\, energy - work\; done \tag{A.5}$$

Consider δ*u(x,y,z)*,δ*v(x,y,z)* and δ*w(x,y,z)* are component vectors of virtual displacements of a body structure, and the associated virtual strain are described as

$$\delta\epsilon_x = \frac{\partial}{\partial_x}\delta u \;\; ; \;\; \delta\epsilon_y = \frac{\partial}{\partial_y}\delta v \;\; ; \;\; \delta\epsilon_z = \frac{\partial}{\partial_z}\delta w$$

$$\delta\gamma_{xy} = \frac{1}{2}(\frac{\partial}{\partial_x}\delta v + \frac{\partial}{\partial_y}\delta u) \; ; \; \delta\gamma_{yz} = \frac{1}{2}(\frac{\partial}{\partial_y}\delta w + \frac{\partial}{\partial_z}\delta v) \; ; \; \delta\gamma_{xz} = \frac{1}{2}(\frac{\partial}{\partial_x}\delta w + \frac{\partial}{\partial_z}\delta u) \tag{A.6a}$$

hence, the strain energy density becomes:

$$\delta\widetilde{W} = \sigma_x\delta\epsilon_x + \sigma_y\delta\epsilon_y + \sigma_z\delta\epsilon_z + \tau_{yz}\delta\gamma_{yz} + \tau_{zx}\delta\gamma_{zx} + \tau_{xy}\delta\gamma_{xy} \tag{A.7}$$

According to the aforementioned principle, the quantity *U* must at minimum, thus we have:

$$\int_{volume} \delta\widetilde{W}\; dxdydz - \int_{surface} (F_{s,x}\delta u + F_{s,y}\delta v + F_{s,z}\delta w) dS$$
$$- \int_{volume} F_{b,x}\delta u + F_{b,y}\delta v + F_{b,z}\delta w)\; dxdydz = 0 \tag{A.8a}$$

The total strain energy is the first integral. The negative of total work done by surface forces and body forces are defined in the second and the third integral, respectively. And

the potential energy of the system *U* is defined as:

$$U = \int_{volume} \widetilde{W} dxdydz - \int_{surface} (F_{s,x}u + F_{s,y}v + F_{s,z}w)dS - \int_{volume} F_{b,x}u + F_{b,y}v + F_{b,z}w)dxdydz \quad \text{(A.9a)}$$

For three-dimensions problem, energy density in **plates** and **membranes** can be obtained in term of stress components:

$$\widetilde{W} = \frac{1}{2E}(\sigma_x^2 + \sigma_y^2 + \sigma_z^2) - \frac{\nu}{E}(\sigma_x\sigma_y + \sigma_y\sigma_z + \sigma_x\sigma_z) + \frac{1}{2G}(\tau_{xy}^2 + \tau_{yz}^2 + \tau_{xz}^2) \quad \text{(A.10)}$$

where E is known as Young's Modulus, *v* is Poisson ratio, and *G* is the shear modulus which defined as:

$$G = \frac{E}{2(1+\nu)} \quad \text{(A.11)}$$

At the state of plane stress where σ_z, τ_{yz} and τ_{xz} are zero, the energy density becomes:

$$\widetilde{W} = \frac{1}{2E}(\sigma_x^2 + \sigma_y^2) - \frac{\nu}{E}(\sigma_x\sigma_y) + \frac{1}{2G}(\tau_{xy}^2) \quad \text{(A.12)}$$

This equation can be written in term of strains component:

$$\widetilde{W} = \frac{E}{2(1-\nu^2)}(\epsilon_x^2 + \epsilon_y^2 + 2\nu\epsilon_x\epsilon_y) + \frac{G}{2}\gamma_{xy}^2 \quad \text{(A.13)}$$

Using approximations to apply the principle of virtual work, for instance in the displacement fields, will be explained in the following, in so called variational methods. We define now trial displacement functions $\hat{u}$ =(*x, y, z;* c_1, c_2,...c_n), $\hat{v}$ =(*x, y, z;* c_1, c_2,...c_n) and $\hat{w}$ =(*x, y, z;* c_1, c_2,...c_n), where c_1, c_2,...c_n are set of *n* parameters in the trial functions. To obtain potential energy of the system, the equation $A.9a$ can be used, and since *U* must be stationary with respect to any virtual displacement, thus we can obtain

$$\frac{\partial U}{\partial c_j} = 0 \quad \text{(A.14)}$$

for every c_j, which will take us to a set of *n* equations:

$$\frac{\partial U}{\partial c_1} = 0 ...... \frac{\partial U}{\partial c_n} = 0 \quad \text{(A.15)}$$

Solutions for those equations lead to *n* values of c_j that yield to a minimum potential energy. The aforementioned analysis has an important key in **finite-element** numerical modeling, wherein the variational parameters implies the nodal displacements of mesh elements in the structural analysis.

Appendix B

Technological processes regarding the fabrication

This part presents technological process steps involved in the fabrication of the filters. Optical lithography of the photoresists is given in in tabular form in the next section, followed by the spin coating process of the polymers. The product information regarding the diluter for PAK-01 polymer and the exponential model data for the PAK-01 polymer curve are also presented. Etch conditions for structuring of the DBRs are summarized in the last section.

B.1 Lithography of the photoresists

The following table (Tabel $B.1$ and Tabel $B.2$) presents the steps of optical lithography for patterning the utilized photoresists in the filters fabrication process [113].

Table B.1: Optical lithography of the photoresist I

Photoresist	Process flow
AZ1518	preparation: Bake the sample (glass with ITO film) on hotplate 120°C ca.10min
	Coating TI-Prime (4000rpm)
	Coating AZ1518 (4000rpm)
	Bake on hotplate 90°C 5min
	Exposure UV light ca.3min *
	Exposure with MA4 (with photomask) 6.6s +
	Development in 0.8%KOH 30-40s
	Bake 120°C ≥30min *
	Bake 120°C 3-5min +
* for the corner of the sample,thus lift-off bottom DBRs can be done +for patterning the mesa or top electrode	

Table B.2: Optical lithography of the photoresist II

Photoresist	Process flow
AZnLoF2070 5:1	preparation:Bake the sample on hotplate 110°C ca.10min Coating TI-Prime P18 (500rpm 2s+3000rpm 40s) Coating AZnLoF2070 5:1 P18 (500rpm 2s+3000rpm 40s) Bake on hotplate 100°C 11min Exposure with MA4 (with photomask) 14.5s Bake on hotplate 110°C 1min Development in AZ-826 120s Hardbake on hotplate 120°C 3min
AZ1505	preparation:Bake the sample on hotplate 120°C ca.10min Coating TI-Prime (4000rpm) Coating AZ1505 (4000rpm) Bake on hotplate 90°C 5min Exposure with MA4 (with photomask) 4.5s Development in 0.8%KOH 10-15s Hardbake 120°C ca.5min

B.2 Film deposition

The following tabel, Tabel $B.3$ and $B.4$, show the parameters used in the deposition of thin films by PECVD and IBSD, respectively.

Table B.3: Deposition by PECVD

Layer	Gases (sccm)	Power (W)	Pressure	Temperature
Si_3N_4	SiH_4:1000/NH_3:20	HF 20/LF 20	0.65 Torr	120°
SiO_2	SiH_4:430/N_2O:10	HF 20/LF -	1 Torr	120°

B.3 Photomasks for the fabrication

For the first design, where the experiments dealed with one element of filter, IMA3 mask was used. In the second design, the filter arrays fabrication used MZT TOSA masks, 2009 and 2010, for patterning the mesa and top electrodes. Also a protection layer mask (2009) was available for some experiments regarding the protection layer. Fig. $B.1$ shows few structures plotted in Block H of each mask (2009).

Light protection MZT TOSA 2009 mask, combined with Mesa MZT TOSA, was used for patterning the top electrodes layer. Since this layer was made of reflective material (Al), hence, a circle in the middle of membrane was required to open the center of filter

Table B.4: Deposition by IBSD

Layer	Process parameters
ITO	Po25/Ro60/Ti45; MW 190W Beam voltage/current: 1000 V/50mA Accelerator voltage/current: 100V/2.5mA Ar 3sccm/O_2 9sccm Pulsing condition:40%/1kHz (ions-ground) without electron-current
TiO_2	Po25/Ro60/Ti45 Beam voltage/current: 800 V/75mA Accelerator voltage/current: 100V/2.6mA Pulsing condition:70%/1kHz (ions-ground) without electron-current ISQ1: Ar 4sccm; MW 203W/ISQ2: Ar 6sccm O_2 3sccm; MW 200W
SiO_2	Po25/Ro60/Ti45 Beam voltage/current: 800 V/50mA Accelerator voltage/current: 100V/1.2mA Pulsing condition:70%/1kHz (ions-ground) without electron-current ISQ1: Ar 4sccm; MW 203W/ISQ2: Ar 6sccm O_2 4.5sccm; MW 200W

Po25:position 25°,Ro60:rotation 60°,Ti45:tilting 45°

membrane area for the optical properties characterization. This light protection layer mask, can be utilized for defining reflective structures around the mesa, that is necessary to avoid unwanted signals that might captured during characterization of the filters.

For the third design, where the three stopband arranged in series for implementation of broad filter bandwitdh, new masks were required, particularly for bonding, stopbands and defining membranes. To obtain efficient patterning of top electrodes a new top electrode photomask was introduced. Fig. $B.2$ shows some structures in the two photomasks that are located in Block A.

B.4 Material and coating process concerning the UV-NIL polymers

The spin curves of mr-UVCur06 and mr-UVCur21, which are produced by micro resist technology GmbH, are shown in Fig. $B.3$.
The line at 3000 rpm corresponds to mr-UVCur06 polymer thickness of 258nm, and mr-UVCur21 thickness of 300nm. In this work mrUVCur21-300nm was used.

B.4.1 The coating process of the polymers

Tabel $B.5$ and Tabel $B.6$ summarizes the detail process regarding spin coating of the polymers, as the cavity layer.

Table B.5: Spin coating process of the mr-UVCur06 polymer

Material	Process flow
Preparation	Bake the sample on hotplate 150°C ca.30min
mr-APS1	Coating at speed 5000rpm 60s (P2)
	Bake on hotplate 150°C 60s
mr-UVCur06	Coating at speed 3000rpm 60s (t=258nm according to the manufacturer)
	Bake on hotplate 80°C 60s
	UV exposure 5min - N_2 ambient

Table B.6: Spin coating process of the mr-UVCur21 and PAK-01 polymers

Material	Process flow
Preparation	Bake the sample on hotplate 150°C ca.30min
mr-APS1	Coating at 5000rpm 60s (P2)
	Bake on hotplate 150°C 60s
mr-UVCur21	Coating at speed 3000rpm 60s (t=300nm according to the manufacturer)
	Bake on hotplate 80°C 60s
	UV exposure 5min - N_2 ambient
Preparation	Bake the sample on hotplate 150°C 20 to 30min
TI-Prime	Coating at 3000rpm 20s (P1)
	Bake on hotplate 150°C 40s
PAK-01*	ramp speed 350 (500)rpm→1000rpm→3000rpm (t=370nm; Fig. 5.10)
	Bake on hotplate 80°C 60s
	UV exposure 5min - N_2 ambient

* undiluted or diluted polymer

B.4.2 PAK-01 polymer

B.4.2.1 The exponential model regarding the curve of the PAK-01 polymer thicknesses

In the following, the data of the exponential model regarding the PAK-01 (undiluted and diluted 4:1) polymer thickness are given in the tabular form (Fig. 5.10 page54).

Table B.7: Tabular form of the exponential model regarding the PAK-01 polymer thickness curve

Equation	y=A1*exp(-x/t1)+y0
Reduced Chi-Sqr	0,04157
Adj.R-Sqr	0,99711
Value y0	2,01845
Standard error y0	0,23143
Value A1	22,70302
Standard error A1	1,43781
Value t1	1149,89671
Standard error t1	93,72865

Table B.8: Tabular form of the exponential model regarding the PAK-01 (diluted 4:1) polymer thickness curve

Equation	y=A1*exp(-x/t1)+y0
Reduced Chi-Sqr	94,87812
Adj.R-Sqr	0,97597
Value y0	269,21342
Standard error y0	34,67443
Value A1	450,46319
Standard error A1	62,74889
Value t1	1935,31777
Standard error t1	642,90591

B.4.2.2 Diluter for the PAK-01 polymer

The following table (Table $B.9$) gives the information regarding the diluter for PAK-01 polymer, ethylen-glycol-monomethylether ($C_3H_8O_2$).

B.5 Etch conditions for lateral structuring of the DBRs

Dry etching in the CCP and ICP for structuring of the DBRs used the conditions as summarized in the following.
Structuring of the Si_3N_4/SiO_2 DBRs

(a) CCP-RIE (Castor) for Si_3N_4/SiO_2 DBRs:
Ar/SF_6/CHF_3= 5.1/2/3 sccm, 50 W, 12.5°C, 18.75mTorr (0.025mBar)
Etch rate ca.30 nm/min
Selectivity to photoresist AZ1518 mask S≅1.5 to 3

Table B.9: Product information of the PAK-01 diluter (ethylen-glycol-monomethylether)

Synonym	2-methoxyethanol, methylglycol
Molecular formula	$C_3H_8O_2$
Chemical formula	$CH_3OCH_2CH_2OH$
Ignition temperature	325°C
Melting point	-85°C
Boiling point	125°C
Flash point	43°C
Density	0.964 g/cm^3 (20°C)
Molar mass	76.09 g/mol
Solubility in water	20°C soluble
pH	(H_2O,20°C) neutral

(b) ICP for Si_3N_4/SiO_2 DBRs (with photoresist mask): $CHF_3/Ar/SF_6$=10/40/5 sccm, 100 W ICP/175 W RF power, 20°C, at 10 mTorr
Etch rate ca. 54 nm/min
Selectivity to photoresist AZ1518 etch mask S≅1
Removing of the photoresist mask:10 sccm of O_2, 2000 W ICP/200 W RF power, 20°C, at 6 mTorr

(c) ICP (*RIE mode*) for Si_3N_4/SiO_2 DBRs:
$Ar/SF_6/CHF_3$= 5.1/2/3 sccm, 250 W, 20°C, at 6/10/19mTorr
Etch rate ca.30 up to 80 nm/min
Selectivity to photoresist masks: AZ1505 S≅2 at 19mTorr; AZ1518 S≅3 at 6mTorr; AZnLoF2070 diluted 5:1 S≅3.5 at 6mTorr

Structuring of the TiO_2/SiO_2 DBRs

(a) CCP-RIE (Castor) for TiO_2/SiO_2 DBRs:
Ar/SF_6= 4/7 sccm, 50 W, 12.5°C, 18.75mTorr
Etch rate ca.21 nm/min
Selectivity to photoresist AZ1518 etch mask S≅0.5

(b) ICP for TiO_2/SiO_2 DBRs:
Ar/SF_6= 20/10 sccm, 300 W RF/500 W ICP, 20°C, 6mTorr
Etch rate ca.80 nm/min
Selectivity to ITO etch mask $S>9$

(c) ICP for TiO_2/SiO_2 DBRs:
Ar/SF_6= 10/10 sccm, varied RF/500 W ICP, 20°C, 6mTorr and 10mTorr
Etch rate ca.30 up to 80 nm/min
Selectivity to photoresist masks:AZnLoF2070 5:1 S≅0.35 to 0.55; AZ1518 S≅0.30

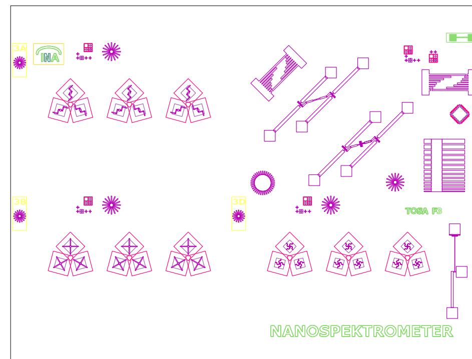

(a) Mesa

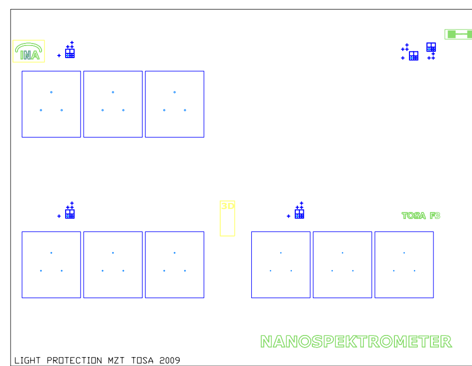

(b) Light protection

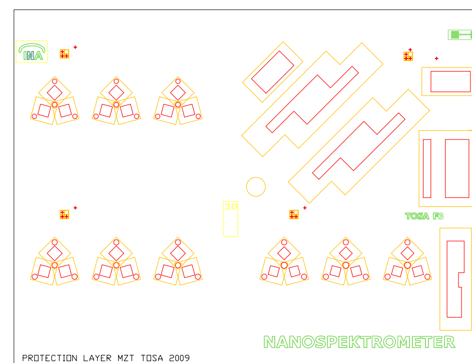

(c) Protection layer

Figure B.1: *Three photomasks MZT TOSA 2009: Mesa MZT TOSA 2009(a), Light protection MZT TOSA 2009 (b) and Protection layer MZT TOSA 2009 (c).*

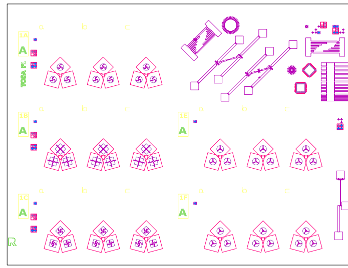

(a) Mesa MAZET Nov2010

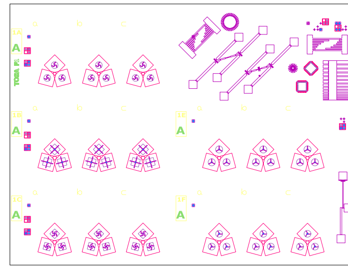

(b) Top electrode MAZET 2010

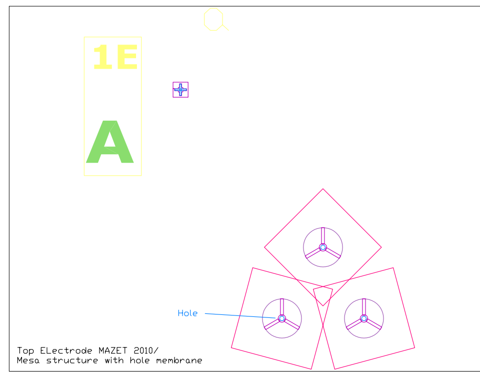

(c) Top electrode zoom-in

Figure B.2: *Two photomasks MAZET 2010: Mesa MAZET mask for patterning the mesa (a), and top electrode mask for patterning the top electrodes (b). Zoom-in image of the filter arrays-a in Block A (field-1F) (c).*

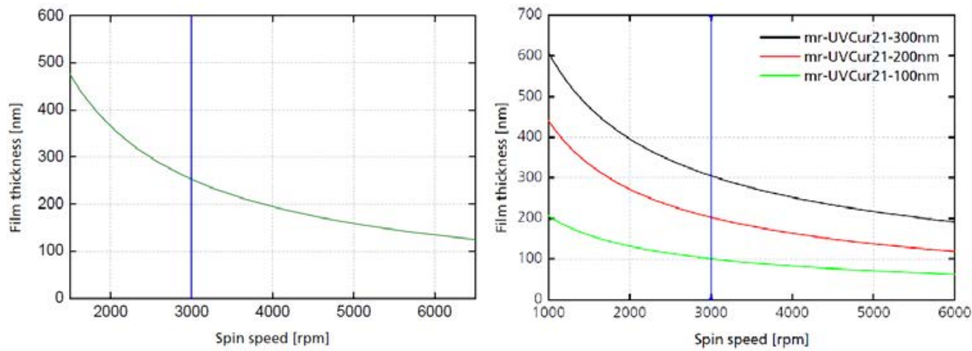

Figure B.3: *Polymer film thickness as a function of spin speed, at 60s spin time, after coating and softbake: mr-UVCur06 (left) and mr-UVCur21 (right); the mr-UVCur21-300nm was used in this work [courtesy of micro-resist-tech. GmbH [111]].*